Aus der Klinik für Psychiatrie und Psychotherapie
der Medizinischen Fakultät Charité – Universitätsmedizin Berlin

DISSERTATION

Funktionelle Echtzeitanalyse der zellulären und molekularen Mechanismen der neuronalen Dysfunktion in chronischer Neuroinflammation

zur Erlangung des akademischen Grades
Doctor medicinae (Dr. med.)

vorgelegt der Medizinischen Fakultät
Charité – Universitätsmedizin Berlin

von

Agata Anna Mossakowski

aus Thorn

Datum der Promotion: 05.06.2016

ZUSAMMENFASSUNG

ZUSAMMENFASSUNG

Für das Verständnis der Pathomechanismen in der Multiplen Sklerose (MS) ist die Darstellung funktioneller Zusammenhänge maßgeblich, mit bisher angewendeten Methoden jedoch nur bedingt möglich. In dieser Arbeit wurde die Zweiphotonenmikroskopie (TPLSM) auch in Kombination mit Fluoreszenzlebensdauermessung (FLIM) sowohl intravital im Tiermodell als auch in vitro an Patientenzellen genutzt, um die Reaktionen des Gewebes auf die Immunzellinvasion zu untersuchen. Hierbei wurde deutlich, dass das Gewebe des zentralen Nervensystems (ZNS) selbst entscheidende Änderungen in Form von Ausbildung eines retikulären Fasernetzwerkes vollzieht, die es erst ermöglichen, dass massenweise periphere Immunzellen einwandern. Die Immunzellen führen direkt und indirekt zur neuronalen Dysfunktion, welche mittels Messung der intrazellulären neuronalen Calciumkonzentration intravital analysiert wurde. Darüber hinaus konnte erstmals gezeigt werden, dass die Aktivität der NADPH-Oxidase (NOX) als Entstehungsort reaktiver Sauerstoffspezies (ROS) in direkter Korrelation mit der neuronalen Dysfunktion steht. Die Zellen, die für die Produktion der ROS im zentralen Nervensystem verantwortlich sind, waren neben peripheren eingewanderten Makrophagen und ortsständigen Mikroglia auch zu einem großen Teil Astrozyten. Die systemische Komponente der MS spiegelte sich in der Überaktivierung der NOX in peripheren $CD11b^+$-Zellen mit signifikanten Unterschieden zwischen den Erkrankungsstadien bei MS-Patienten im Vergleich zu gesunden Probanden und Patienten wider. Eine Behandlung mit dem Antioxidans Epigallokatechingallat, einem Extrakt aus grünem Tee, senkte die NOX-Aktivierung auf gesunde Werte. Insgesamt zeigt diese Arbeit neue Zugänge auf, funktionelle Zusammenhänge neuroimmunologischer Erkrankungen im lebendigen Gewebe in Echtzeit zu erforschen.

ABSTRACT

To fully understand the underlying pathological mechanisms of multiple sclerosis (MS), it is crucial to register and comprehend its functional dynamics. Yet until now, due to the lack of adequate detection methods, many interrelations in cell and metabolism dynamics remain elusive. In this work we introduced two-photon fluorescence microscopy (TPLSM) and its combination with NAD(P)H-fluorescence lifetime imaging (FLIM) both in an animal model for MS as well as human blood cells to investigate tissue and cell response to immune cell invasion. Thereby it became apparent how the central nervous system tissue itself undergoes changes in its extracellular matrix by developing a reticular meshwork that allows peripheral immune cells to infiltrate inflammatory lesions. These immune cells lead to neuronal dysfunction, which was analyzed through measuring intracellular neuronal calcium concentrations in vivo. Furthermore we showed for the first time how the activity of NADPH oxidase (NOX), the main source of reactive oxygen species (ROS), is directly correlated with neuronal dysfunction. The cellular source and the dynamics of ROS production were undetermined up to now, since freely diffusing ROS molecules cannot be localized and their production requires the assembly and not the mere expression of NOX subunits. Using intravital TPLSM and NAD(P)H-FLIM we identified infiltrating peripheral monocytes, activated resident microglia and astrocytes as the main cellular sources of ROS in EAE brainstem lesions. The systemic dimension of MS was mirrored in the over-activation of NOX enzymes in peripheral $CD11b^+$ cells with significant differences between MS patients compared to healthy subjects. Administration of the anti-oxidant epigallocatechin-3-gallate, a green tea extract, counteracted this effect. Overall, this work establishes new intravital approaches to explore functional contexts in neuroinflammation and neurodegeneration in real time.

EINLEITUNG

MULTIPLE SKLEROSE, CIS UND EAE

Multiple Sklerose (MS) ist eine chronisch-entzündliche neurodegenerative Erkrankung des zentralen Nervensystems (ZNS). Sie ist gekennzeichnet durch Immunzellinfiltrate vornehmlich in der weißen Substanz, so genannte Entzündungsherde, die klinisch mit funktionell-anatomisch korrespondierenden Symptomen einhergehen (*1*). Bei etwa 85 % aller Patienten nimmt die Erkrankung zunächst einen schubweisen Verlauf (relapsing-remitting multiple sclerosis, RRMS), bei dem in unregelmäßigen Abständen Symptome einsetzen, die sich in der Regel nach wenigen Wochen vollständig oder teilweise zurückbilden. Bei einem Teil der RRMS-Patienten kann der Verlauf in eine sekundär progrediente MS übergehen (secondary progressive multiple sclerosis, SPMS). Bei den übrigen Patienten setzt bereits primär ein chronisch progredienter Verlauf ein (primary progressive multiple sclerosis, PPMS). Bei 30 – 70 % der Patienten treten vor Erfüllen der Diagnosekriterien der MS neuroinflammatorische Symptome auf. Diese werden als klinisch isoliertes Syndrom bezeichnet (clinically isolated syndrome, CIS) (*2*). Die Multiple Sklerose ist mit einem Erkrankungsgipfel um das dreißigste Lebensjahr die häufigste nicht-traumatische Ursache körperlicher Behinderung im jungen Erwachsenenalter. Die Prävalenz beträgt in Europa je nach Region zwischen 20 und 190 Erkrankte pro 100.000 Einwohner (*3, 4*). Die Ätiologie und die entscheidenden Mechanismen der Pathogenese sind trotz umfangreicher Forschung weiterhin ungeklärt. Es wird angenommen, dass Erkrankungsschübe vornehmlich durch Neuroinflammation gekennzeichnet werden, während progrediente Verläufe und bleibende Schäden in erster Linie Ausdruck eines neurodegenerativen Geschehens sind. Obwohl regelmäßig neue Therapien entwickelt werden, sind weiterhin insbesondere progrediente MS-Verläufe mit konsekutiver körperlicher Behinderung für die Patienten maßgeblich beeinträchtigend in der Lebensqualität (*5*).

NEUROINFLAMMATION UND EXTRAZELLULÄRE MATRIX

Während ursprünglich angenommen wurde, dass extrazelluläre Matrix (ECM) im zentralen Nervensystem lediglich als Gerüst dient, weiß man mittlerweile, dass sie an zahlreichen Prozessen in der Zellinteraktion, -migration und –differenzierung beteiligt ist. Demnach ist es nicht verwunderlich, dass die ECM in neuroinflammatorischen Prozessen nicht nur die Kulisse darstellt, sondern auf vielfältige Arten das

Krankheitsgeschehen mitbestimmt. In der MS wurden multiple Veränderungen in der Zusammensetzung der ECM nachgewiesen, die vor allem die Immunzellmigration zu beeinflussen und Neuroregeneration hemmen (*6-8*).

Oxidativer Stress führt zu Neurodegeneration

Als ein grundsätzlicher Pathomechanismus, der zu Neurodegeneration im Sinne von neuroaxonalen Schäden bei der Multiplen Sklerose führt, wurden unlängst reaktive Sauerstoffspezies (reactive oxygen species, ROS) identifiziert (*9-11*). Unter diesem Begriff werden Moleküle zusammengefasst, die aufgrund ihrer chemischen Eigenschaften in der Lage sind, oxidative Veränderungen in Zellen auszulösen. Unter physiologischen Bedingungen sind Zellen in der Lage, sich gegen diese oxidativen Einflüsse zu schützen. Liegt jedoch ein Ungleichgewicht zwischen der ROS-Produktion und den Eliminationsmechanismen der Zelle vor, entsteht oxidativer Stress. Auch in der Pathogenese der MS scheint oxidativer Stress eine entscheidende Rolle zu spielen. So finden sich beispielsweise in Entzündungsherden, im Liquor sowie im Plasma von MS-Patienten oxidierte DNA, Lipide und Proteine (*12, 13*). Insbesondere Demyelinisierung und Axonschäden werden nach dem bisherigen Kenntnisstand maßgeblich von ROS hervorgerufen (*14*). Die wichtigste Quelle von ROS im Entzündungskontext ist das membranständige Enzym Nicotinamidadenindinukleotidphosphat (NADPH)-Oxidase (NOX) (*15*). In MS-Entzündungsherden konnte eine signifikante Hochregulation von NOX-Untereinheiten nachgewiesen werden (*9*). Der Annahme folgend, dass oxidativer Stress an der Pathogenese der MS beteiligt ist, befinden sich aktuell Antioxidantien in der therapeutischen Erprobung. Zum Beispiel konnte Epigallocatechingallat (EGCG), ein polyphenolisches Metabolit des Grüntees, bereits im Tiermodell der MS, der experimentellen autoimmunen Enzephalomyelitis (EAE), den Krankheitsverlauf positiv beeinflussen (*16, 17*). Der klinische Nutzen von EGCG wird in randomisierten Doppelblindstudien zurzeit erprobt.

Zweiphotonenmikroskopie

Zweiphotonenmikroskopie ist aktuell das geeignetste Instrument, um intravital hochaufgelöst zu mikroskopieren (*18*). Im Gegensatz zur herkömmlichen Fluoreszenzmikroskopie wird jeweils ein Molekül eines Fluorophors von zwei gleichzeitig auftreffenden Photonen angeregt. Diese haben im Vergleich zur herkömmlichen Fluoreszenzmikroskopie die doppelte Wellenlänge und somit die halbe

Frequenz und die halbe Energie. Für die Intravitalmikroskopie hat dieses Phänomen zwei entscheidende Vorteile: Zum einen herrscht nur im Fokuspunkt des Mikroskops eine ausreichende Photonendichte, um das Zusammentreffen zweier Photonen zu ermöglichen. Aus diesem Grund entsteht bei der Zweiphotonenmikroskopie nur in einem kleinen Areal Phototoxizität, sodass Zell- und Gewebeschäden vermieden werden können. Da außerdem Moleküle nur in einem begrenzten Volumen angeregt werden können, ist die räumliche Auflösung somit wesentlich erhöht im Vergleich zu Ein-Photonen-Anregung. Zum anderen ist durch die Verwendung von länger-welligem Licht die Streuung reduziert, was sich in höheren Eindringtiefen äußert. Auf diese Weise können Organe intravital über längere Zeit mit einer Eindringtiefe von bis zu 500 µm mikroskopiert werden.

Fluoreszenzlebensdauer-Mikroskopie

Fluoreszenzlebensdauer-Mikroskopie (fluorescence lifetime imaging, FLIM) ist eine Kombination aus Fluoreszenzmikroskopie und zeitaufgelöster Fluoreszenzmessung. Während Fluoreszenzmikroskopie über die Lokalisation von Zellbestandteilen Aufschluss gibt und auf diese Weise über Markerproteine Zelltypen im Gewebe aufschlüsseln lässt, können anhand der zeitaufgelösten Fluoreszenzmessung die Dynamik und Struktur von Makromolekülen bestimmt werden (*19*).

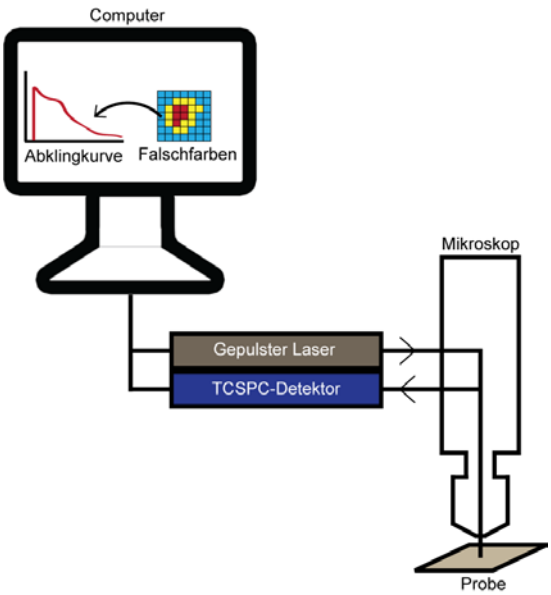

Abbildung 1. Schematischer Aufbau FLIM.

Prinzipiell besteht die Datenerhebung aus drei Bestandteilen: Zunächst wird mit einem gepulsten Laser ein Fluorophor über wenige Femtosekunden angeregt. Die daraufhin folgende Fluoreszenz wird Photon für Photon mithilfe eines Detektors aufgezeichnet (time-correlated single photon counting, TCSPC). Im Computer wird aus dieser Aufzeichnung eine Fluoreszenz-Abklingkurve für jeden Pixel des mikroskopierten Gebiets abgespeichert. Die Parameter der exponentiellen Approximation dieser Kurven können dann wiederum in Falschfarben kodiert als zweidimensionales Bild dargestellt werden (Abbildung 1).

Die Fluoreszenzlebensdauer (τ) eines Makromoleküls, also die Zeit, in der das Molekül Photonen emittiert, ist abhängig von seinem direkten Milieu (*19*) oder ist beeinflusst durch Mechanismen intra- und intermolekularen Energietransfers, wie z.B. des Förster-Resonanzenergietransfers (FRET). Die Fluoreszenzlebensdauer von Nicotinamidadenindinukleotid (NADH) und Nicotinamidadenindinukleotidphosphat (NADPH, im Folgenden zusammenfassend NAD(P)H), beides ubiquitäre Koenzyme, ist abhängig von dem jeweiligen Enzym, an das sie gebunden sind. Auf diese Weise kann spezifisch durch die Bindung von NAD(P)H identifiziert werden, wann die NADPH-Oxidase aktiviert ist (*20*). Während freies NAD(P)H eine Fluoreszenzlebensdauer von ca. 400 ps aufweist, verlängert sich diese durch die Bindung an Enzyme des physiologischen Zellstoffwechsels auf etwa 1100 bis 2700 ps (*19, 21-24*). Bindet NADPH jedoch an NOX, hat es eine Fluoreszenzlebensdauer von 3670 ± 140 ps (*20*).

Förster-Resonanzenergietransfer

Theodor Förster beschrieb 1946 erstmals den Energietransfer zwischen zwei Fluorophoren, einem „Donor“ und einem „Akzeptor“ (*25*). Durch diesen Förster-Resonanzenergietransfer kann einerseits die Fluoreszenz, andererseits aber auch die Fluoreszenzlebensdauer des „Akzeptors“ verändert werden. Seit der Entwicklung zahlreicher Biosensoren in Tieren (*26*) können so mithilfe von FRET und FRET-FLIM unterschiedliche Aspekte zellulärer Funktionen in vitro und in vivo untersucht werden (*27*).

Second harmonic generation

Für die Mikroskopie der extrazellulären Matrix kann das physikalische Phänomen Second harmonic generation (SHG) verwendet werden. Hierbei entsteht durch die besondere Zusammensetzung einer mikroskopierten Struktur Strahlung in der doppelten Frequenz und der halben Wellenlänge des anregenden Lichts. Die Voraussetzungen hierfür erfüllt beispielsweise Kollagen durch seinen nicht-zentrosymmetrischen Aufbau (*28*).

Zielsetzung

In dieser Arbeit sollten die zellulären und molekularen Mechanismen ermittelt werden, die bei der Interaktion von Immunzellen und dem zentralem Nervensystem während der Multiplen Sklerose eine Rolle spielen. Hierfür wurden verschiedene Techniken der funktionellen Mikroskopie etabliert und im Mausmodell angewendet. Zunächst sollte die

Umformung der extrazellulären Matrix und ihr Einfluss auf die Invasion der Immunzellen untersucht werden. Anschließend sollten die direkten und indirekten zellulären Einflüsse auf die Dynamik neuronalen Schadens eruiert und beeinflusst werden. Schließlich sollte aufgezeigt werden, inwieweit eine Translation der entwickelten Methoden zur Untersuchung von molekularen Mechanismen bei Multipler Sklerose realisierbar ist, um mögliche Biomarker zu prüfen und neue Therapieansätze zu entwickeln.

METHODIK

ZWEIPHOTONENMIKROSKOPIE UND FLIM

Alle Experimente wurden mit einem speziell angefertigten Multiphotonenmikroskop für Fluoreszenzlebensdauermessung (FLIM) durchgeführt. Der Ti:Sa Laserstrahl (Wellenlängen 700 – 1080 nm, 140 fs, 80 MHz, Cameleon Ultra II, Coherent, Dieburg, Deutschland) wird von zwei Galvanometerspiegel gescannt und durch ein Wasser-Immersionsobjektiv für tiefe Gewebeschichten (Olympus, Hamburg, Deutschland) fokussiert. Die entstehende Fluoreszenz wird entweder von einem TCSPC-Detektor (p-TCSPC FLIM-X16, LaVision Biotec GmbH, Bielefeld, Deutschland) durch einen Interferenzfilter bei 460 ± 30 nm oder einem Photomultiplier (Hamamatsu, Japan) bei 460 ± 30 nm, 525 ± 25 nm und 593 ± 20 nm detektiert und analysiert. NAD(P)H wurde mit 760 nm angeregt. Es wurde eine durchschnittliche Laserleistung von maximal 8 mW genutzt.

MÄUSE

Die Versuchstierhaltung und -behandlung entsprach dem deutschen Tierschutzgesetz. Alle Tierversuche wurden vom Landesamt für Gesundheit und Soziales bewilligt (G0198/11 und G0081/10) und wurden entsprechend aktueller Leitlinien und Bestimmungen durchgeführt.

A. STÄMME

Alle Experimente wurden an Mäusen auf einem C57BL/6 Hintergrund durchgeführt. Für die Intravitalmikroskopie wurden Wildtyp-C57BL/6- oder verschiedene fluoreszierende Stämme verwendet wie CX3CR1+/- EGFP, CerTN L15 oder CerTN L15 x LysM tdRFP. Der CerTN L15-Stamm exprimiert einen Troponin-C-basierten Calcium-Biosensor über Thy 1 (im ZNS vornehmlich in Neuronen exprimiert). Troponin-C ist an Cerulean und Citrulin gebunden, die ein FRET-Paar bilden. Auf diese Weise können intrazelluläre

Calciumkonzentrationen zwischen 100 nM bis 10 µM gemessen werden (*29*). In diesen Mäusen sind neuronale Calciumkonzentrationen von über 1 µM über den Zeitraum einer Stunde ein verlässlicher Indikator früher neuronaler Dysfunktion (*30*). CerTN L15-Mäuse wurden auch mit LysM tdRFP- Mäusen gekreuzt, sodass zusätzlich tdRFP (tandem dimer red fluorescent protein) (*31*) in LysM+ Zellen exprimiert wurde (*32*). Der CX3CR1+/- EGFP-Stamm exprimiert EGFP (enhanced green fluorescent protein) in vornehmlich in Monozyten und Mikroglia. C57BL/6-Mäusen wurde Sulforhodamin 101 injiziert, um Astrozyten spezifisch zu markieren (*33, 34*).

B. Intravitalmikroskopie

Der Hirnstamm der Mäuse wurde zu zwei Zeitpunkten in 1,5% Isofluran-Narkose intravital mikroskopiert: zum Erkrankungsbeginn (onset, ein bis zwei Tage nach Einsetzen der ersten klinischen Symptome) und im Erkrankungsgipfel (peak, drei bis sieben Tage nach Einsetzen der ersten klinischen Symptome). Die Bildaufnahme erfolgte Atemzug-getriggert, um Atmungsartefakte zu vermeiden. So konnten Fluoreszenzaufnahmen mit unterschiedlichen Wellenlängen am identischen Areal erfasst werden (*35*).

Isolation der peripheren Monozyten

Gesunde Probanden, unbehandelte CIS-Patienten sowie mit Glatirameracetat behandelte RRMS-Patienten, die in einer randomisierten Doppelblindstudie entweder 600 mg EGCG oder ein Placebo als tägliches Nahrungsergänzungsmittel erhielten, wurden nach ausführlicher Aufklärung und Einverständniserklärung der Probanden eingeschlossen. Venöses Blut wurde in CPT-Vacutainern (BD Biosciences, Heidelberg, Deutschland) entnommen. Periphere Monozyten wurden aus dem venösen Blut der Patienten sowie aus den Milzen von EAE-Mäusen isoliert. Über Magnetic Cell Separation (MACS, Miltenyi Biotec, Bergisch Gladbach, Deutschland) wurde gemäß Herstellerprotokoll eine $CD11b^+$-Anreicherung durchgeführt. Die entsprechenden $CD11b^+$-Monozyten wurden in Medium suspendiert und in eigens angefertigte Mikroskopierkammern injiziert. Die Qualität der MACS-Anreicherung wurde mittels Durchflusszytometrie überprüft. Die Messungen wurden unter standardisierten Bedingungen durchgeführt.

Datenanalyse

Die Datenanalyse erfolgte mit Hilfe von GraphPad Prism 4 (Graphpad Software, USA) und Origin Pro (Origin Lab, USA). FLIM-Daten wurden mittels einer laboreigenen Software ausgewertet.

Ergebnisse

In Entzündungsherden lässt sich SHG detektieren

Mittels intravitaler Zweiphotonenmikroskopie in einer Wellenlänge zwischen 1050 nm und 1110 nm konnten wir im Hirnstamm von Mäusen mit EAE in bis zu 100 µm Tiefe netzförmig strukturiertes SHG-Signal aufzeichnen. Diese Struktur war deutlich abzugrenzen sowohl von den umliegenden Zellen und Gefäßen als auch vom SHG der Meningen, welches eine andere Anordnung und Form aufwies (Abbildung 2). Ein vergleichbares Netzwerk konnte weder in gesunden Tieren noch in umfangreichen Zellkulturexperimenten mit verschiedenen Zellzusammensetzungen und Stimulanzien nachgewiesen werden.

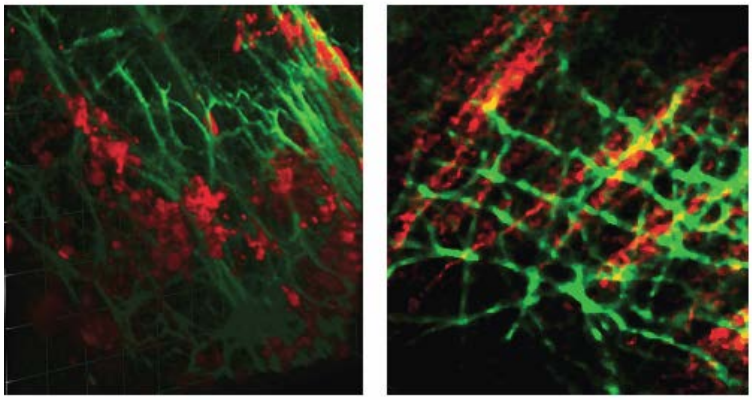

Abbildung 2. Hirnstamm einer Maus mit EAE im Erkrankungsgipfel. (A) C57BL/6 nach Injektion von Suforhodamin, welches Astrozyten anfärbt. Zusammengefügtes Bild, Fluoreszenz angeregt bei 850 nm (Sulforhodamin = rot) und 1110 nm (SHG = grün). (B) CerTN L15. Zusammengefügtes Bild, Fluoreszenz angeregt bei 850 nm (YFP in Axonen = rot) und 1110 nm (SHG = grün).

Neuronale Dysfunktion kann mit FRET-FLIM quantifiziert werden

Zunächst wurde der direkte Effekt von Immunzellkontakten auf die neuronale Funktion untersucht. Der neuronale FRET-Calcium Sensor der CerTN L15 Mäuse ermöglicht eine intravitale FRET-FLIM Analyse, so dass während der neuroinflammatorischen Prozesse kalibrationsfrei neuronale Dysfunktion quantifiziert werden kann. Der Calciumspiegel in den Somata und Nervenfortsätzen mit Immunzellkontakt war direkt an den Kontaktstellen signifikant höher (FRET-Signal bis zu 58%, 1.66 µM Calcium) als in Somata und Fortsätzen, die nicht in unmittelbarer Nähe zu Immunzellen lagen (FRET-Signal ca. 8%, 110 nM Calcium).

EINE ÜBERAKTIVIERUNG VON NOX IN EAE KORRELIERT MIT DEM KRANKHEITSVERLAUF UND MIT NEURONALEN SCHÄDEN IM CNS

Neuronale Schäden entstehen jedoch in der MS auch ohne direkten Zellkontakt durch frei diffundierende Stoffe wie ROS. Im Hirnstamm von Mäusen mit EAE im Erkrankungsgipfel (peak) konnten wir intravital durch Anfärbung von ROS mit Amplex Red® extrazelluläre ROS-Konzentrationen von etwa 200 µM nachweisen (Abbildung 3). Bei gesunden Kontrollen lagen ROS unter der Nachweisgrenze.

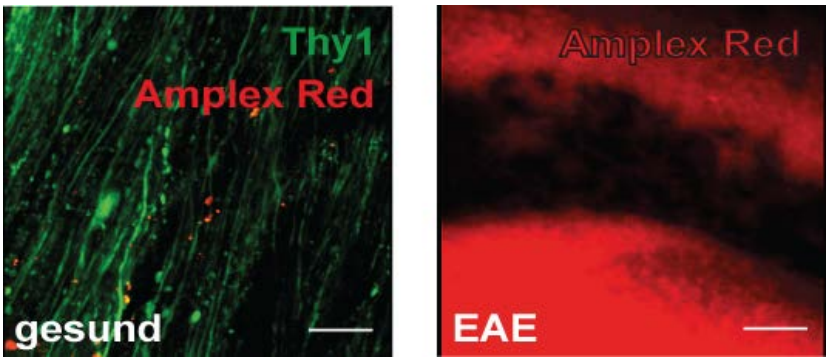

Abbildung 3. ROS-Konzentration im Hirnstamm einer gesunden Maus im Vergleich zu einer Maus mit EAE im Erkrankungsgipfel. Amplex Red® wurde als ROS Indikator genutzt. λexc = 910 nm, λem = 525 ± 25 nm (Citrin in Neuronen/Thy1, grün), λem = 593 ± 20 nm (Amplex Red®, rot), Maßstabsleiste = 50 µm.

Anschließend untersuchten wir, wo und zu welchem Zeitpunkt NOX als Hauptquelle von ROS aktiviert ist. Die NOX-Aktivierung wurde mithilfe von intravitaler NAD(P)H-FLIM im Hirnstamm von Mäusen mit EAE (n = 4 bei EAE-onset und n = 7 im EAE peak) sowie gesunder Kontrollen (n = 3) gemessen. Die Fluoreszenzlebensdauer von enzym-gebundenem NAD(P)H wurde für jeden Pixel des mikroskopierten Gebiets (300x300 µm, 517x517 Pixel, Tiefe zwischen 30 und 150 µm bei z-step von 2 µm) ermittelt. Die spezifische NAD(P)H-Fluoreszenzlebensdauer, die eine NOX-Aktivierung indiziert („NOX only“ zwischen 3.3 – 3.9 ns), wurde lediglich in Entzündungsherden (mikroskopisch ermittelt über die massive Infiltration von $LysM^{+}$ tdRFP-Zellen) gesehen, jedoch nicht in Gebieten ohne Zellinfiltration desselben Hirnstammes (Abbildung 4 A und B). Die Fläche der NOX-spezifischen Fluoreszenzlebensdauer in EAE-Entzündungsherden wurde quantifiziert, um eventuelle Veränderungen der NOX-Aktivierung im Krankheitsverlauf zu ermitteln. Gesunde Kontrollen wiesen eine NOX-Aktivierung in 2.19 ± 0.94 % (n = 3) des NAD(P)H-abhängigen Gewebes (definiert als die Fläche aller Zellen mit NAD(P)H-abhängigen Stoffwechsel im Sichtfeld) auf. Zu Beginn der klinischen Symptomatik lag die NOX-Aktivierung bereits bei 4.98 ± 1.53 % des NAD(P)H-abhängigen Gewebes und stieg signifikant auf 14.88 ± 5.81 % des NAD(P)H-abhängigen Gewebes im Erkrankungsgipfel. Zusätzlich korrelierten wir diese Messungen mit der simultanen Quantifizierung von neuronaler Dysfunktion in CerTN

L15 x LysM tdRFP-Mäusen durch FRET-FLIM. Eine erhöhte NOX-Aktivierung war mit einer kritischen Erhöhung des intrazellulären Calciumspiegels über 1 µM („Ca^{2+} > 1 µM“) in Neuronen räumlich korreliert (Abbildung 4 C). Bei EAE-onset war der Calciumspiegel in 1.32 ± 0.78 % der neuronalen Gewebefläche auf über 1 µM erhöht (n = 3), im peak betrug dieser Anteil 12.80 ± 2.41 % der neuronalen Gewebefläche (n = 4), während der Calciumspiegel in den gesunden Kontrollen in keiner Messung kritische Werte erreichte.

Der zelluläre Ursprung von oxidativem Stress in EAE

Diese Ergebnisse warfen die Frage auf, welche Zellen in der erhöhten NOX-Aktivierung im Hirnstamm bei EAE-Mäusen eine Rolle spielen. Wir betrachteten daher die Kolokalisierung der aktivierten NOX mit spezifischen Zellmarkern, indem wir Masken für Neurone (Thy1 in der CerTN L15-Maus), Makrophagen und Mikroglia ($LysM^+$ tdRFP und $CX_3CR_1^+$) und Astrozyten (Sulforhodamin) aus Fluoreszenzintensitätsbildern anfertigten und diese über die entsprechenden Fluoreszenzlebenszeitbilder derselben Aufnahme legten. Während Neurone zu Krankheitsbeginn und -gipfel sowohl selbst eine geringe Fläche mit NOX-Aktivierung aufweisen (jeweils 0.8 ± 0.5 % und 1.8 ± 0.4 % der NAD(P)H-abhängigen Enzyme in den Neuronen) als auch einen geringen Beitrag zur gesamten Fläche mit NOX-Aktivierung leisten (jeweils 2.3 % und 3.8 % des NAD(P)H-abhängigen Gewebes), war die Fläche mit NOX-Aktivierung in Makrophagen im Krankheitsgipfel gegenüber der Aktivierung zu Krankheitsbeginn signifikant erhöht (26.4 ± 6.6 % gegenüber 7.9 ± 2.3 %). Die NOX-Aktivierung innerhalb der $LysM^+$-Zellen machte einen Anteil von 22.7 ± 6.4 % zu Krankheitsbeginn und 28.2 ± 4.7 % im Krankheitsgipfel der gesamten NOX-Aktivierung aus. Zusätzlich konnte NOX-Aktivierung in $CX3CR1^+$-Zellen nachgewiesen werden, diese war an der Gesamtfläche mit 13.1 ± 2.3 % zu Krankheitsbeginn und 17.4 ± 2.4 % im Krankheitsgipfel beteiligt. Ein maßgeblicher Anteil der gesamten NOX-Aktivierung sowohl zu Krankheitsbeginn als auch im Krankheitsgipfel entstammte Sulforhodamin-markierten Astrozyten (jeweils 26.4 ± 4.4 % und 34.2 ± 5.6 %).

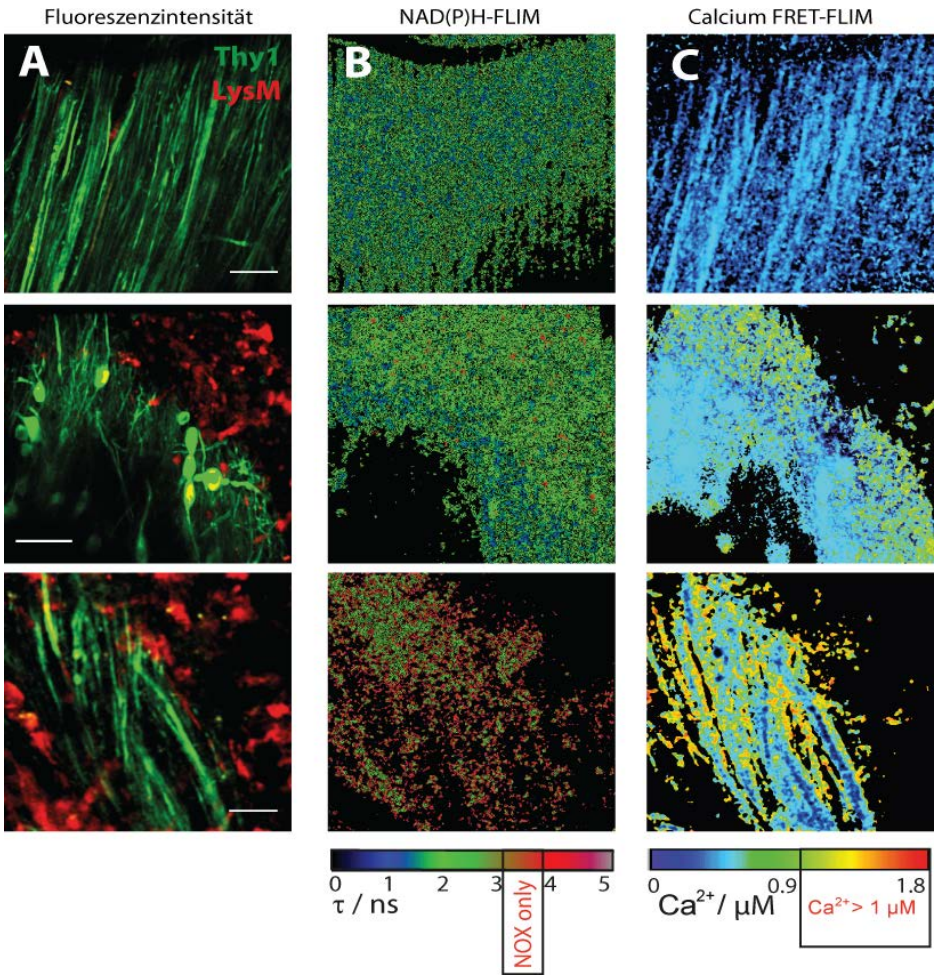

Abbildung 4. NOX-Aktivierung ist abhängig vom Krankheitsstadium und korreliert mit neuronaler Dysfunktion. (A) LysM+ tdRFP Zellen (rot) infiltrieren das ZNS (Neurone in grün). Maßstabsleiste = 30 µm. (B) Fluoreszenzlebensdauer des in A dargestellten Areals. Enzymgebundenes NAD(P)H mit Fluoreszenzlebensdauern zwischen 1 und 3 ns ist in grün und blau dargestellt, an NOX gebundenes NAD(P)H ("NOX only" gate) erscheint rot. (C) Neuronale Calciumspiegel des in A dargestellten Areals. Kritische Erhöhung des intrazellulären Calciumspiegels („Ca^{2+} > 1 µM" gate) dargestellt in gelb.

NOX IST IN PERIPHEREN MONOZYTEN IN MS ÜBERAKTIVIERT, KANN JEDOCH DURCH EGCG GEHEMMT WERDEN

Um zu ermitteln, ob der in Makrophagen beobachtete Anstieg der NOX-Aktivierung nach der Infiltration des ZNS stattfindet oder bereits in peripheren Zellen vorhanden ist, wurden $CD11b^+$-Monozyten aus peripherem Blut von MS-Patienten, CIS-Patienten und gesunden Probanden isoliert. Bei gesunden Menschen war NOX in $CD11b^+$-Monozyten nur geringfügig aktiviert (8.68 %, n = 6). Es gab darin keinen signifikanten Unterschied zu CIS-Patienten (NOX-Aktivierung von 7.70 %, n = 5). Bei den untersuchten MS-Patienten war die NOX-Aktivierung höher: In einem Einzelfall einer MS mit Kontraindikationen gegen Schubtherapie konnten wir Blut einer unbehandelten

Patientin im MS-Schub akquirieren. Die NOX-Aktivierung lag bei 36.75 %. MS-Patienten, die mit dem Standardmedikament Glatirameracetat und einem Placebo behandelt wurden, zeigten eine NOX-Aktivierung von 16.20 % (n = 6). Nahmen die mit Glatirameracetat behandelten MS-Patienten statt Placebo über drei Monate hochkonzentrierte EGCG-Kapseln ein, reduzierte sich die NOX-Aktivierung auf 6.46 % (n = 6; Abbildung 5).

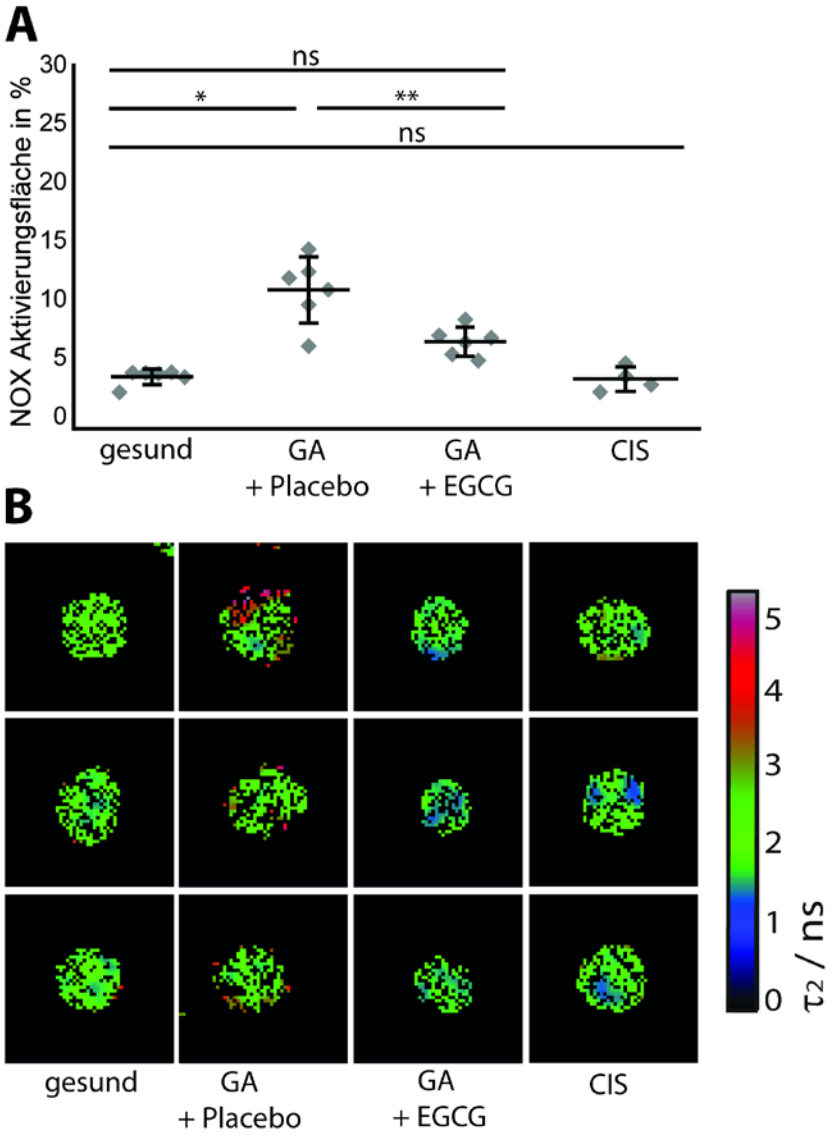

Abbildung 5. NOX-Aktivierung in humanen peripheren CD11b$^+$-Zellen. (A) Quantifizierung der NOX-Aktivierungsfläche in humanen CD11b$^+$-angereicherten Monozyten in gesunden Kontrollen (*n* = 6), RRMS-Patienten, die entweder mit Glatirameracetat (GA) und Placebo (*n* = 6) oder mit Glatirameracetat (GA) und EGCG (*n* = 6) behandelt wurden, sowie CIS-Patienten (n = 6). (B) Repräsentative Fluoreszenzlebensdauerbilder humaner CD11b$^+$-Monozyten. Maßstabsleiste = 50 µm. Statistische Auswertung mit ANOVA-Test (* - $p < 0.05$, ** - $p < 0.01$, *** - $p < 0.001$).

DISKUSSION

Während die neuroinflammatorischen Aspekte der MS seit Jahrzehnten umfänglich erforscht werden und die existierenden Therapien vor allem auf Antiinflammation und Immunmodulation zielen, rückt die schon zu Beginn der Erkrankung auftretende Neurodegeneration erst in den letzten Jahren in den Fokus wissenschaftlicher Bemühungen (*36*). Viele der neueren Therapien sind darauf ausgelegt, Immunzellen an der Einwanderung in das Gehirn zu hindern - mit teilweise fatalen Nebenwirkungen wie der Progressiven Multifokalen Leukenzephalopathie (*37*). Überdies ist die neuroprotektive Wirkung der aktuell verwendeten Therapeutika umstritten und nur schwer zu quantifizieren.

Um gezielt neue Therapien zu entwickeln ist es daher unumgänglich, die genauen Mechanismen zu verstehen, wie sich Immunzellen im zentralen Nervensystem verhalten und wie sich das Gewebe im Rahmen der Entzündungsreaktion verändert. Wir detektierten in den Entzündungsherden netzartig strukturiertes SHG-Signal, welches im biologischen Kontext vor allem nicht-zentrosymmetrische Strukturen wie Kollagen kennzeichnet. Diese Strukturen dienten $CD4^+$-T-Zellen als Migrationswege (*38*). Ein ähnliches SHG-Netzwerk wurde bereits in ZNS-Infektionen mit Toxoplasma gondii dargestellt. In gesundem ZNS Gewebe hingegen kann es nicht nachgewiesen werden. Histologisch konnte an den entsprechenden Stellen jedoch kein erhöhtes Kollagen nachgewiesen werden, sodass der Ursprung des SHG-Signals in Entzündungen weiterhin ungeklärt bleibt (*39*). Eine Modulation dieser Migrationswege könnte ein wirksamer Angriffspunkt für neue Therapien sein.

Des Weiteren kann die direkte Interaktion von Immunzellen mit Nervenzellen zu neuronaler Dysfunktion führen (*30, 40*) und stellt einen unmittelbaren neuen therapeutischen Angriffspunkt dar. Mittels Fluoreszenlebensdauermessungen in FRET-Modellen, so genannter FRET-FLIM, konnten wir neuronale Dysfunktion erstmals dreidimensional intravital über die Zeit quantifizieren. Hierbei ist im Gegensatz zu klassischer ratiometrischer FRET-Auswertung keine Kalibrierung notwendig (*41*). Die ratiometrische Methode ist in intravitalen Experimenten nicht überzeugend anwendbar, da sie direkt die Zellparameter beeinflusst und verfälscht.

In den durchgeführten Untersuchungen zeigte sich, dass zu einem gewissen Anteil der neuronale Schaden nicht durch direkte Zellkontakte vermittelt wird. Die Produktion von

löslichen Faktoren wie reaktive Sauerstoffspezies durch die Immunzellen kann hierbei eine wichtige Rolle spielen. Mit FRET-FLIM konnten wir eine erhöhte NADPH-Oxidase (NOX)-Aktivierung mit neuronaler Dysfunktion korrelieren. Mithilfe der NAD(P)H-Fluoreszenzlebensdauermikroskopie konnte in dieser Arbeit erstmals die NOX als Entstehungsort von freien Radikalen in Echtzeit funktionell beobachtet werden. Weiterhin wird die Methode als Monitor antioxidativer und somit neuroprotektiver Effekte auf molekularer Ebene vorgestellt. Das Grüntee-Phenol EGCG hatte einen starken antioxidativen Effekt auf periphere $CD11b^{+}$-Zellen sowohl bei EAE-Mäusen und MS-Patienten (*42*), aber auch das Standardtherapeutikum Glatirameracetat scheint entsprechend früherer Berichte (*43*) antioxidativ zu wirken. In dieser Studie wurde der direkte molekulare Effekt einer EGCG-Therapie auf die NOX-Aktivierung gemessen. Die klinische Wirkung von oralem EGCG in MS wird aktuell in randomisiert-kontrollierten Doppelblindstudien untersucht (NCT00525668, NCT00799890 und NCT01417312). Da es sich jedoch vermuten lässt, dass es sich hierbei um eine neuroprotektive Therapie handelt, müssten womöglich langfristigere Endpunkte gesetzt werden als bei bisherigen MS-Studien, um Schubresiduen und eine Langzeitbehinderung verlässlich quantifizieren zu können.

Oxidativer Stress scheint bereits in frühen Krankheitsphasen Nervenschäden auszulösen (*10*), und Medikamente, die sich gegen oxidativen Stress richten, haben bereits neuroprotektive Effekte gezeigt (*44, 45*). Durch eine verbesserte neuroprotektive Therapie wird erhofft, die Progression der Erkrankung aufzuhalten und den Grad der Behinderung betroffener Patienten verringern zu können (*46*).

In unseren Untersuchungen sahen wir erstaunliche Parallelen in der NOX-Aktivierung und ihrer therapeutischen Beeinflussbarkeit zwischen humanen und murinen Proben. Die EAE steht oft in der Kritik, nicht ausreichend die Krankheitsmechanismen und -verläufe zu spiegeln, um übertragbar auf den Menschen zu sein (*47*). So muss die von uns gemessene erhöhte NOX-Aktivität im ZNS der EAE-Mäuse nicht zwangsläufig auf die gleiche Weise in der menschlichen MS eine Rolle spielen. Beim Menschen sind sieben NOX-Isotypen bekannt, NOX1 bis 5 und DUOX 1 und 2 (*15*). Bisher wurden verschiedene NOX-Isotypen histologisch in Mikroglia, in Astrozyten und Neuronen nachgewiesen. Es ist bekannt, dass die NOX-Isotypen im ZNS unterschiedliche Aktivitäts- und Aktivierbarkeitsmuster aufweisen (*48*). Während NAD(P)H-FLIM Aussagen über die Aktivität der NOX erlaubt, kann man jedoch nicht zwischen den

verschiedenen NOX-Isotypen unterscheiden. Die genaue Bedeutung der einzelnen NOX-Isotypen in der MS ist weiterhin ungeklärt.

Den NOX-Enzymen ist jedoch gemein, dass sie stets membrangebunden sind. Dieser Fakt vereinfacht die Identifikation ihres zellulären Ursprungs. Wir erwarteten entsprechend dem Bericht von Nikic et al. (*10*), vornehmlich in Makrophagen beziehungsweise aktivierten Mikroglia im ZNS von EAE-Mäusen aktivierte NOX zu finden. Auch ältere Arbeiten zeigten, dass diese Zellen in Kokulturen mit Neuronen ROS sezernierten und so zum Untergang der Nervenzellen führen (*49*). In unserer Arbeit ließ sich jedoch nur knapp über ein Drittel der gesamten NOX-Aktivierung auf Makrophagen und Mikroglia zurückführen. Überraschend war hingegen der hohe Anteil, den die NOX-Aktivierung innerhalb von Astrozyten an der gesamten NOX-Aktivierung ausmachte. Diese Diskrepanz könnte durch die Visualisierung von NOX mithilfe unterschiedlicher Methoden erklärt werden. Während der bisher geführte histologische Nachweis lediglich die Exprimierung von NOX in unterschiedlichen Zelltypen mithilfe von Färbung einzelner Untereinheiten aufzeigt (*50*), wird mit NAD(P)H-FLIM der Moment identifiziert, in dem NADPH an NOX gebunden ist, das Enzym also funktionell aktiv ist und ROS produziert. Daher ist es möglich, dass analog den Vorberichten NOX in Mikroglia und Makrophagen in MS-Entzündungsherden zwar stark exprimiert wird, aber nicht in allen Zellen NOX aktiviert ist, weil die Voraussetzungen für einen metabolischen Shift zugunsten der Produktion von ROS nicht erfüllt werden. Gleichzeitig könnten andere Zellen, etwa Astrozyten, eine geringere Exprimierung, aber eine relativ höhere Aktivierung der NOX aufzeigen (*51*). Einen erwartungsgemäß sehr geringen Anteil an der gesamten NOX-Aktivierung tragen $CD4^{+}$YFP-Zellen mit 3 % während des gesamten Krankheitsverlaufs bei und sind somit wahrscheinlich nicht direkt an der oxidativen Schädigung der Neurone beteiligt.

Die von uns gemessene erhöhte NOX-Aktivierung in peripheren Monozyten unterstützt die Betrachtung der MS als komplexen systemischen Prozess: Es konnten signifikante Unterschiede zwischen den Erkrankungsstadien sowohl in der EAE als auch bei MS-Patienten gefunden werden (*42*). Die Aktivierung der NADPH-Oxidase in peripheren Makrophagen ist jedoch ein vielschichtiger Prozess. Bis zum Beginn des 21. Jahrhunderts ging man davon aus, dass NOX primär der Pathogenabwehr über den oxidativen Burst dient. Mittlerweile werden immer mehr intra- und interzelluläre Signalwege und physiologische Abläufe entdeckt, an denen die NOX über ROS-

Produktion beteiligt ist (*52*). Um die Rolle der NOX-Aktivierung in peripheren Immunzellen weiter herauszuarbeiten, sollen in Zukunft mehr und größere Vergleichsgruppen herangezogen werden: Die schubförmig remittierende MS wird verglichen mit den progressiven Formen SPMS und PPMS, sowie mit der erst kürzlich als Krankheitsentität abgegrenzten Neuromyelitis optica, bei der ebenfalls schubförmig entzündliche Läsionen des ZNS auftreten. Kontrollen einer systemischen Entzündung bieten die rheumatoide Arthritis und Infektionen. Einen Sonderfall stellt die septische Granulomatose dar – diese Erbkrankheit geht mit einem Funktionsverlust der NADPH-Oxidase einher. Bisher wurde kein Fall von MS bei septischer Granulomatose publiziert.

Neben den neuen Einblicken in die molekularen und zellulären Mechanismen bei der EAE und der MS sowohl im ZNS als auch in der Peripherie offenbart diese Arbeit das außerordentliche Potenzial der funktionellen Mikroskopie mit NAD(P)H-FLIM und SHG als intravital einsetzbare, markerfreie Methoden zur Beobachtung von Biomarkern oder zur Kontrolle individuellen Therapieansprechens einer personalisierten Medizin.

LITERATURVERZEICHNIS

1. J. H. Noseworthy, C. Lucchinetti, M. Rodriguez, B. G. Weinshenker, Multiple sclerosis. *N Engl J Med* **343**, 938-952 (2000); published online EpubSep 28 (10.1056/NEJM200009283431307).
2. D. Miller, F. Barkhof, X. Montalban, A. Thompson, M. Filippi, Clinically isolated syndromes suggestive of multiple sclerosis, part I: natural history, pathogenesis, diagnosis, and prognosis. *The Lancet. Neurology* **4**, 281-288 (2005); published online EpubMay (10.1016/S1474-4422(05)70071-5).
3. M. Pugliatti, G. Rosati, H. Carton, T. Riise, J. Drulovic, L. Vecsei, I. Milanov, The epidemiology of multiple sclerosis in Europe. *Eur J Neurol* **13**, 700-722 (2006); published online EpubJul (10.1111/j.1468-1331.2006.01342.x).
4. T. Hein, W. Hopfenmuller, [Projection of the number of multiple sclerosis patients in Germany]. *Nervenarzt* **71**, 288-294 (2000); published online EpubApr (
5. K. Karampampa, A. Gustavsson, C. Miltenburger, B. Eckert, Treatment experience, burden and unmet needs (TRIBUNE) in MS study: results from five European countries. *Multiple sclerosis* **18**, 7-15 (2012); published online EpubJun (10.1177/1352458512441566).
6. J. van Horssen, C. D. Dijkstra, H. E. de Vries, The extracellular matrix in multiple sclerosis pathology. *Journal of neurochemistry* **103**, 1293-1301 (2007); published online EpubNov (10.1111/j.1471-4159.2007.04897.x).
7. J. van Horssen, L. Bo, C. M. Vos, I. Virtanen, H. E. de Vries, Basement membrane proteins in multiple sclerosis-associated inflammatory cuffs: potential role in influx and transport of leukocytes. *Journal of neuropathology and experimental neurology* **64**, 722-729 (2005); published online EpubAug (
8. H. Mohan, M. Krumbholz, R. Sharma, S. Eisele, A. Junker, M. Sixt, J. Newcombe, H. Wekerle, R. Hohlfeld, H. Lassmann, E. Meinl, Extracellular matrix in multiple sclerosis lesions: Fibrillar collagens, biglycan and decorin are upregulated and associated with infiltrating immune cells. *Brain pathology* **20**, 966-975 (2010); published online EpubSep (10.1111/j.1750-3639.2010.00399.x).
9. M. T. Fischer, R. Sharma, J. L. Lim, L. Haider, J. M. Frischer, J. Drexhage, D. Mahad, M. Bradl, J. van Horssen, H. Lassmann, NADPH oxidase expression in active multiple sclerosis lesions in relation to oxidative tissue damage and mitochondrial injury. *Brain* **135**, 886-899 (2012); published online EpubMarch 1, 2012 (10.1093/brain/aws012).
10. I. Nikic, D. Merkler, C. Sorbara, M. Brinkoetter, M. Kreutzfeldt, F. M. Bareyre, W. Bruck, D. Bishop, T. Misgeld, M. Kerschensteiner, A reversible form of axon damage in experimental autoimmune encephalomyelitis and multiple sclerosis. *Nat Med* **17**, 495-499 (2011)http://www.nature.com/nm/journal/v17/n4/abs/nm.2324.html#supplementary-information).
11. J. van Horssen, G. Schreibelt, J. Drexhage, T. Hazes, C. D. Dijkstra, P. van der Valk, H. E. de Vries, Severe oxidative damage in multiple sclerosis lesions coincides with enhanced antioxidant enzyme expression. *Free Radical Biology and Medicine* **45**, 1729-1737 (2008)http://dx.doi.org/10.1016/j.freeradbiomed.2008.09.023).
12. L. Haider, M. T. Fischer, J. M. Frischer, J. Bauer, R. Hoftberger, G. Botond, H. Esterbauer, C. J. Binder, J. L. Witztum, H. Lassmann, Oxidative damage in multiple sclerosis lesions. *Brain* **134**, 1914-1924 (2011); published online EpubJul (10.1093/brain/awr128).
13. M. I. Hunter, B. C. Nlemadim, D. L. Davidson, Lipid peroxidation products and antioxidant proteins in plasma and cerebrospinal fluid from multiple sclerosis patients. *Neurochem Res* **10**, 1645-1652 (1985); published online EpubDec (
14. H. Lassmann, Mechanisms of white matter damage in multiple sclerosis. *Glia*, (2014); published online EpubJan 28 (10.1002/glia.22597).
15. K. Bedard, K.-H. Krause, The NOX Family of ROS-Generating NADPH Oxidases: Physiology and Pathophysiology. *Physiological reviews* **87**, 245-313 (2007); published online EpubJanuary 1, 2007 (10.1152/physrev.00044.2005).
16. O. Aktas, T. Prozorovski, A. Smorodchenko, N. E. Savaskan, R. Lauster, P. M. Kloetzel, C. Infante-Duarte, S. Brocke, F. Zipp, Green tea epigallocatechin-3-gallate mediates T cellular NF-kappa B inhibition and exerts neuroprotection in autoimmune encephalomyelitis. *J Immunol* **173**, 5794-5800 (2004); published online EpubNov 1 (
17. K. Herges, J. M. Millward, N. Hentschel, C. Infante-Duarte, O. Aktas, F. Zipp, Neuroprotective effect of combination therapy of glatiramer acetate and epigallocatechin-3-gallate in neuroinflammation. *PLoS One* **6**, e25456 (2011)10.1371/journal.pone.0025456).

18. R. Weigert, N. Porat-Shliom, P. Amornphimoltham, Imaging cell biology in live animals: ready for prime time. *J Cell Biol* **201**, 969-979 (2013); published online EpubJun 24 (10.1083/jcb.201212130).
19. J. R. Lakowicz, H. Szmacinski, K. Nowaczyk, M. L. Johnson, Fluorescence lifetime imaging of free and protein-bound NADH. *Proc Natl Acad Sci U S A* **89**, 1271-1275 (1992); published online EpubFeb 15 (
20. R. Niesner, P. Narang, H. Spiecker, V. Andresen, K. H. Gericke, M. Gunzer, Selective Detection of NADPH Oxidase in Polymorphonuclear Cells by Means of NAD(P)H-Based Fluorescence Lifetime Imaging. *Journal of Biophysics* **2008**, (2008).
21. K. Konig, M. W. Berns, B. J. Tromberg, Time-resolved and steady-state fluorescence measurements of beta-nicotinamide adenine dinucleotide-alcohol dehydrogenase complex during UVA exposure. *J Photochem Photobiol B* **37**, 91-95 (1997); published online EpubJan (
22. J. C. Brochon, P. Wahl, M. O. Monneuse-Doublet, A. Olomucki, Pulse fluorimetry study of octopine dehydrogenase-reduced nicotinamide adenine dinucleotide complexes. *Biochemistry* **16**, 4594-4599 (1977); published online EpubOct 18 (
23. A. Gafni, L. Brand, Fluorescence decay studies of reduced nicotinamide adenine dinucleotide in solution and bound to liver alcohol dehydrogenase. *Biochemistry* **15**, 3165-3171 (1976); published online EpubJul 27 (
24. D. M. Jameson, V. Thomas, D. M. Zhou, Time-resolved fluorescence studies on NADH bound to mitochondrial malate dehydrogenase. *Biochim Biophys Acta* **994**, 187-190 (1989); published online EpubFeb 2 (
25. T. Förster, Zwischenmolekulare Energiewanderung und Fluoreszenz. *Annalen der Physik* **437**, 55-75 (1948)10.1002/andp.19484370105).
26. R. Y. Tsien, Indicators based on fluorescence resonance energy transfer (FRET). *Cold Spring Harbor protocols* **2009**, pdb top57 (2009); published online EpubJul (10.1101/pdb.top57).
27. Y. Ueda, S. Kwok, Y. Hayashi, Application of FRET probes in the analysis of neuronal plasticity. *Front Neural Circuits* **7**, 163 (2013)10.3389/fncir.2013.00163).
28. P. J. Campagnola, L. M. Loew, Second-harmonic imaging microscopy for visualizing biomolecular arrays in cells, tissues and organisms. *Nature biotechnology* **21**, 1356-1360 (2003); published online EpubNov (10.1038/nbt894).
29. N. Heim, O. Garaschuk, M. W. Friedrich, M. Mank, R. I. Milos, Y. Kovalchuk, A. Konnerth, O. Griesbeck, Improved calcium imaging in transgenic mice expressing a troponin C-based biosensor. *Nat.Methods* **4**, 127-129 (2007).
30. V. Siffrin, H. Radbruch, R. Glumm, R. Niesner, M. Paterka, J. Herz, T. Leuenberger, S. M. Lehmann, S. Luenstedt, J. L. Rinnenthal, G. Laube, H. Luche, S. Lehnardt, H. J. Fehling, O. Griesbeck, F. Zipp, In vivo imaging of partially reversible th17 cell-induced neuronal dysfunction in the course of encephalomyelitis. *Immunity* **33**, 424-436 (2010).
31. H. Luche, O. Weber, T. Nageswaraâ€„Rao, C. Blum, H. Fehling, Faithful activation of an extra-bright red fluorescent protein in â€œknock-inâ€ reporter mice ideally suited for lineage tracing studies. *European Journal of Immunology* **37**, 43-53 (2007).
32. B. E. Clausen, C. Burkhardt, W. Reith, R. Renkawitz, I. Forster, Conditional gene targeting in macrophages and granulocytes using LysMcre mice. *Transgenic Res* **8**, 265-277 (1999); published online EpubAug (
33. A. Nimmerjahn, F. Helmchen, In vivo labeling of cortical astrocytes with sulforhodamine 101 (SR101). *Cold Spring Harbor protocols* **2012**, 326-334 (2012); published online EpubMar (10.1101/pdb.prot068155).
34. A. Nimmerjahn, F. Kirchhoff, J. N. Kerr, F. Helmchen, Sulforhodamine 101 as a specific marker of astroglia in the neocortex in vivo. *Nature methods* **1**, 31-37 (2004); published online EpubOct (10.1038/nmeth706).
35. R. Niesner, V. Siffrin, F. Zipp, Two-photon imaging of immune cells in neural tissue. *Cold Spring Harbor protocols* **2013**, (2013); published online EpubMar (10.1101/pdb.prot073528).
36. D. Buck, B. Hemmer, Treatment of multiple sclerosis: current concepts and future perspectives. *Journal of neurology* **258**, 1747-1762 (2011); published online EpubOct (10.1007/s00415-011-6101-2).
37. D. B. Clifford, A. De Luca, D. M. Simpson, G. Arendt, G. Giovannoni, A. Nath, Natalizumab-associated progressive multifocal leukoencephalopathy in patients with multiple sclerosis: lessons from 28 cases. *The Lancet. Neurology* **9**, 438-446 (2010); published online EpubApr (10.1016/S1474-4422(10)70028-4).
38. J. Herz, M. Paterka, R. A. Niesner, A. U. Brandt, V. Siffrin, T. Leuenberger, J. Birkenstock, A. Mossakowski, R. Glumm, F. Zipp, H. Radbruch, In vivo imaging of lymphocytes in the CNS

reveals different behaviour of naive T cells in health and autoimmunity. *Journal of neuroinflammation* **8**, 131 (2011)10.1186/1742-2094-8-131).

39. E. H. Wilson, T. H. Harris, P. Mrass, B. John, E. D. Tait, G. F. Wu, M. Pepper, E. J. Wherry, F. Dzierzinski, D. Roos, P. G. Haydon, T. M. Laufer, W. Weninger, C. A. Hunter, Behavior of parasite-specific effector CD8+ T cells in the brain and visualization of a kinesis-associated system of reticular fibers. *Immunity* **30**, 300-311 (2009); published online EpubFeb 20 (10.1016/j.immuni.2008.12.013).
40. J. L. Rinnenthal, C. Bornchen, H. Radbruch, V. Andresen, A. Mossakowski, V. Siffrin, T. Seelemann, H. Spiecker, I. Moll, J. Herz, A. E. Hauser, F. Zipp, M. J. Behne, R. Niesner, Parallelized TCSPC for dynamic intravital fluorescence lifetime imaging: quantifying neuronal dysfunction in neuroinflammation. *PLoS One* **8**, e60100 (2013)10.1371/journal.pone.0060100).
41. H. Radbruch, D. Bremer, R. Mothes, R. Gunther, J. L. Rinnenthal, J. Pohlan, C. Ulbricht, A. E. Hauser, R. Niesner, Intravital FRET: Probing Cellular and Tissue Function in Vivo. *International journal of molecular sciences* **16**, 11713-11727 (2015)10.3390/ijms160511713).
42. A. A. Mossakowski, J. Pohlan, D. Bremer, R. Lindquist, J. M. Millward, M. Bock, K. Pollok, R. Mothes, L. Viohl, M. Radbruch, J. Gerhard, J. Bellmann-Strobl, J. Behrens, C. Infante-Duarte, A. Mahler, M. Boschmann, J. L. Rinnenthal, M. Fuchtemeier, J. Herz, F. C. Pache, M. Bardua, J. Priller, A. E. Hauser, F. Paul, R. Niesner, H. Radbruch, Tracking CNS and systemic sources of oxidative stress during the course of chronic neuroinflammation. *Acta neuropathologica*, (2015); published online EpubOct 31 (10.1007/s00401-015-1497-x).
43. C. Iarlori, D. Gambi, A. Lugaresi, A. Patruno, M. Felaco, M. Salvatore, L. Speranza, M. Reale, Reduction of free radicals in multiple sclerosis: effect of glatiramer acetate (Copaxone). *Multiple sclerosis* **14**, 739-748 (2008); published online EpubJul (10.1177/1352458508088918).
44. A. S. Basso, D. Frenkel, F. J. Quintana, F. A. Costa-Pinto, S. Petrovic-Stojkovic, L. Puckett, A. Monsonego, A. Bar-Shir, Y. Engel, M. Gozin, H. L. Weiner, Reversal of axonal loss and disability in a mouse model of progressive multiple sclerosis. *J Clin Invest* **118**, 1532-1543 (2008); published online EpubApr (10.1172/JCI33464).
45. C. M. Rice, M. Sun, K. Kemp, E. Gray, A. Wilkins, N. J. Scolding, Mitochondrial sirtuins--a new therapeutic target for repair and protection in multiple sclerosis. *Eur J Neurosci* **35**, 1887-1893 (2012); published online EpubJun (10.1111/j.1460-9568.2012.08150.x).
46. R. J. Fox, Primary neuroprotection: the Holy Grail of multiple sclerosis therapy. *Neurology* **74**, 1018-1019 (2010); published online EpubMar 30 (10.1212/WNL.0b013e3181d6b165).
47. S. Sriram, I. Steiner, Experimental allergic encephalomyelitis: a misleading model of multiple sclerosis. *Annals of neurology* **58**, 939-945 (2005); published online EpubDec (10.1002/ana.20743).
48. Z. Nayernia, V. Jaquet, K. H. Krause, New Insights on NOX Enzymes in the Central Nervous System. *Antioxid Redox Signal*, (2014); published online EpubJan 16 (10.1089/ars.2013.5703).
49. R. B. Banati, J. Gehrmann, P. Schubert, G. W. Kreutzberg, Cytotoxicity of microglia. *Glia* **7**, 111-118 (1993); published online EpubJan (10.1002/glia.440070117).
50. C. Schuh, I. Wimmer, S. Hametner, L. Haider, A. M. Van Dam, R. S. Liblau, K. J. Smith, L. Probert, C. J. Binder, J. Bauer, M. Bradl, D. Mahad, H. Lassmann, Oxidative tissue injury in multiple sclerosis is only partly reflected in experimental disease models. *Acta neuropathologica* **128**, 247-266 (2014); published online EpubAug (10.1007/s00401-014-1263-5).
51. H. Sumimoto, K. Miyano, R. Takeya, Molecular composition and regulation of the Nox family NAD(P)H oxidases. *Biochemical and biophysical research communications* **338**, 677-686 (2005); published online EpubDec 9 (10.1016/j.bbrc.2005.08.210).
52. H. J. Forman, M. Torres, Reactive oxygen species and cell signaling: respiratory burst in macrophage signaling. *Am J Respir Crit Care Med* **166**, S4-8 (2002); published online EpubDec 15 (10.1164/rccm.2206007).

EIDESSTATTLICHE VERSICHERUNG

„Ich, Agata Anna Mossakowski, versichere an Eides statt durch meine eigenhändige Unterschrift, dass ich die vorgelegte Dissertation mit dem Thema „*Funktionelle Echtzeitanalyse der zellulären und molekularen Mechanismen der neuronalen Dysfunktion in chronischer Neuroinflammation*“ selbstständig und ohne nicht offengelegte Hilfe Dritter verfasst und keine anderen als die angegebenen Quellen und Hilfsmittel genutzt habe.

Alle Stellen, die wörtlich oder dem Sinne nach auf Publikationen oder Vorträgen anderer Autoren beruhen, sind als solche in korrekter Zitierung (siehe „Uniform Requirements for Manuscripts (URM)“ des ICMJE -*www.**icmje**.org*) kenntlich gemacht. Die Abschnitte zu Methodik (insbesondere praktische Arbeiten, Laborbestimmungen, statistische Aufarbeitung) und Resultaten (insbesondere Abbildungen, Graphiken und Tabellen) entsprechen den URM (s.o) und werden von mir verantwortet.

Meine Anteile an den ausgewählten Publikationen entsprechen denen, die in der untenstehenden gemeinsamen Erklärung mit dem/der Betreuer/in, angegeben sind. Sämtliche Publikationen, die aus dieser Dissertation hervorgegangen sind und bei denen ich Autor bin, entsprechen den URM (s.o) und werden von mir verantwortet.

Die Bedeutung dieser eidesstattlichen Versicherung und die strafrechtlichen Folgen einer unwahren eidesstattlichen Versicherung (§156,161 des Strafgesetzbuches) sind mir bekannt und bewusst.“

_____

Datum Unterschrift

ANTEILSERKLÄRUNG AN DEN ERFOLGTEN PUBLIKATIONEN

Agata Anna Mossakowski hatte folgenden Anteil an den folgenden Publikationen:

Publikation 1: „*In vivo* imaging of lymphocytes in the CNS reveals different behaviour of naïve T cells in health and autoimmunity“

Josephine Herz, Magdalena Paterka, Raluca A Niesner, Alexander U Brandt, Volker Siffrin, Tina Leuenberger, Jerome Birkenstock, **Agata Mossakowski**, Robert Glumm, Frauke Zipp und Helena Radbruch,

Journal of Neuroinflammation, 2011

Beitrag im Einzelnen: Erhebung der Primärdaten (intravitale und in vitro Zweiphotonenmikroskopie mit SHG-Messung, Zellkulturen und Stimulationsreihen), Auswertung der Daten, Beteiligung an Verfassung der Manuskriptes.

Publikation 2: “Parallelized TCSPC for Dynamic Intravital Fluorescence Lifetime Imaging: Quantifying Neuronal Dysfunction in Neuroinflammation”

Jan Leo Rinnenthal, Christian Börnchen, Helena Radbruch, Volker Andresen, **Agata Mossakowski,** Volker Siffrin, Thomas Seelemann, Heinrich Spiecker, Ingrid Moll, Josephine Herz, Anja E. Hauser, Frauke Zipp, Martin J. Behne und Raluca Niesner,

PLOS one, 2013

Beitrag im Einzelnen: Erhebung der Primärdaten (intravitale und in vitro Zweiphotonenmikroskopie mit Fluoreszenzlebensdauermessung), Auswertung der Daten.

Publikation 3: „Tracking CNS and systemic sources of oxidative stress during the course of chronic neuroinflammation“

Agata A. Mossakowski, Julian Pohlan, Daniel Bremer, Randall Lindquist, Jason M. Millward, Markus Bock, Karolin Pollok, Ronja Mothes, Leonard Viohl, Moritz Radbruch,

Jenny Gerhard, Judith Bellmann-Strobl, Janina Behrens, Carmen Infante-Duarte, Anja Mähler, Michael Boschmann, Jan Leo Rinnenthal, Martina Füchtemeier, Josephine Herz, Florence C. Pache, Markus Bardua, Josef Priller, Anja E. Hauser, Friedemann Paul, Raluca Niesner, Helena Radbruch

Acta Neuropathologica, 2015

Beitrag im Einzelnen: Studiendesign und Versuchsaufbau, Erhebung der Primärdaten (intravitale und in vitro Zweiphotonenmikroskopie mit Fluoreszenzlebensdauermessung, Zellisolation, Validierung und Optimierung der in vitro-Messungen), Auswertung der Daten, Verfassung der Manuskriptes.

Unterschrift der Doktorandin

_____

DRUCKEXEMPLARE DER AUSGEWÄHLTEN PUBLIKATIONEN

JOURNAL OF NEUROINFLAMMATION

RESEARCH Open Access

In vivo imaging of lymphocytes in the CNS reveals different behaviour of naïve T cells in health and autoimmunity

Josephine Herz[1,7], Magdalena Paterka[2,7], Raluca A Niesner[3,7], Alexander U Brandt[4,7], Volker Siffrin[2,7], Tina Leuenberger[2,7], Jerome Birkenstock[2], Agata Mossakowski[3], Robert Glumm[5,7], Frauke Zipp[2,7] and Helena Radbruch[6,7*]

Abstract

Background: Two-photon laser scanning microscopy (TPLSM) has become a powerful tool in the visualization of immune cell dynamics and cellular communication within the complex biological networks of the inflamed central nervous system (CNS). Whereas many previous studies mainly focused on the role of effector or effector memory T cells, the role of naïve T cells as possible key players in immune regulation directly in the CNS is still highly debated.

Methods: We applied *ex vivo* and intravital TPLSM to investigate migratory pathways of naïve T cells in the inflamed and non-inflamed CNS. MACS-sorted naïve CD4+ T cells were either applied on healthy CNS slices or intravenously injected into RAG1 -/- mice, which were affected by experimental autoimmune encephalomyelitis (EAE). We further checked for the generation of second harmonic generation (SHG) signals produced by extracellular matrix (ECM) structures.

Results: By applying TPLSM on living brain slices we could show that the migratory capacity of activated CD4+ T cells is not strongly influenced by antigen specificity and is independent of regulatory or effector T cell phenotype. Naïve T cells, however, cannot find sufficient migratory signals in healthy, non-inflamed CNS parenchyma since they only showed stationary behaviour in this context. This is in contrast to the high motility of naïve CD4+ T cells in lymphoid organs. We observed a highly motile migration pattern for naïve T cells as compared to effector CD4+ T cells in inflamed brain tissue of living EAE-affected mice. Interestingly, in the inflamed CNS we could detect reticular structures by their SHG signal which partially co-localises with naïve CD4+ T cell tracks.

Conclusions: The activation status rather than antigen specificity or regulatory phenotype is the central requirement for CD4+ T cell migration within healthy CNS tissue. However, under inflammatory conditions naïve CD4+ T cells can get access to CNS parenchyma and partially migrate along inflammation-induced extracellular SHG structures, which are similar to those seen in lymphoid organs. These SHG structures apparently provide essential migratory signals for naïve CD4+ T cells within the diseased CNS.

Keywords: naïve, T-cell, migration, EAE, second harmonic generation

1. Background

In the last 10 years, two-photon laser scanning microscopy (TPLSM) has revealed the dynamic nature of immune cells within living lymphoid and target organs [1-6]. This has led not only to a better understanding of generation and priming of many immune cells, but also of the basics of immune regulation.

Using TPLSM, we previously showed that activated CD4+ effector T cells are attracted to the CNS's perivascular space and reveal a CXCR4 dependent and vessel-associated migration pattern, suggesting this compartment is highly relevant for autoimmunity and immunoregulation [3,7]. While previous studies of ours as well as other studies mainly concentrated on T cells in their effector or effector-memory state, in the current study

* Correspondence: helena.radbruch@charite.de
[6]Labor für Molekulare Psychiatrie, Charité and Berlin-Brandenburg School for Regenerative Therapies (BSRT), Charité Universitätsmedizin Berlin, Charitéplatz 1, 10117 Berlin, Germany
Full list of author information is available at the end of the article

BioMed Central

© 2011 Herz et al; licensee BioMed Central Ltd. This is an Open Access article distributed under the terms of the Creative Commons Attribution License (http://creativecommons.org/licenses/by/2.0), which permits unrestricted use, distribution, and reproduction in any medium, provided the original work is properly cited.

we focused on the behaviour of naïve and regulatory T cells.

Activated and memory T cells express adhesion molecules, chemokine receptors and integrins that enable them to cross the blood brain barrier to carry out immune surveillance of the CNS [7]. Adversely, naïve T cells which do not express essential proteolytic enzymes (e.g. matrix metalloproteinases) and adhesion ligands (e.g. LFA-1 and VLA-4), were thought to circulate only between the blood, lymph and secondary lymphoid organs. However, flow cytometry experiments showed that naïve T cells can indeed be found in the healthy, non-inflamed CNS [8,9]. This is also the case for other non-lymphoid tissues including the pancreas, intestine, lung, liver, kidney, skin and testis, where it is thought that this circulation is part of the normal migratory behaviour of naïve T cells [8]. During CNS- inflammation adhesion ligands (i.e. ICAM-1 and VCAM) facilitate T cell recruitment to the CNS [10-12], and they only get activated when they encounter their antigen in the CNS [13].

Naïve T cells could therefore be potential players in CNS immunoregulation and fulfil an important role both in physiological immune surveillance and in pathological autoimmune processes, such as those which occur during Multiple Sclerosis or experimental autoimmune encephalomyelitis (EAE). However, this raises the question how these T cells can migrate through structures of normal tissue in the absence of inflammatory conditions. This is particularly unclear in the CNS in which there is an intricate architecture of neurons, myelinated axons, oligodendrocytes, astrocytes and microglia. Furthermore, the CNS includes a highly complex, extracellular matrix which provides both structural stability and supports homeostasis of the cellular components. Conventional histological examinations offer insights into these questions, but lack the capacity to directly address kinetics, dynamics and functional relevance of T cell trafficking.

Hence, in the current study we applied intravital TPLSM to investigate migratory pathways of naïve T cells in healthy and inflamed CNS.

2. Methods

2.1. Mice

C57BL/6 mice and C57BL/6 pups were purchased from Charles River (Germany). *β-actin-EGFP* transgenic C57BL/6 (003291, C57BL/6-Tg(ACTB-EGFP)1Osb/J), *OT-2* (C57BL/6-Tg(TcraTcrb)425Cbn) transgenic mice and *RAG1 -/-* transgenic C57Bl/6 (002216, B6.129S7-Rag1tm1Mom/J) were originally obtained from The Jackson Laboratory (Maine, USA), bred under SPF conditions at the central animal facility of the Charité - University Medicine Berlin (FEM), and kept in-house for experiments in IVC (individually ventilated cages).

C57BL/6 *OT2* mice, C57BL/6 *2d2 TCR* [14] transgenic mice (kindly provided by A. Waismann), C57BL/6 *Rosa26 tdRFP ("ΔNeo-flip")*mice [15], obtained from H.J. Fehling, or C57BL/6 *β-actin-EGFP* transgenic mice were intercrossed to generate C57BL/6 *OT2 tdRFP*, C57BL/6 *2d2 tdRFP* mice and C57BL/6 *OT2 EGFP* mice, respectively. C57BL/6 *Thy1-21 EGFP* [16] mice were kindly provided by P. Caroni, C57BL/6 *Thy1.1 CerTN L15* mice were kindly provided by O.Griesbeck [17] C57BL/6 *Foxp3 EGFP* mice were kindly provided by B. and M. Malissen.

All animal experiments were conducted according to the German Animal Protection Law, were approved by the appropriate state committees for animal welfare (LAGeSo, Landesamt für Gesundheit und Soziales) and were performed in accordance with current guidelines and regulations.

2.2. Cell culture

Mice (6-10 weeks old) were sacrificed and spleen cells were isolated as described before [3]. For OT-2 Th2 cells splenocytes were cultured in 3×10^6/ml cell culture medium (RPMI 1640 supplemented with 2 mM L-glutamine, 100 U/ml penicillin, 100 μg/ml streptomycin, and 10% fetal calf serum), and stimulated with the respective ovalbumin (OVA) peptide (0.3 μM $OVA_{323-339;}$ Pepceuticals, UK). Differentiation towards a Th2 phenotype of OT-2 cells was achieved by the addition of 200U/ml IL-4, 5 μg/ml anti-IL-12 (C17.8) and anti-IFN-γ (AN18.17.24). C57BL/6 Th1 cells were generated from CD4+ sorted spleen and lymph node cells (MACS®) of C57BL/6 mice by polyclonal activation by 1 μg/ml plate-bound antiCD3/antiCD28 in the presence of 5 ng/ml IL-12 and 5 μg/ml anti-IL-4 (11B11). Antigen specific and polyclonal effector T cells were restimulated every 7 days by irradiated syngenic CD90-depleted (MACS®) APCs or antiCD3/antiCD28, respectively. C57BL/6 Foxp3 expressing regulatory T cells were isolated either by MACS®sort for CD4, CD25 and CD62L or by FACS for Foxp3EGFP and CD62L. Cells were polyclonally activated by plate-bound antiCD3/antiCD28 (3/10) in round bottom 96 well plates in the presence of 2000 U IL-2. IL-10 producing Ovalbumin- or MOG-specific regulatory T cells were generated according to the protocol by Barrat et al.[18]. Briefly, naïve CD4+CD62L+T cells were stimulated with irradiated syngenic CD90depleted splenic APCs (MACS®) and 0.3 μM $OVA_{323-339}$ or 12,5 μg/ml MOG_{35-55} peptide in the presence of 40 nM Vitamin D3 and 100 nM Dexamethasone and 5 μg/ml anti-IL-12 (C17.8), anti-IFN-γ (AN18.17.24) and anti-IL 4 (11B11). Restimulation was done on day 7 with anti-CD3/anti-CD28. All analysed T cell subsets were stimulated for 3-7 days prior to hippocampal brain slice co-culture experiments. For characterization of T cell

phenotypes intracellular staining was performed on short term stimulated (4 h antiCD3/antiCD28) T cells on day 4-7 in order to analyse cytokine and Foxp3 expression by flow cytometry.

For T cells of naïve phenotype spleen and lymph node cells of OT2, OT2 EGFP or OT2 tdRFP mice were MACS®-sorted for CD4 and CD62L and used for i.v. injection for lymph node and intravital imaging of the brain stem or for application onto hippocampal brain slices.

2.3. Experimental Autoimmune Encephalomyelitis

For adoptive transfer EAE, spleen cells from C57BL/6 *2d2.tdRFP* or C57BL/6 *2d2.EGFP* mice were isolated and stimulated as previously described [19]. Three days after the second restimulation, 5×10^6 2d2.tdRF TH17 or 2d2.EGFP TH17 cells were transferred intravenously into C57BL/6 *RAG1*$^{-/-}$. Cytokine expression was checked on restimulation and before transfer. Mice were checked for clinical symptoms daily and signs of conventional EAE were translated into clinical score as follows: 0, no detectable signs of EAE; 0.5, tail weakness; 1, complete tail paralysis; 2, partial hind limb paralysis; 2.5, unilateral complete hind limb paralysis; 3, complete bilateral hind limb paralysis; 3.5, complete hind limb paralysis and partial forelimb paralysis; 4, total paralysis of forelimbs and hind limbs (mice with a score above 3.5 to be killed); 5, death. The severity of atypical EAE was translated as: grade 1, tail paralysis, hunched appearance; grade 2, ataxia, scruffy coat; grade 3, head tilt, hypersensitivity, spasticity or knuckling; grade 4, severe proprioception defects; grade 5, moribund.

For intravital imaging of naïve T cells MACS®-sorted naïve OT2 EGFP or OT2 tdRFP cells were co-transferred intravenously 12-24 hours before TPLSM or were locally applied on the imaging field at the peak of disease (score 2.5-3.5).

2.4. Two-photon laser scanning microscopy

T cells and vessels were visualised by a two-photon laser scanning system (LaVision BioTec, Bielefeld) as described before [20] with dual NIR (850 nm) and IR (1,110 nm) excitation. XYZ-stacks were typically collected within a scan field of 300 × 300 μm at 512 × 512 pixel resolution and a z-plane distance of 2 μm at a frequency of 400 or 800 Hz. Applied laser powers ranged from 2-6 mW at the specimen's surface.

2.5. Brain slice T cell co-culture

Preparation of brain slices was performed as previously described [3] and allowed to recover for at least 45 min at room temperature prior to transfer to a heated and with aerated artificial cerebrospinal fluid (ACSF) perfused Luigs & Neumann slice chamber (37°C). T cells, if not expressing EGFP or tdRFP, were stained with cell-tracker Orange CMTMR (Invitrogen, Germany), pipetted upon the slice and allowed to invade the slice for about 30 - 60 min before image acquisition.

2.6. Anaesthesia and preparation of imaging field for intravital imaging

Mice were anaesthetized using 1.5% isoflurane (Abott) in oxygen/nitrous oxide (1:2) with a facemask. They were then tracheotomized and continuously respirated with a Harvard Apparatus Advanced Safety Respirator (Hugo Sachs, Germany). For the brainstem imaging, the anaesthetized animal was transferred to a custom-built microscopy table and fixed in a hanging position. The preparation of the imaging field was performed as previously described [3].

2.7. Lymph node preparation for TPLSM

Lymph node preparation was performed as previously described [20]. In brief, 8-96 hours after intravenous injection of naïve OT2 EGFP or OT2 tdRFP T cells, popliteal lymph nodes were removed, glued onto a coverslip and placed into a heated chamber at 36°C, superfused RPMI medium without phenol red bubbled with 95%O2/5%CO2. Naïve T cell migration was visualised up to 130 μm beneath the surface using the same TPLSM setup as described above.

2.8. Data analysis

Cell recognition, movement tracking and 3D presentation were performed with Volocity (Improvision, Germany) and tracks with durations > 5 min. were included in the analysis. Average cell velocity was calculated with Volocity. The co-localisation area was calculated with Volocity as previously described [19]. To discriminate short/transient (random) contacts from long-lasting (most probably non-random) interactions, we defined contacts which last longer than 5 min as 'long-lasting'. These interactions were further differentiated into slow/static (velocity < 0.04 μm/s) and dynamic (velocity > 0.04 μm/s) contacts. In order to exclude the SHG signal which is detected with the same detector as EGFP in our setup, we increased the signal threshold so that only EGFP expressing cells (without any SHG signal) were automatically identified and tracked by the software. For angle comparison between cell trajectories and vessel structures and for vessel distance measurements at the end of the track, cell-tracking data from Volocity was further processed in MATLAB as described previously [3]. For each track, a vector between origin and endpoint was calculated in a two-dimensional angle and the distance between the cell-tracking vector and the vector representing the vessel was calculated using standard linear algebra. Statistical analysis was carried out with

SPSS (SPSS, Germany) and graphical presentation with GraphPad Prism 4 (Graphpad Software, USA). Results are shown as individual data points; in addition, mean ± SD summarize collective data from performed experiments. To test for statistical significance of differences between two T cell subpopulations, the non-parametric Mann-Whitney-test was performed for more than two groups Kruskal Wallis test with Dunn's multiple comparison test as post test was performed.

3. Results

3.1. Intravital imaging of the inflamed CNS of living mice reveals distinct migration pattern of naïve T lymphocytes

To observe naïve T cell migration under inflammatory circumstances in the CNS, we first performed flow cytometry analysis on brain-derived immune cells after transfer of naïve T cells, which are characterized by high CD62L and low CD69, CD25 and CD44 expression (Figure 1A), into EAE affected Rag 1-/- mice. For disease induction we transferred *in vitro* generated encephalitogenic 2d2 CD4+ TH17 cells (with transgenic T cell receptor specific for Myelin Oligodendrocyte Glycoprotein (MOG)). Some of the injected naïve T cells could be detected in the CNS but the cell number was too low to analyse activation markers and CD62L expression (data not shown). Therefore we used intravital TPLSM in the brainstem to record their behaviour. Using this approach it was possible to find naïve T cells up to 150 µm deep in the CNS parenchyma in EAE and to track their migration (Figure 1B). We used T cells with a

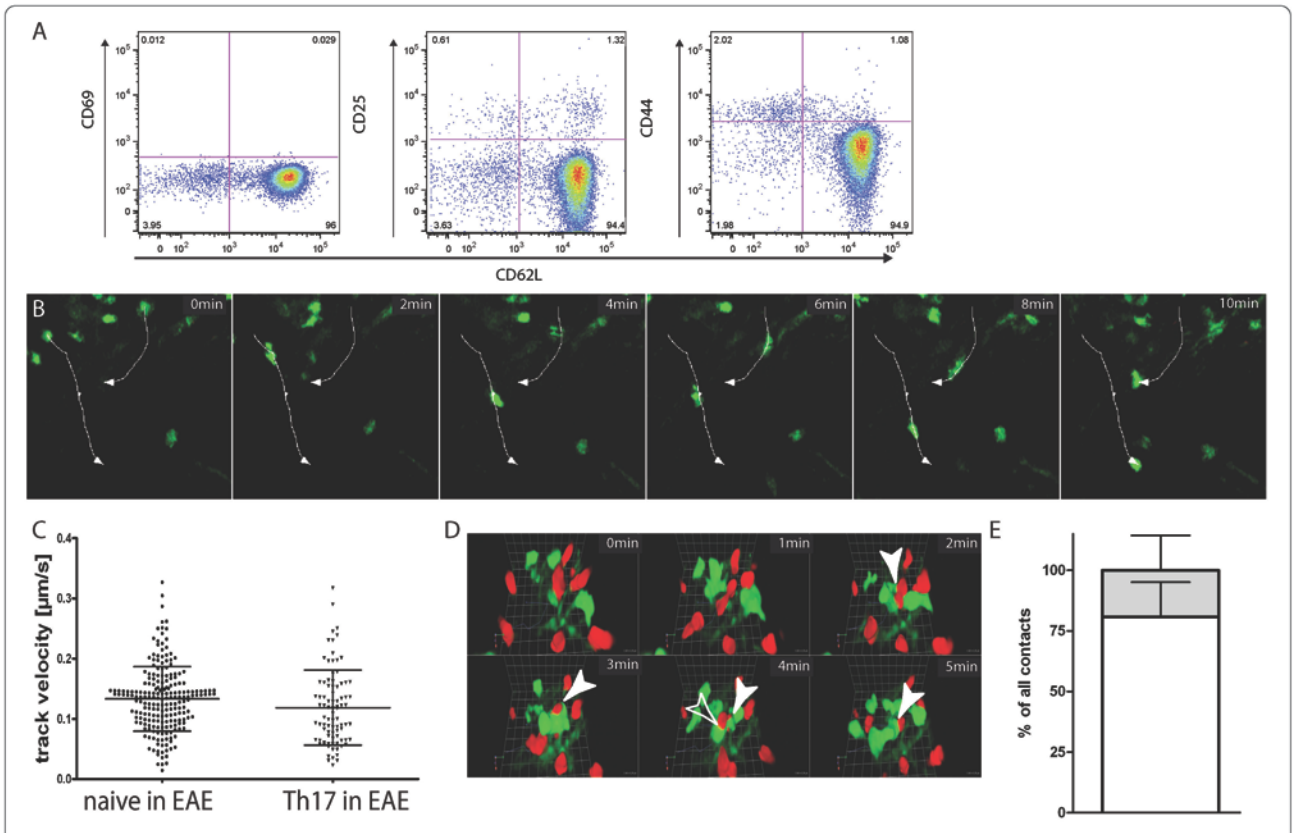

Figure 1 Intravital imaging reveals high motility of naïve CD4+ T cells in the inflamed CNS. Naïve OT2 EGFP T cells were intravenously injected into EAE affected mice at the peak of disease (clinical score 2.5) or locally applied onto the imaging field. Intravital TPLSM on the brain stem of these mice was performed 12 - 24 hours after naïve T cell injection or 30 minutes after local application. Adoptive EAE was induced by transfer of *in vitro* generated encephalitogenic 2d2 Th17 T cells into *C57BL/6 RAG1-/-* mice. **(A)** T cell phenotype of MACS isolated naïve T cells was confirmed by FACS analysis prior to experiments. Surface antigen expression of CD62L, CD25, CD69 and CD44 was determined on CD4+ lymphocytes. **(B)** A representative time lapse series derived from intravital TPLSM demonstrates rapid movement of naïve T cells deep in CNS tissue (100-150 µm). Two cell tracks are shown exemplarily by white arrows. For further details see also Additional File 1 (Scale bar: 10 µm.). **(C)** Cell track velocities of naïve OT2 (N = 212) and effector 2d2 Th17 (N = 87) cells at the peak of disease in the inflamed CNS were quantified. The mean track velocities from 4 independent experiments are shown (± SD). **(D)** Contacts (arrowheads) between encephalitogenic 2d2 Th17 effector T cells (EGFP,green) and naïve OT2 (tdRFP red) could be observed during intravital TPLSM, as revealed by the reconstructed 3D time lapse series (80-110 µm). These interactions were mainly short and random like (open arrowhead) although some static long-lasting contacts (filled arrowhead) could be also detected. **(E)** To quantify effector-naïve T cell interactions we analyse the co-localisation area of EGFP and tdRFP as previously described [19]. We discriminated short (random) contacts (< 5 min) from long-lasting (most probably non-random) interactions (≥ 5 min) and observed that 81% ± 14 formed short interactions with effector T cells (white bar) and 19% ± 14 (gray bar) formed long-lasting interactions. Data are shwon as percentage of all contacts from two independent experiments (± SD).

transgenic T cell receptor specific for Ovalbumin (OVA) to limit antigen specific activation on their way to and within the CNS. To further minimize activation, our timepoint of investigation was shortly after transfer (12 h for IV and 30 min for local application). Whereas we previously observed no lymphocytes in healthy mice deep in the CNS parenchyma we could detect some sporadic cells in the perivascular space [3]. However, during EAE naïve T cells were able to invade the parenchyma after local application on the brainstem or to cross the corrupted blood brain barrier after IV transfer and to move rapidly (Figure 1B, Additional File 1) resulting in a mean track velocity of 0.13 ± 0.05 μm/sec (± SD; N = 212) which was similar to that of encephalitogenic 2d2 CD4+ TH17 effector cells with 0.12 ± 0.06 μm/sec (±SD; N = 87) (Figure 1C). The dynamic interaction between both cell types was examined by co-localisation analysis as previously described [19]. We discriminated between short (random) contacts and long-lasting (most probably non-random). On their way through the parenchyma 19% of all contacts were of long-lasting nature whereas the majority (81 ± 14%) of the naïve-effector T cell interactions was short and random (Figure 1D/E).

3.2. Naïve CD4+ T cells do not get sufficient migratory signals in non-inflamed CNS tissue

As it was not possible to investigate the behaviour of naïve CD4+ T cells in healthy living anaesthetized mice due to the low frequency of lymphocytes after IV transfer [21], we circumvented the blood brain barrier and applied naive CD4 T cells on the brain stem of healthy living anaesthetized mice. The cells remained stucked on the surface or were flushed away with the perfusion (Additional File 2). We further co-incubated naïve T cells with brain tissue cultured in artificial cerebrospinal fluid (ACSF). These CNS slices have been shown to retain a middle layer which consists of intact *in vivo*-like CNS in murine brain cultures [22]. Naïve CD4+ T cells were labeled with the Celltracker Orange 5-(and-6)-(4-chloromethyl(benzoyl)amino) tetramethylrhodamine (CMTMR) if they were not transgenic for tdRFP or EGFP, and consecutively co-incubated with a living brain slice in which the vasculature had been highlighted by previous IV injection of FITC- or rhodamine-dextran. Independent of the need to transmigrate through the blood brain barrier, these cells showed a nearly stationary behaviour. The cell tracks were short and the cells seemed more or less trapped in their position on the slice surface after application on the non-inflamed CNS tissue (Figure 2A). This was quantified by a significantly lower mean track velocity with 0.056 ± 0.03 μm/sec (± SD; N = 86) as compared to activated CD4+ T cells (**$p < 0.01$). Furthermore the significantly reduced displacement rate of 0.019 ± 0.015 μm/sec (± SD) shows that they move on their place and do not invade the parenchyma (***$p < 0.01$) (Figure 2B).

3.3. Activated T helper cells infiltrate non-inflamed brain tissue independent of antigen specificity and phenotype and show a perivascular compartmentalisation

The stationary behaviour of naïve CD4+ T cells, as described above, is clearly a contrast to the migration pattern of activated CD4+ TH1 and CD4+ TH2 effector cells. We previously showed that CD4+ antigen specific, highly-activated and differentiated effector T cell lines show a vessel-associated movement pattern [3]. We wanted to check whether antigen specificity or regulatory phenotype would influence T cell migration. Therefore we performed T cell brain slice co-culture experiments as described above exemplarily for activated antigen specific (OT2 or 2d2) IL-10-producing regulatory and antigen specific (OT2) effector CD4+ TH2 cells as well as for polyclonally-activated Foxp3 T regulatory and CD4+ TH1 effector cells (Figure 3A). After an initial invasion period, the potential of tissue penetration was evident for all analysed activated T cell subsets as visualised by time lapse TPLSM. Furthermore, the migration pattern was similar in all investigated CD4+ T cell subtypes. The mean angle between vessel and cell trajectory vectors was similar in all investigated subgroups (Figure 3B, Figure 3C). The vessel-associated movement of CD4+ T cells in contrast to CD8+ T cells [3] seems also to be important for regulatory T cell subtypes independent of antigen specificity and underlines the importance of the perivascular space for immunoregulation and autoimmunity. Activated CD4+ T cells of regulatory phenotypes moved through non-inflamed CNS tissue with 0.07 ± 0.04 μm/s (± SD) for antigen-specific IL-10 producing regulatory T cells (N = 290) and 0.08 ± 0.04 μm/s (± SD) for C57Bl/6 Foxp3 CD4+ T cells (N = 215). Activated effector T cell subsets also revealed comparable mean track velocities, irrespective of antigen specificity and phenotype with 0.07 ± 0.0 μm/s (± SD) for OT2 Th2 (N = 290) and 0.07 ± 0.04 μm/s (± SD) for C57BL/6 Th1 (N = 248) cells (Figure 2B).

3.4. Naïve CD4+ T cells reveal high motility in healthy lymphoid organs

As control for the principle migratory capacity of naïve CD4+ T cells we injected MACS® sorted naïve OT2 cells intravenously into healthy mice and tracked their migration pattern in the lymph node (Figure 4). To check whether the cells were activated and primed after transfer we performed FACS analysis on injected cells and observed that these cells retain their $CD62L^{high}$ and $CD69^{low}$ phenotype up to 4 days after transfer (Figure 4A). We performed our experiments within this time

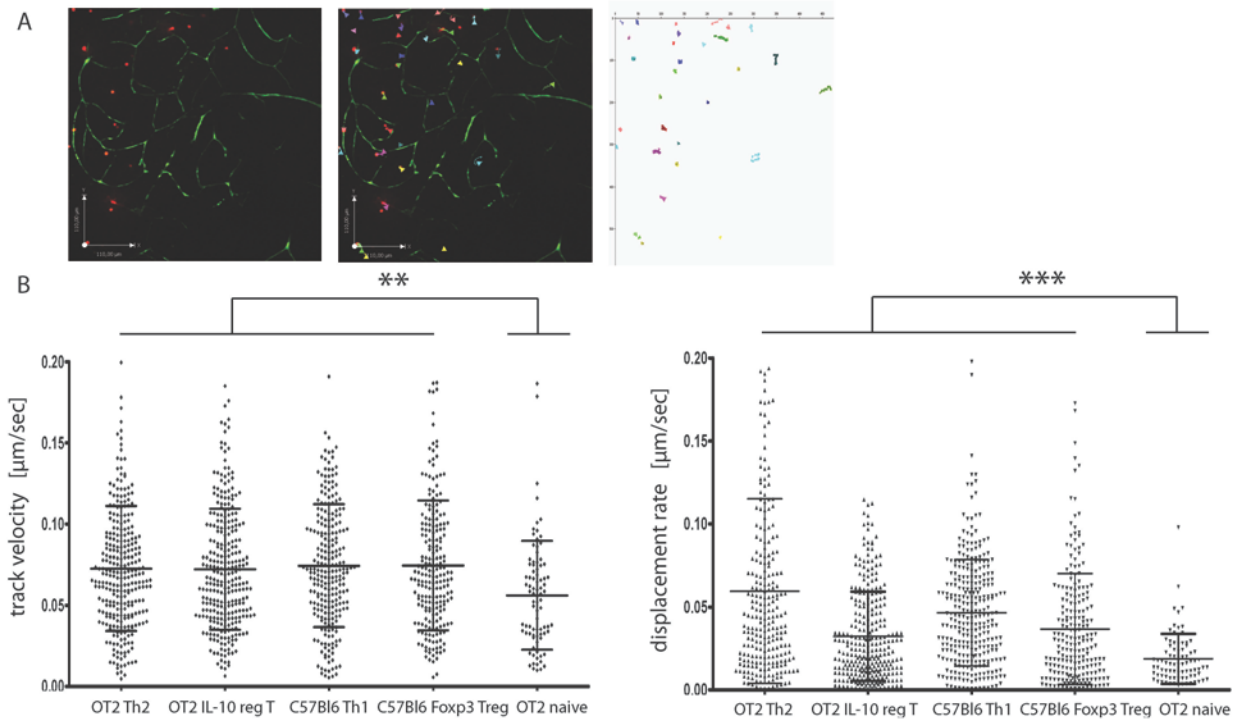

Figure 2 Naïve CD4+ T cells hardly infiltrate non-inflamed CNS tissue. MACS isolated CMTMR stained naïve T cells were co-incubated with living hippocampal brain slices in order to visualise their migratory capacity. **(A)** 3D time lapse TPLSM revealed a nearly stationary behaviour of naïve T lymphocytes. Cell tracking analysis of individual T cells confirmed these qualitative observations since the corresponding trajectory vectors display almost no displacement of naïve T lymphocytes. (Scale bar: 110 µm). **(B)** Track velocities and displacement rates for naïve T cells are compared with different activated T cell subsets (OT-2 Th2, OT-2/2d2 IL-10 reg T, C57BL6 Th1, C57BL6 Foxp3 Treg) using cell tracking analysis for individual cells of 2-6 independent experiments (± SD). **p < 0.01, ***p < 0.001, Kruskal Wallis Test.

frame. Time lapse TPLSM revealed high motility for naïve T cells (Figure 4B). Cell tracking analysis of individual T cells confirmed our qualitative observations, as the mean track velocity with 0.17 ± 0.06 µm/sec (± SD; N = 126) was similar to what was previously described by others [2] (Figure 4C).

3.5. Naïve T cells partially migrate along inflammatory induced reticular fibers in vivo

In lymphoid tissue it is known that naïve T cell motility is directed by fibroblastic reticular cells and ECM structures which can be visualised by second harmonic generation (SHG) [23]. Interestingly, we observed similar SHG signals which were generated by an optical parametric oscillator (OPO) at 1110 nm wavelength in the inflamed CNS of EAE affected mice. Moreover, naïve T cells partially moved along these structures (Figure 5A, Additional File 3). In order to objectify our observation we performed quantitative analysis for naïve T cell - SHG co-localization (Figure 5B/C). This analysis revealed that most of the contacts are short (81 ± 14%) but there is also a population of naive T cells that show long-lasting contacts with the reticular fiber network (19 ± 14%). These interactions were further differentiated into slow/static (velocity < 0.04 µm/s) and dynamic (velocity > 0.04 µm/s) contacts. Interestingly, these long-lasting contacts were due to migration associated co-localisation, since their velocity was > 0.04 µm/s supporting our qualitative observation that a distinct population of naïve T cells partially migrate along these inflammation induced fibers (Figure 5B/C).

The reticular fiber network was observed deep in the parenchyma (up 100 µm) and thus could be distinguished from the arachnoidea covering the surface of the brain stem parenchyma. Moreover, by visualisation of the vasculature by IV Rhodamine-dextrane injection prior to imaging we observed that in addition to the vessel associated collagen network surrounding the very close proximity of the vasculature further fiber tracts are generated deep in the parenchyma itself (Figure 5D).

We could not detect these structures under healthy conditions in the CNS parenchyma (Additional File 2). However, intravital TPLSM on the brain stem of EAE affected C57BL/6 *Thy1.1 CerTN L15* mice which express a FRET based calcium sensor, i.e. the Citrulin/Cerulean FRET pair (based on YFP/CFP) in neurons and neuronal

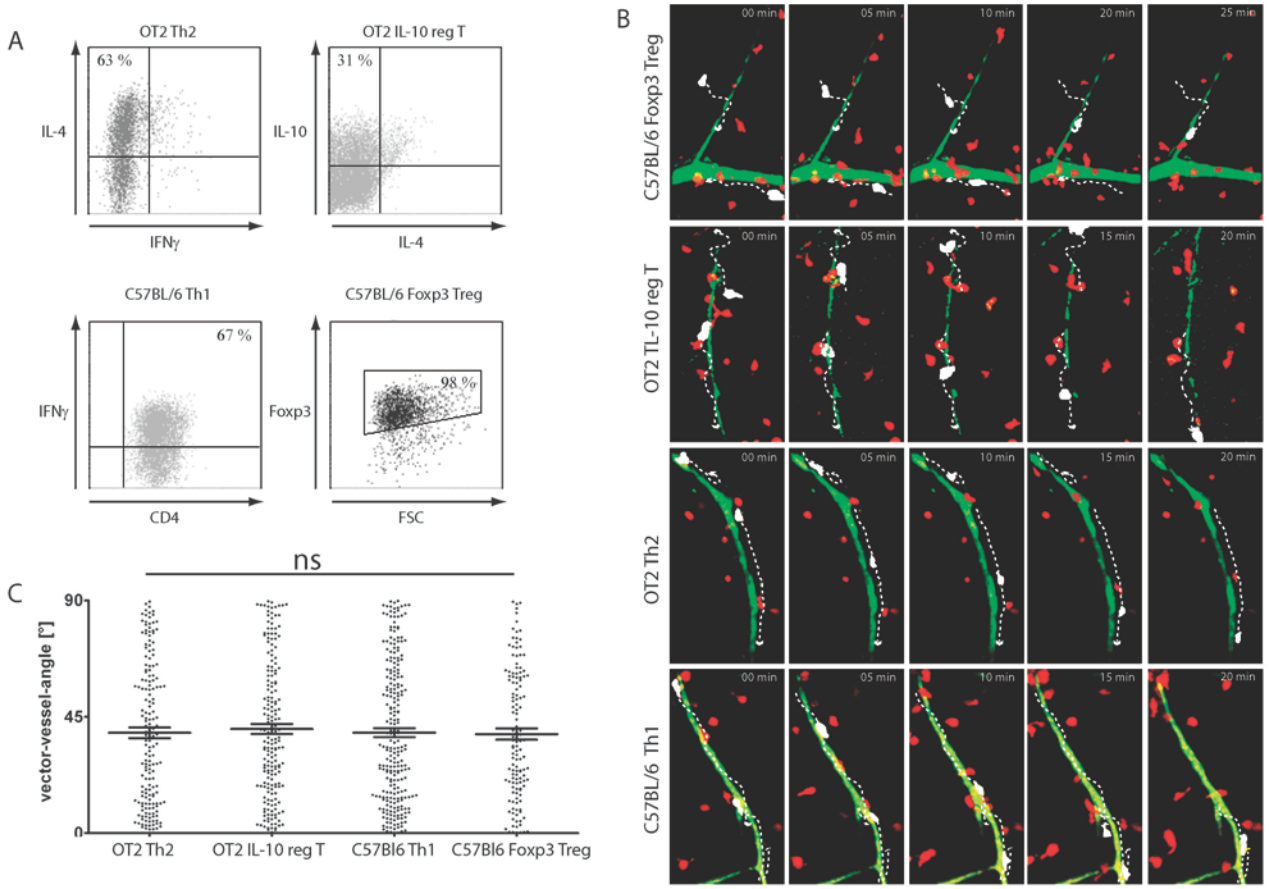

Figure 3 Activated regulatory and effector CD4+ T cells move rapidly in healthy CNS tissue independent of antigen specificity. T cell brain slice co-culture experiments were performed for activated antigen-specific IL-10 producing regulatory and effector CD4+ TH2 cells as well as for polyclonally activated Foxp3 regulatory and effector CD4+ TH1 cells. **(A)** T cell subsets were characterized by intracellular staining of typically expressed molecules for each cell type. For detection of interleukins, T cells were stimulated by aCD3/aCD28 (1 μg/ml) prior to staining. **(B)** Movement patterns of polyclonally and antigen-specific activated regulatory and effector T cells were analysed by time lapse TPLSM at 80-130 μm depth after an initial invasion period of 30-45 min. For each series, migratory routes of two exemplary cells (white) are represented by white arrows. **(C)** Vector vessel angels of individual cell tracks of different activated T cell subsets (OT-2 Th2, OT-2/2d2 IL-10 producing regulatory T cells, C57BL6 Th1, C57BL6 Foxp3 Treg) were calculated using cell tracking analysis for individual cells of 2-6 independent experiments per group (± SD). ns: not significant, Kruskal Wallis Test.

processes (axons and dendrites) [17], we could distinguish the generated SHG signal due to wavelength specificity of SHG (1110 nm) and separated excitation of Citrulin (850 nm). Using this approach we did not observe any co-localisation with the neuronal structures. In contrast, they appeared to cross the neuronal processes orthogonally, as visualised by merging fluorescence images acquired at both excitation wavelengths (Figure 5E).

4. Discussion

Unexpectedly, we observed a highly motile migration pattern for naïve T cells similar to effector T cells in the inflamed CNS of living EAE affected mice. However, we could further show that even though naïve T cells have migratory capacity in lymphoid organs and diseased CNS, they cannot find sufficient migratory signals in healthy non-inflamed CNS parenchyma since they only showed stationary behaviour in this environment. Using different experimental approaches, i.e. locally applied or IV transferred naive T cells, we could detect highly motile cells in the inflamed CNS parenchyma but no migration in healthy tissue supporting the hypothesis that the extend of inflammation is the crucial factor determining the possibility for naive T cells migration in the CNS parenchyma. Interestingly, in the inflamed CNS we could detect reticular structures by their SHG signal which was not detected in the non-inflamed CNS. These structures resemble those present in lymphoid tissues, suggesting that these inflammation-induced structures might provide the chemotactic signals needed for the naïve T cells to migrate within the diseased CNS.

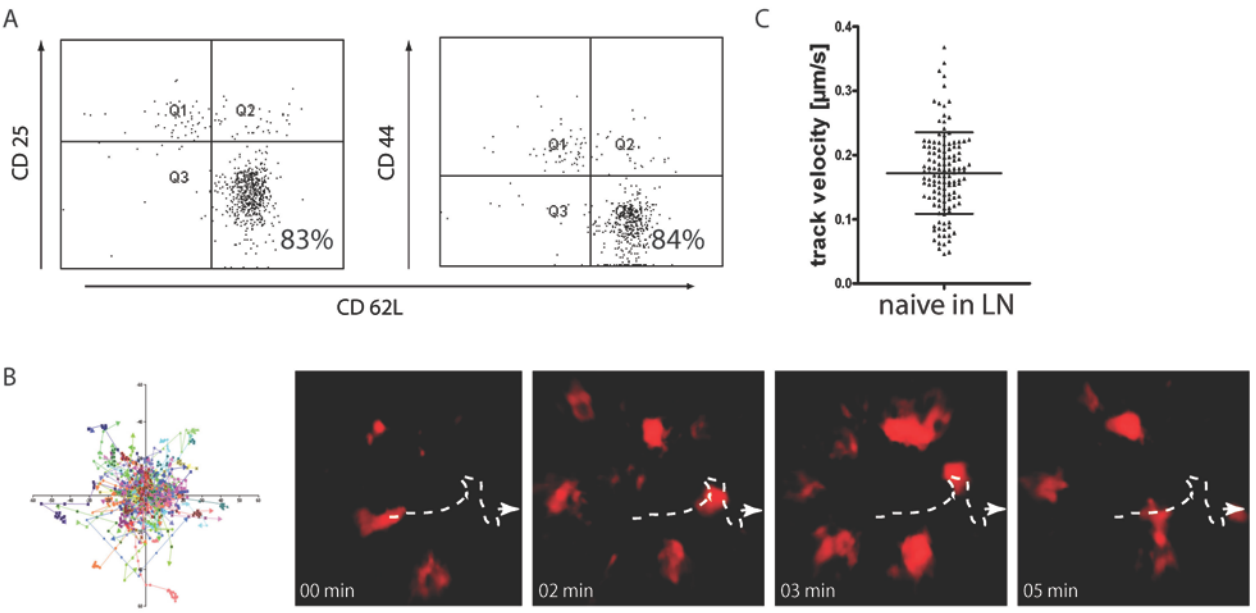

Figure 4 High motility of naïve CD4+ T cells in healthy lymphoid tissue. MACS® sorted OT2 tdRFP expressing CD4+ naïve T cells were intravenously injected into healthy *C57BL/6 RAG 1 -/-* mice in order to perform time lapse TPLSM on popliteal lymph nodes at 8 - 96 hours after transfer. **(A)** Injected OT2 tdRFP cells were isolated from lymph nodes of *C57BL/6 OT2 tdRFP* mice and subjected to FACS analysis to measure surface expression of CD62L, CD25, and CD44 at 96 hours after transfer. Dot Plots reveal analysis on CD4+ tdRFP positive lymphocytes. **(B)** High motility of naïve T lymphocytes in lymph nodes is revealed by trajectory vector blots derived from cell tracking analysis of time lapse TPLSM at 24 hours after transfer (left). Each vector represents displacement of individual cells for an imaging period of 30 min (one image every minute) relative to their starting position. A corresponding time lapse series of naïve cell migration is shown on the right. The dashed arrow represents migration of one single cell exemplarily. **(C)** Quantification of naïve CD4+ T cell movement in isolated lymph nodes. The mean track velocity is 0.16 ± 0.06 µm/sec (± SD, N = 73).

Little is known concerning the behaviour of naïve T cells in non-lymphoid organs under both homeostatic and inflammatory conditions in general. Regarding the CNS even less is known and most of the data are derived from flow cytometry studies of cells isolated from CNS tissue [8,9,13,24,25] or cerebrospinal fluid [26] and give contradictory results. Using an *in vivo* staining method, a recent study did not detect naïve CD4+ T cells in the brain at 4 days after transfer of naïve T cells [24]. In contrast experiments using an inverse transfer model (encephalitogenic cells into OVA specific T cell receptor transgenic mice) show that naïve endogenous T cells occur in parallel with activated encephalitogenic T cells but keep a resting phenotype unless they recognize their antigen in the CNS [13]. Similarly, McMahon et al. could only detect naïve PLP specific T cells in PLP immunized mice in contrast to OVA immunized controls. This supposes that naïve T cells can only enter the CNS if they get locally activated [25].

But in our study we could find naïve OVA specific CD4+ T cells in the inflamed CNS and using intravital TPLSM we could further show for the first time that naïve CD4+ T cells can indeed migrate rapidly through the CNS parenchyma, comparable to the way they move in lymphoid tissue. Due to the low frequency of naïve CD4 T cells compared to effector Th17 cells in the inflamed parenchyma it could be possible that they are not detected by flow cytometry after isolation. Therefore TPLSM could be used as complementary technique to analyse rare cell migration and further allows the investigation of dynamics.

The mean track velocity of naïve T cells was similar to the velocity of Th17 effector T cells. However, it remains unclear what role naïve T-cells play in the CNS. In MS naïve T cells are found in the cerebrospinal fluid during relapses [26] and the experiments from Brabb et al. support a possible function for the development of tolerance [9]: Using MBP (myelin basic protein)-recognizing T-cell receptor transgenic mice, they showed that naïve MBP-specific T cells isolated from the brain did not show any reactivity for MBP *in vitro*. On the other hand, MBP-specific naïve T cells from the periphery did react to MBP. Although we did not investigate the direct impact of naïve CD4+ T cells on function and behaviour of encephalitogenic T cells within the inflamed brain, our observation of direct contacts between naïve T cells and encephalitogenic T cells

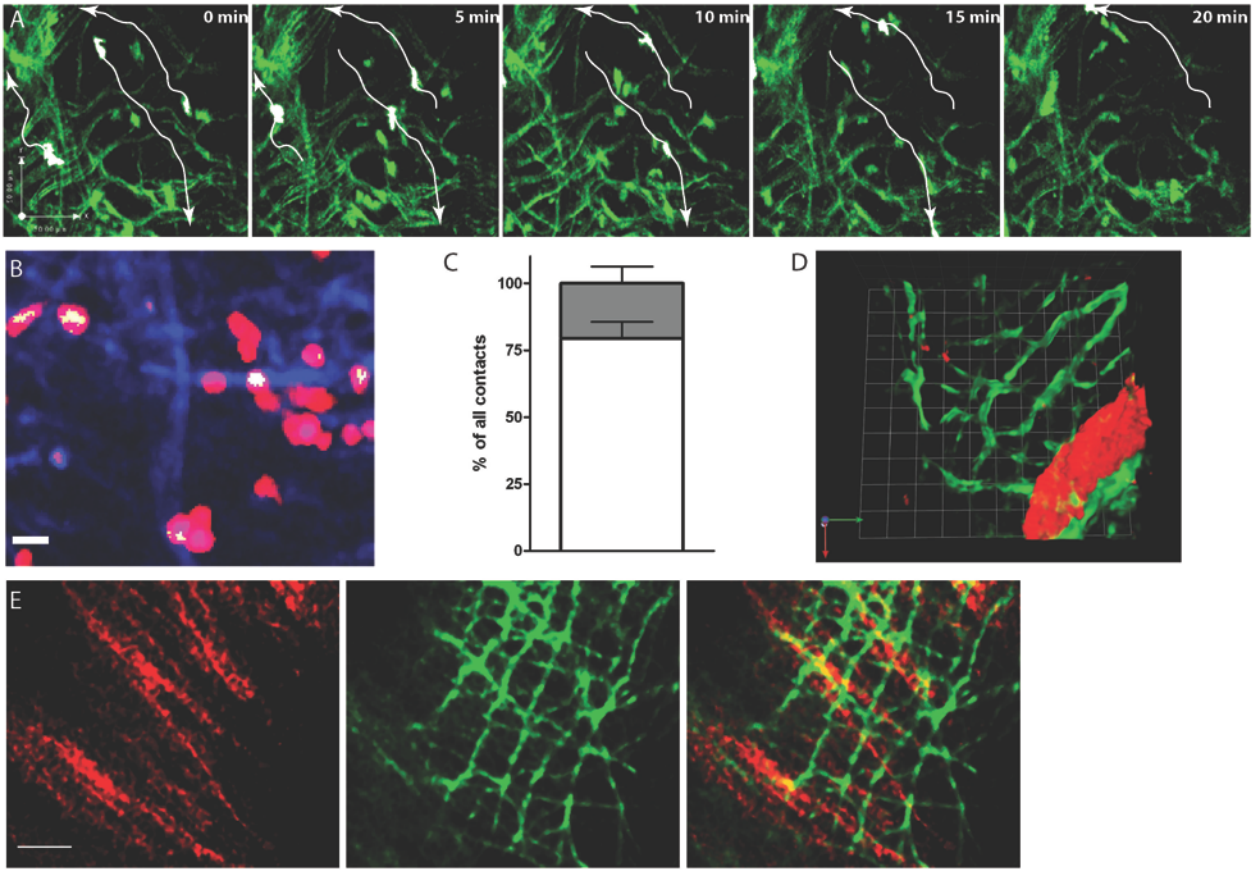

Figure 5 The role of inflammatory induced reticular fibers in naïve T cell migration in healthy and inflamed CNS tissue. **(A)** Intravital TPLSM reveals inflammation induced reticular fibers which are visualised by second harmonic generation (SHG) at 1110 nm wavelength in the brain stem of EAE affected mice. Naïve T cells partially migrate along SHG structures as demonstrated by cell tracks represented by white arrows exemplarily. For further details see also Additional File 3. **(B)** To quantify SHG signal and naïve T cell interactions we analyse the co-localisation area of SHG signal (blue) and tdRFP (red). The calculated colocalisation channel (white) was analyzed by determining the duration and the velocity of the tracked contacts (scale bar 10 μm). **(C)** Interaction patterns were differentiated into short (less than 5 min duration) and long-lasting contacts (equal or longer than 5 min duration,), Most of the contacts were short (79% ± 6; N = 164; white bar) but also long-lasting interactions could be detected (20 ± 6%; N = 38; gray bar) and that these long-lasting contacts are due to migration associated co-localisation as their velocity is > 0.04 μm/s. Data from two independent experiments are shown as percentage of all contacts (± SD). **(D)** Visualization of the vasculature by IV injection of Rhodamine-dextrane prior to imaging enabled the visualisation of both, the reticular structures (green) and vessels (red), simultaneously revealing that besides the vessel associated SHG signal a large amount of fibers originates directly from the CNS parenchyma outside the perivascular space. 1 unit = 15 μm **(E)** Intravital TPLSM on brain stem of EAE affected C57BL/6 *Thy1.1 CerTN L15* mice which express a FRET based calcium sensor. The Citrulin/Cerulean FRET pair is expressed in neurons and is detected by excitation at 850 nm (left, red) whereas SHG signal was generated by a separated excitation at 1110 nm (middle, green), which does not allow to detect either Citrulin or Cerulean. Images are presented in false colors in order to increase the contrast between both separately detected structures. Merge of both images derived from different excitation modes in the same layer demonstrates that the SHG signal (green) is not co-localised to neuronal structures (red). These images are derived form the same layer at a depth of 60 μm below the surface. Scale bar 30 μm.

suggests a possible direct impact. It remains to be clarified whether naïve CD4+ T cells might be of regulatory phenotype and nature in the CNS, and could therefore provide an opportunity for a novel therapeutic approach in MS or other autoimmune diseases.

However, in order to develop new treatment strategies, it is essential to understand how CNS tissue itself regulates naïve T cell trafficking. In lymphoid tissue it is known that T cell motility is directed by fibroblastic reticular cells and ECM structures [23]. Similar reticular structures exist in peripheral tissues such as the liver or skin, but are absent from the non-inflamed brain [27-29]. The source of the ECM structures in the CNS during inflammatory conditions we could detect in this study, however, is unclear. The ECM seems to undergo significant structural changes in the CNS since we could only detect SHG structures under inflammatory conditions. Similarly, Wilson et al. showed a reticular fiber network the produces a SHG signal during *Toxoplasma gondii* infection [29]. SHG generated by excitation at

wavelengths of 1000-1500 nm in TPLSM has its origin from highly-ordered, non-centrosymmetric structures such as collagen [30]. As the SHG phenomenon gives no indication of the molecular nature of the structures, it remains unclear which fibers are generating this signal. In the study of Wilson et al. the SHG signal was co-localised with GFAP expressing astrocytes, but with a spatial separation, suggesting that the SHG signal originates from extracellular fiber networks [29]. Furthermore, they found no increased collagen type IV or type I induction but reticular structures by histology which co-localised with CCL21 under inflammatory conditions, suggesting that CCL21 could be one possible candidate, because it is also known that impaired neurons bind CCL21 on their surface [31]. However, as we investigated the co-localisation of neuronal structures and the SHG signal in EAE in transgenic mice expressing EGFP or Citrulin under the neuron specific Thy1 promoter, we could not detect any co-localisation. In contrast, we observed an orthogonal crossing of neuronal structures by the SHG signals, indicating that these structures are not generated by intermediate filaments inside axons or extra cellular matrix co-localised with axons *in vivo*.

Nevertheless, CCL21 bound to these reticular fibers, could be a signal for attracting naïve T cells: Woolf et al. compared soluble vs. matrix-bound CCL21 in an *in vitro* assay and showed that naïve T cells migrated only if the chemokine was matrix-bound [32]. Our experiments are consistent with these results and demonstrate *in vivo* relevance of the described phenomenon. Furthermore, our observations suggest that reticular fibers, analogous to those of the lymph node's ECM, may provide a scaffold that supports T cell migration in the inflamed brain.

5. Conclusions

The mechanisms of autoimmunity and tolerance in the brain are still not clear and the role of naïve T cells as possible key players in these complex processes is highly debated [33]. Due to methodological limitations in the past, there remains an ongoing discussion as to what extent naïve T cells enter the healthy non-inflamed versus the inflamed CNS parenchyma and what role they might have. For activated T cells, proteolytic enzymes like metalloproteinases, disintegrins or granzymes are known to enable migration through the inflamed brain tissue [12,34,35]. These enzymes may be even more important if the reticular fiber network is not as abundant, as it is the case under inflammatory conditions where it facilitates immune cell trafficking. In contrast naïve T cells express molecules that are important for migration to secondary lymphoid organs such as L-Selectin and CCR7 for CD4+ T cells [36]. So it was previously thought that they circulate between blood and secondary lymphoid organs exclusively [37,38].

With the opportunity of TPLSM and the availability of various fluorescent protein expressing transgenic mouse models, we are now able to directly visualise the presence and dynamic processes of different T cell subsets deep in CNS tissue in living animals. We show here that the activation status rather than the T cell phenotype and antigen specificity is the central requirement for the migratory capacity of T cells in healthy CNS tissue independent of transmigration-associated molecular interactions at the blood brain barrier. Even though naïve T cells show a high migratory capacity in lymphoid organs, it remains to be seen why they appear in inflamed CNS where they partially migrated along inflammation-induced extracellular SHG structures and which signals might be responsible for the observed high motility in diseased brain tissue of EAE affected mice.

Although further studies are required to define the composition of these reticular networks, targeting these structures might be a novel therapeutic approach to manage T cell-mediated inflammatory central nervous system diseases.

Additional material

Additional file 1: Naïve T cells do not migrate into healthy CNS tissue *in vivo*. Time lapse movie of naïve tdRFP expressing OT2 T cells 30 min after local application on the brain stem of a healthy mouse.

Additional file 2: Movement of naïve T cells in the brain stem during EAE. Timelapse movie of naïve EGFP expressing OT-2 T cells in the brain stem at peak of disease. Cells were MACS sorted for CD4 and CD62L and transferred intravenously to EAE affected mice at peak of disease. Analysis was performed 12 h after transfer.

Additional file 3: SHG structures are induced in the inflamed CNS and naïve T cells partially migrate along these structures. Timelapse movie of naïve EGFP expressing OT-2 T cells at peak of disease. Cells were MACS sorted for CD4 and CD62L and transferred intravenously to EAE affected mice at peak of disease. Analysis was performed 12 h after transfer. Second harmonic generated signal was also detected in the 535/50 nm PMT and is displayed as a reticular structure.

8. Acknowledgements

We thank A. Waisman for providing the C57BL/6 *2d2 TCR* transgenic mice; P. Caroni for providing the C57BL/6 *Thy1-21 EGFP* transgenic mice; O.Griesbeck for providing the C57BL/6 *Thy1.1 CerTN L15* mice and H. Luche and H. J. Fehling for providing the C57BL/6 *Rosa-tdRFP* knock-in mice. We thank J. Millward for the fruitful discussions of the manuscript. This work was supported by grants from the German Research Foundation: the Graduate Research School GRK1258 to JH and TL; SFB-TRR 43 to FZ, DFG Ni1167/2-1 to RN, through Berlin-Brandenburg School for Regenerative Therapies for HR and from the Charité Universitätsmedizin Berlin through Rahel Hirsch Grant to RN. We thank Natalie Asselborn and Robert Günther for expert technical support and Sara Duke for reading the manuscript as a native speaker.

Author details

[1]Klinik für Neurologie, Universitätsklinik Essen, Hufelandstr. 55, 45122 Essen, Germany. [2]Universiätsmedizin Mainz, Klinik für Neurologie, Langenbeckstr 1, 55131 Mainz, Germany. [3]Deutsches Rheuma-Forschungszentrum (DRFZ),

Berlin, Charitéplatz 1, 10117 Berlin, Germany. [4]gfnmediber GmbH, Sophie Charlottenstr 92-94, 14059 Berlin, Germany. [5]Experimental and Clinical Research Center, a joint cooperation between the Charité Medical Faculty and the Max-Delbrück Center for Molecular Medicine, Berlin, Germany, Robert-Rössle Str 10 13092 Berlin, Germany. [6]Labor für Molekulare Psychiatrie, Charité and Berlin-Brandenburg School for Regenerative Therapies (BSRT), Charité Universitätsmedizin Berlin, Charitéplatz 1, 10117 Berlin, Germany. [7]Max-Delbrueck Center for Molecular Medicine Berlin-Buch, Robert-Rössle Str 10 13092 Berlin, Germany.

Authors' contributions

JH was responsible for executing the research project and, together with HR, writing the manuscript. AUB performed the statistical analysis and assisted in editing the manuscript, RN, VS, TL, MP, JB, AM and RG assisted technically with research and data analysis. FZ contributed to the design of the experiments and assisted in editing the manuscript. HR directed all aspects of this research project including the experimental design, completion of statistical analysis, and writing of the manuscript. All authors read, critically revised and approved the final manuscript.

Competing interests

The authors declare that they have no competing interests.

Received: 18 May 2011 Accepted: 6 October 2011
Published: 6 October 2011

References

1. Cahalan MD, Parker I: **Choreography of Cell Motility and Interaction Dynamics Imaged by Two-Photon Microscopy in Lymphoid Organs.** *Annu Rev Immunol* 2008, **26**:585-626.
2. Miller MJ, Wei SH, Parker I, Cahalan MD: **Two-photon imaging of lymphocyte motility and antigen response in intact lymph node.** *Science* 2002, **296**:1869-1873.
3. Siffrin V, Brandt AU, Radbruch H, Herz J, Boldakowa N, Leuenberger T, Werr J, Hahner A, Schulze-Topphoff U, Nitsch R, Zipp F: **Differential immune cell dynamics in the CNS cause CD4+ T cell compartmentalization.** *Brain* 2009, **132**:1247-1258.
4. Nimmerjahn A, Kirchhoff F, Helmchen F: **Resting Microglial Cells Are Highly Dynamic Surveillants of Brain Parenchyma in Vivo.** *Science* 2005, **308**:1314-1318.
5. Germain RN, Miller MJ, Dustin ML, Nussenzweig MC: **Dynamic imaging of the immune system: progress, pitfalls and promise.** *Nat Rev Immunol* 2006, **6**:497-507.
6. Bartholomaus I, Kawakami N, Odoardi F, Schlager C, Miljkovic D, Ellwart JW, Klinkert WE, Flugel-Koch C, Issekutz TB, Wekerle H, Fluegel A: **Effector T cell interactions with meningeal vascular structures in nascent autoimmune CNS lesions.** *Nature* 2009, **462**:94-98.
7. Ransohoff RM, Kivisakk P, Kidd G: **Three or more routes for leukocyte migration into the central nervous system.** *Nat Rev Immunol* 2003, **3**:569-581.
8. Cose S, Brammer C, Khanna KM, Masopust D, Lefrancois L: **Evidence that a significant number of naive T cells enter non-lymphoid organs as part of a normal migratory pathway.** *Eur J Immunol* 2006, **36**:1423-1433.
9. Brabb T, von Dassow P, Ordonez N, Schnabel B, Duke B, Goverman J: **In situ tolerance within the central nervous system as a mechanism for preventing autoimmunity.** *J Exp Med* 2000, **192**:871-880.
10. Martin R, McFarland HF, McFarlin DE: **Immunological aspects of demyelinating diseases.** *Annu Rev Immunol* 1992, **10**:153-187.
11. Owens T, Renno T, Taupin V, Krakowski M: **Inflammatory cytokines in the brain: does the CNS shape immune responses?** *Immunol Today* 1994, **15**:566-571.
12. Cannella B, Cross AH, Raine CS: **Adhesion-related molecules in the central nervous system. Upregulation correlates with inflammatory cell influx during relapsing experimental autoimmune encephalomyelitis.** *Lab Invest* 1991, **65**:23-31.
13. Krakowski ML, Owens T: **Naive T lymphocytes traffic to inflamed central nervous system, but require antigen recognition for activation.** *Eur J Immunol* 2000, **30**:1002-1009.
14. Krishnamoorthy G, Lassmann H, Wekerle H, Holz A: **Spontaneous opticospinal encephalomyelitis in a double-transgenic mouse model of autoimmune T cell/B cell cooperation.** *J Clin Invest* 2006, **116**:2385-2392.
15. Luche H, Weber O, NageswaraΓÇäRao T, Blum C, Fehling H: **Faithful activation of an extra-bright red fluorescent protein in ΓÇ£knock-inΓÇØ Cre-reporter mice ideally suited for lineage tracing studies.** *European Journal of Immunology* 2007, **37**:43-53.
16. Feng G, Mellor RH, Bernstein M, Keller-Peck C, Nguyen QT, Wallace M, Nerbonne JM, Lichtman JW, Sanes JR: **Imaging Neuronal Subsets in Transgenic Mice Expressing Multiple Spectral Variants of GFP.** *Neuron* 2000, **28**:41-51.
17. Heim N, Garaschuk O, Friedrich MW, Mank M, Milos RI, Kovalchuk Y, Konnerth A, Griesbeck O: **Improved calcium imaging in transgenic mice expressing a troponin C-based biosensor.** *Nat Methods* 2007, **4**:127-129.
18. Barrat FJ, Cua DJ, Boonstra A, Richards DF, Crain C, Savelkoul HF, Waal-Malefyt R, Coffman RL, Hawrylowicz CM, O'Garra A: **In vitro generation of interleukin 10-producing regulatory CD4(+) T cells is induced by immunosuppressive drugs and inhibited by T helper type 1 (Th1)- and Th2-inducing cytokines.** *J Exp Med* 2002, **195**:603-616.
19. Siffrin V, Radbruch H, Glumm R, Niesner R, Paterka M, Herz J, Leuenberger T, Lehmann SM, Luenstedt S, Rinnenthal JL, Laube G, Luche H, Lehnardt S, Fehling H, Griesbeck O, Zipp F: **In vivo imaging of partially reversible th17 cell-induced neuronal dysfunction in the course of encephalomyelitis.** *Immunity* 2010, **33**:424-436.
20. Herz J, Siffrin V, Hauser AE, Brandt AU, Leuenberger T, Radbruch H, Zipp F, Niesner RA: **Expanding two-photon intravital microscopy to the infrared by means of optical parametric oscillator.** *Biophys J* 2010, **98**:715-723.
21. Kawakami N, Nagerl UV, Odoardi F, Bonhoeffer T, Wekerle H, Flugel A: **Live imaging of effector cell trafficking and autoantigen recognition within the unfolding autoimmune encephalomyelitis lesion.** *J Exp Med* 2005, **201**:1805-1814.
22. Nitsch R, Bechmann I, Deisz RA, Haas D, Lehmann TN, Wendling U, Zipp F: **Human brain-cell death induced by tumour-necrosis-factor-related apoptosis-inducing ligand (TRAIL).** *Lancet* 2000, **356**:827-828.
23. Bajθnoff M, Egen JG, Koo LY, Laugier J, Brau F, Glaichenhaus N, Germain RN: **Stromal Cell Networks Regulate Lymphocyte Entry, Migration, and Territoriality in Lymph Nodes.** *Immunity* 2006, **25**:989-1001.
24. Lees JR, Sim J, Russell JH: **Encephalitogenic T-cells increase numbers of CNS T-cells regardless of antigen specificity by both increasing T-cell entry and preventing egress.** *Journal of Neuroimmunology* 2010, **220**:10-16.
25. McMahon EJ, Bailey SL, Castenada CV, Waldner H, Miller SD: **Epitope spreading initiates in the CNS in two mouse models of multiple sclerosis.** *Nat Med* 2005, **11**:335-339.
26. Oksaranta O, Tarvonen S, Ilonen J, Poikonen K, Reunanen M, Panelius M, Salonen R: **Influx of nonactivated T lymphocytes into the cerebrospinal fluid during relapse of multiple sclerosis.** *Ann Neurol* 1995, **38**:465-468.
27. Friedl P, Weigelin B: **Interstitial leukocyte migration and immune function.** *Nat Immunol* 2008, **9**:960-969.
28. Yang BG, Tanaka T, Jang MH, Bai Z, Hayasaka H, Miyasaka M: **Binding of lymphoid chemokines to collagen IV that accumulates in the basal lamina of high endothelial venules: its implications in lymphocyte trafficking.** *J Immunol* 2007, **179**:4376-4382.
29. Wilson EH, Harris TH, Mrass P, John B, Tait ED, Wu GF, Pepper M, Wherry EJ, Dzierzinski F, Roos D, Haydon PG, Laufer TM, Weninger W, Hunter CA: **Behavior of parasite-specific effector CD8+ T cells in the brain and visualization of a kinesis-associated system of reticular fibers.** *Immunity* 2009, **30**:300-311.
30. Campagnola PJ, Loew LM: **Second-harmonic imaging microscopy for visualizing biomolecular arrays in cells, tissues and organisms.** *Nat Biotechnol* 2003, **21**:1356-1360.
31. Biber K, Sauter A, Brouwer N, Copray SC, Boddeke HW: **Ischemia-induced neuronal expression of the microglia attracting chemokine secondary lymphoid-tissue chemokine (SLC).** *Glia* 2001, **34**:121-133.
32. Woolf E, Grigorova I, Sagiv A, Grabovsky V, Feigelson SW, Shulman Z, Hartmann T, Sixt M, Cyster JG, Alon R: **Lymph node chemokines promote sustained T lymphocyte motility without triggering stable integrin adhesiveness in the absence of shear forces.** *Nat Immunol* 2007, **8**:1076-1085.
33. Lewis M, Tarlton JF, Cose S: **Memory versus naive T-cell migration.** *Immunol Cell Biol* 2008, **86**:226-231.
34. Opdenakker G, Nelissen I, Van DJ: **Functional roles and therapeutic targeting of gelatinase B and chemokines in multiple sclerosis.** *Lancet Neurol* 2003, **2**:747-756.

35. Yong VW, Krekoski CA, Forsyth PA, Bell R, Edwards DR: **Matrix metalloproteinases and diseases of the CNS.** *Trends Neurosci* 1998, **21**:75-80.
36. Bradley LM, Watson SR, Swain SL: **Entry of naive CD4 T cells into peripheral lymph nodes requires L-selectin.** *J Exp Med* 1994, **180**:2401-2406.
37. Mora JR, von Andrian UH: **T-cell homing specificity and plasticity: new concepts and future challenges.** *Trends Immunol* 2006, **27**:235-243.
38. Butcher EC, Picker LJ: **Lymphocyte homing and homeostasis.** *Science* 1996, **272**:60-66.

doi:10.1186/1742-2094-8-131
Cite this article as: Herz *et al.*: *In vivo* imaging of lymphocytes in the CNS reveals different behaviour of naïve T cells in health and autoimmunity. *Journal of Neuroinflammation* 2011 **8**:131.

Submit your next manuscript to BioMed Central and take full advantage of:

- Convenient online submission
- Thorough peer review
- No space constraints or color figure charges
- Immediate publication on acceptance
- Inclusion in PubMed, CAS, Scopus and Google Scholar
- Research which is freely available for redistribution

Submit your manuscript at
www.biomedcentral.com/submit

BioMed Central

OPEN ACCESS Freely available online

PLOS ONE

Parallelized TCSPC for Dynamic Intravital Fluorescence Lifetime Imaging: Quantifying Neuronal Dysfunction in Neuroinflammation

Jan Leo Rinnenthal[1,4☯], Christian Börnchen[3☯], Helena Radbruch[2,4], Volker Andresen[5], Agata Mossakowski[1,4], Volker Siffrin[2,7], Thomas Seelemann[6], Heinrich Spiecker[5], Ingrid Moll[3], Josephine Herz[2,4¤], Anja E. Hauser[1,4], Frauke Zipp[2,7], Martin J. Behne[3¶], Raluca Niesner[1,2,4*¶]

1 German Rheumatism Research Center, Berlin, Germany, **2** Max-Delbrück Center for Molecular Medicine, Berlin, Germany, **3** Department of Dermatology and Venerology, University Medical Center Hamburg-Eppendorf, Hamburg, Germany, **4** Charité – University of Medicine, Berlin, Germany, **5** LaVision Biotec GmbH, Bielefeld, Germany, **6** LaVision, Göttingen, Germany, **7** Neurology Department, Johannes Gutenberg University Mainz, Mainz, Germany

Abstract

Two-photon laser-scanning microscopy has revolutionized our view on vital processes by revealing motility and interaction patterns of various cell subsets in hardly accessible organs (e.g. brain) in living animals. However, current technology is still insufficient to elucidate the mechanisms of organ dysfunction as a prerequisite for developing new therapeutic strategies, since it renders only sparse information about the molecular basis of cellular response within tissues in health and disease. In the context of imaging, Förster resonant energy transfer (FRET) is one of the most adequate tools to probe molecular mechanisms of cell function. As a calibration-free technique, fluorescence lifetime imaging (FLIM) is superior for quantifying FRET *in vivo*. Currently, its main limitation is the acquisition speed in the context of deep-tissue 3D and 4D imaging. Here we present a parallelized time-correlated single-photon counting point detector (p-TCSPC) (i) for dynamic single-beam scanning FLIM of large 3D areas on the range of hundreds of milliseconds relevant in the context of immune-induced pathologies as well as (ii) for ultrafast 2D FLIM in the range of tens of milliseconds, a scale relevant for cell physiology. We demonstrate its power in dynamic deep-tissue intravital imaging, as compared to multi-beam scanning time-gated FLIM suitable for fast data acquisition and compared to highly sensitive single-channel TCSPC adequate to detect low fluorescence signals. Using p-TCSPC, 256×256 pixel FLIM maps (300×300 μm^2) are acquired within 468 ms while 131×131 pixel FLIM maps (75×75 μm^2) can be acquired every 82 ms in 115 μm depth in the spinal cord of *CerTN L15* mice. The *CerTN L15* mice express a FRET-based Ca-biosensor in certain neuronal subsets. Our new technology allows us to perform time-lapse 3D intravital FLIM (4D FLIM) in the brain stem of *CerTN L15* mice affected by experimental autoimmune encephalomyelitis and, thereby, to truly quantify neuronal dysfunction in neuroinflammation.

Citation: Rinnenthal JL, Börnchen C, Radbruch H, Andresen V, Mossakowski A, et al. (2013) Parallelized TCSPC for Dynamic Intravital Fluorescence Lifetime Imaging: Quantifying Neuronal Dysfunction in Neuroinflammation. PLoS ONE 8(4): e60100. doi:10.1371/journal.pone.0060100

Editor: Stephen D. Ginsberg, Nathan Kline Institute and New York University School of Medicine, United States of America

Received August 8, 2012; **Accepted** February 22, 2013; **Published** April 16, 2013

Copyright: © 2013 Rinnenthal et al. This is an open-access article distributed under the terms of the Creative Commons Attribution License, which permits unrestricted use, distribution, and reproduction in any medium, provided the original author and source are credited.

Funding: The authors acknowledge the Deutsche Forschungsgemeinschaft under grant NI 1167/2-1 to RN and SFB-TRR 43 to FZ, the Berlin-Brandenburg School for Regenerative Therapies GSC 203 for HR and the Charité – University Hospital, Berlin under grant Rahel-Hirsch fellowship for RN for financial support. This work was partially funded through a Marie-Curie grant (MC-IRG 6675 to MB). The funders had no role in study design, data collection and analysis, decision to publish, or preparation of the manuscript.

Competing Interests: VA and HS are with LaVision BioTec, Bielefeld, Germany and TS is with LaVision, Göttingen, Germany. There are no patents, products in development or marketed products to declare. This does not alter the authors' adherence to all the PLOS ONE policies on sharing data and materials.

* E-mail: niesner@drfz.de

☯ These authors contributed equally to this work.

¶ These authors also contributed equally to this work.

¤ Current address: Neurology Department, University Duisburg-Essen, Essen, Germany

Introduction

The two-photon laser-scanning microscopy (TPLSM) [1] has dramatically changed our perspective on cellular dynamics of both physiologic and pathologic processes especially in the central nervous system and in organs of the immune system [2–5], thus, giving the opportunity to develop new diagnostic and therapeutic tools. This is due to the advantages of near-infrared short-pulsed excitation [6–7], which enables non-invasive tracking of cellular motility and communication deep within living organisms, i.e. in intravital imaging. However, the molecular basis of cellular function, the key to organ function, remains difficult to access in dynamic highly-resolved intravital studies.

The most common phenomenon used to monitor cellular function on a molecular basis in optical imaging is Förster Resonant Energy Transfer (FRET), which has been extensively employed *in vitro* to probe protein-protein interactions and examine cellular phenomena [8–12]. The development of mouse models encoding FRET biosensors based on fluorescent proteins [13] has opened new opportunities for the long-term monitoring of cell and tissue function in living organisms [14–17].

Numerous technological advances are required to fully take advantage of the FRET potential for intravital quantification of cell function. In addition to the improvement of microscope optical performance and the development of small animal surgical techniques with the general aim of non-invasive imaging, calibration-free signal quantification and fast 3D-image acquisition are needed, especially to allow observation of pathologic changes of tissue in response to interactions with highly motile cells (e.g. those moving at a rate of 5–7 μm/min) [2–4]. As far as physiological modifications are concerned, even higher acquisition rates are required, for instance, calcium oscillations take place on the time scale of a few milliseconds.

Established quantitative FRET techniques include [8–9]:

i. different ratiometric techniques [18],
ii. photobleaching-based techniques [10,19]
iii. fluorescence lifetime imaging (FLIM) [11,20–21] and
iv. time-resolved fluorescence anisotropy imaging (trFAIM) [11].

Photobleaching-based techniques are very reliable, but rather slow and potentially invasive. Although calibration-free, trFAIM leads to slight read-out modifications at low signal strength, which are incompatible with the requirements of deep-tissue imaging. While ratiometric FRET techniques have already been applied intravitally [3,14,18], in order to fulfill the requirements for dynamic, calibration-free intravital FRET quantification, fast and accurate FLIM with high spatial resolution, deep within the tissue is needed. Although faster than FLIM, ratiometric techniques are prone to artifacts due to light scattering caused by strong refractive index mismatches in tissue. Scattering is dependent on the wavelength (emission/excitation) [22], thus, inducing a different degree of deterioration regarding resolution and signal-to-noise ratio (SNR) for different emitted wavelengths at increasing imaging depth. Concretely, the shorter wavelength emission of the donor and the longer wavelength emission of the acceptor of the FRET-pair are characterized by different depth-dependent signals and SNR which induce an artificial depth-dependent gradient of the FRET-ratio.

Because of the multi-exponential nature of the fluorescence signal typically acquired in tissue, the use of time-domain FLIM techniques is recommended [23]. Multifocal scanning combined with field-detection [24], especially of gated optical intensifiers (GOI), ensures fast, video-rate FLIM [25]. Deficits of this approach include intrinsically poor photon economy (~10% signal exploitation), relatively poor resolution and limited imaging depth in tissue. The alternative use of streak cameras, which allow direct fluorescence decay acquisition, and thus presumably better photon economy, is limited by the slow speed of photon counting electronics, typically 1 MHz [26].

The most accurate techniques which allow for diffraction-limited FLIM [12] are based on time-correlated single-photon counting (TCSPC). Intravital FRET-FLIM microscopy and microendoscopy [12,17] have already been applied in cancer research. However, the principal deficit of standard TCSPC remains the poor photon economy, due to slow photon counting electronics. Count rates are typically 8 MHz for time-to-amplitude-converters (TAC) [27–28] or 11 MHz for time-to-digital-converters (TDC) [29], whereas the repetition rate of TPLSM lasers is typically 80 MHz. This leads to slow image acquisition, up to 90% signal loss and potentially to photobleaching and tissue photodamage. In contrast, multifocal TPLSM combined with TCSPC based on 16 channel multi-anode photomultiplier tubes (PMT) is able to increase the acquisition speed in 3D-FLIM, and has been applied to probe NAD(P)H metabolism in a cancer cell line [27]. However, this approach is still limited by slow electronics, with an average count rate of 3.2 MHz, and by considerable photobleaching (18% between successive 3D images) [27]. Scalable multichannel TCSPC systems based on TDC, which increase the average count rate, have been employed in fluorescence correlation spectroscopy (FCS) rather than FLIM [29]. Using a parallelized TCSPC technique with different detectors and electronics compared to our technology, a FLIM acquisition speed of 100 ms/ 100×100 pixel (10 μs/pixel) has been reported at the surface of brain slices [30]. Multi-parametric, fast wide-field FLIM has been used to quantify protein-protein interactions in living cells [31]. As far as the sensitivity is concerned, hybrid detectors used in new FLIM systems are a very promising solution for fast highly sensitive FLIM.

Still, fast dynamic 3D-FLIM (4D-FLIM) deep within hardly accessible organs of living animals as required by typical biological questions has not been yet demonstrated.

As far as the analysis of the largely unknown multi-exponential fluorescence decays in tissue is concerned, reliable and fast algorithms have been adapted for FLIM, e.g. Phasor-approach [32], stretched-exponential [33], Laguerre expansion [34] or genetic algorithms [20] in addition to the standard Levenberg-Marquardt iterative approach.

Here we present a highly efficient 16-channel parallelized TCSPC (p-TCSPC) technique with an average count rate of 80 MHz, which allows fast fluorescence lifetime map acquisition limited only by the frequency of the galvoscanner, i.e. 512×512 pixel lifetime images are acquired within 427 ms (1.63 μs/pixel). Since the main requirement in live tissue and intravital FLIM with relevance for cell biology or the investigation of (immune-induced) pathologies is fast acquisition in the range of tens or hundreds of milliseconds, we compare the performance of our new device to multifocal GOI, i.e. the standard technique for ultra-fast video-rate FLIM, and to highly sensitive single-channel TCSPC using hybrid detectors both on standardized dye solutions and in live samples (hippocampus slices and brain stem of live mice). Thereby, special focus is dedicated to the relevance of parallelization of detection and counting electronics in order to increse acquisition speed in dynamic intravital FLIM.

By employing p-TCSPC, we are for the first time able to dynamically quantify neuronal function via calcium levels in the chronically inflamed brain stem of *CerTN L15* mice [14]. We chose experimental autoimmune encephalomyelitis, a murine model of Multiple Sclerosis, to induce chronic inflammation to the central nervous system (CNS). We thus demonstrate the practical value of this technique as a tool to truly quantify the cellular mechanisms of early neural injury occurring in CNS inflammation.

Materials and Methods

Two-photon laser-scanning microscopy (TPLSM)

FLIM experiments were performed using a specialized two-photon laser-scanning microscope (Fig. S1a) based on a commercial scan head (TriMScope, LaVision BioTec, Bielefeld, Germany) [35–36]. The novel 16-channel TCSPC detector (FLIM-X_{16}, LaVision BioTec, Bielefeld, Germany) and the hybrid-detector single-channel TCSPC (HPM-100-40 combined with a 10 MHz SPC-150, Becker&Hickl, Berlin, Germany) were used in combination with single-beam laser-scanning whereas the time-gated FLIM field-detector (PicoStar, LaVision, Göttingen, Germany) was used with multi-beam (up to 64 beams) scanning. For detailed setup descriptions see *Material S1*.

Table 1. Mono- and bi-exponential FLIM benchmarking experiments on standardized dyes.

dye conc.	vol. fraction	GOI					pTCSPC					single channel TCSPC				
		100×100 pixel, 33×33 μm²					100×100 pixel, 29×29 μm²					100×100 pixel, 29×29 μm²				
		ph./pixel	τ_1 /ps	τ_2 /ps	a_1/a_1+a_2/%	χ^2_R	ph./pixel	τ_1 /ps	τ_2 /ps	a_1/a_1+a_2/%	χ^2_R	ph./pixel	τ_1 /ps	τ_2 /ps	a_1/a_1+a_2/%	χ^2_R
Rh6G	-	920	-	4003	-	1.26	860	-	4028	-	1.02	890	-	4049	-	1.09
				(83)					(79)					(136)		
RhB	-	850	1691	-	-	1.35	730	1724	-	-	0.94	966	1740	-	-	1.15
			(77)					(53)					(48)			
acq time		4.95 s					8.6 s					15 s				
ph. flux		$4.57 \cdot 10^{29}$ photons/s·cm²					$4.14 \cdot 10^{29}$ photons/s·cm²					$8.28 \cdot 10^{28}$ photons/s·cm²				
count rate		$9.8 \cdot 10^5$ photons/s					$8{,}8 \cdot 10^5$ photons/s					$4.6 \cdot 10^5$ photons/s				
RhB:Rh6G	4:1	1080	1750	4150	83.3	1.36	1100	1712	4182	81.2	0.99	-	-	-	-	-
			(268)	(281)	(3.5)			(98)	(199)	(2.8)						
RhB:Rh6G	1:1	1360	1811	4158	53.3	1.28	1260	1773	4097	52.3	1.02	1250	1738	3972	53.7	1.22
			(283)	(226)	(5.2)			(123)	(160)	(3.1)			(192)	(224)	(4.8)	
aqc time		9.9 s					10.6 s					15 s				
ph. flux		$4.57 \cdot 10^{29}$ photons/s·cm²					$4.14 \cdot 10^{29}$ photons/s·cm²					$8.28 \cdot 10^{28}$ photons/s·cm²				
count rate		$1.2 \cdot 10^6$ photons/s					$1.05 \cdot 10^6$ photons/s					$5.7 \cdot 10^5$ photons/s				

The values in brackets represent FWHM (full width at half maximum) of the corresponding distribution of the parameters τ_1, τ_2, $a_1/(a_1+a_2)$, respectively, in the (mono- or bi-) exponential approximations. The experimental parameters, i.e. frame dimension, photon flux, acquisition time and count rate, are given for each FLIM detector. λ_{exc} = 800 nm, $\lambda_{emission}$ = 593±20 nm.

doi:10.1371/journal.pone.0060100.t001

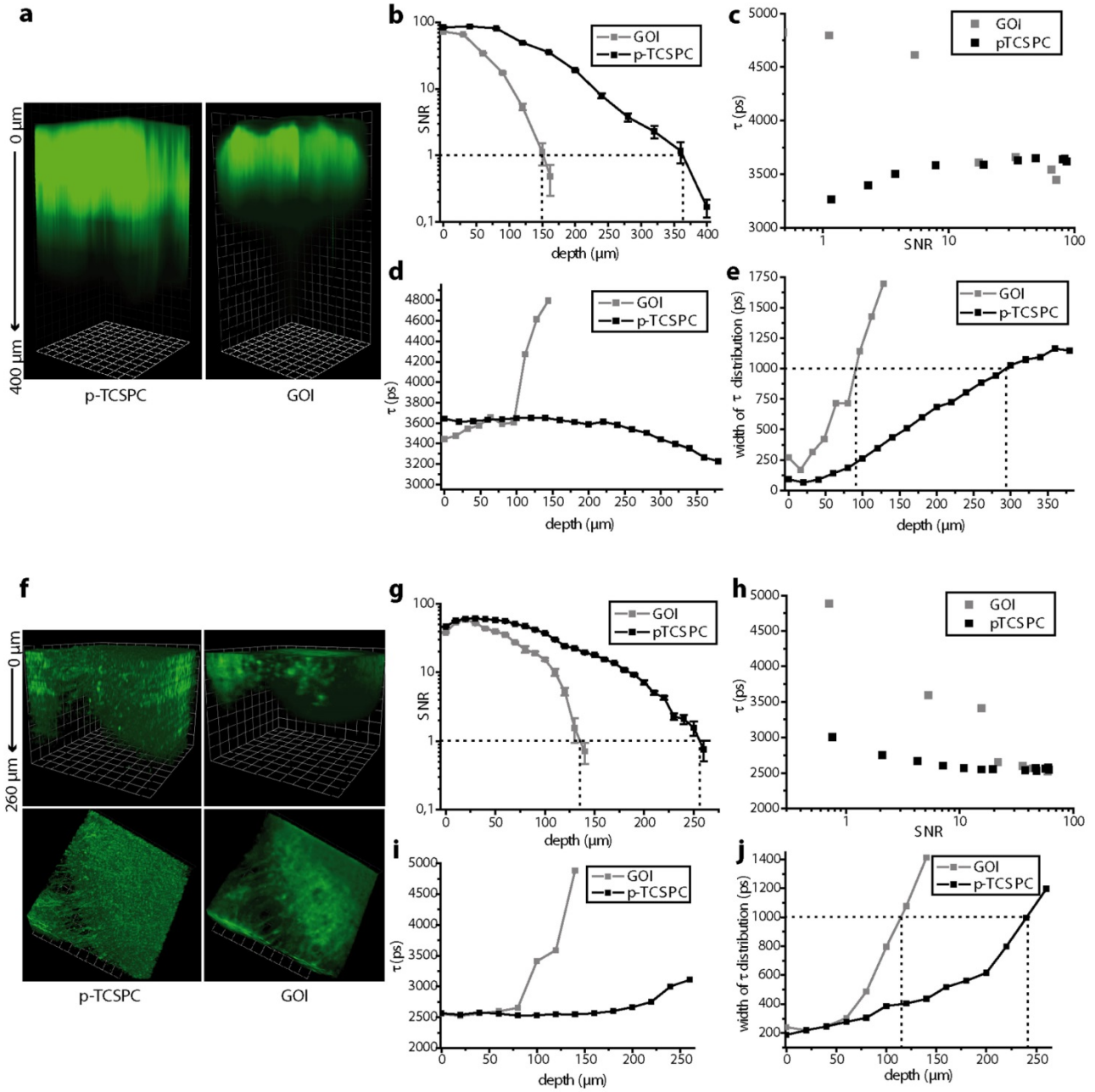

Figure 1. Depth-dependent SNR and maximum imaging depth in FLIM. Three dimensional fluorescence images acquired by means of the GOI and p-TCSPC setup, respectively, at the same region **(a)** of a fluorescein-isothio-cyanate (FITC) stained skin biopsy (200×200×400 μm^3) and **(f)** of a hippocampal slice of a *Thy1 EGFP* mouse, in which neuronal subsets express EGFP, (300×300×260 μm^3). Corresponding depth dependent signal-to-noise ratio (ddSNR) curves are shown in **(b)** for the skin biopsy and in **(g)** for the hippocampal slice**.** Dependence of the mean fluorescence lifetime on ddSNR is depicted in **(c)** for the dermal samples and in **(h)** for the hippocampal slices. Depth dependence of the mean fluorescence lifetime of FITC in the skin biopsy is depicted in **(d)** and of EGFP in the hippocampal slice is shown in **(i)**. The corresponding widths (Gaussian full-width-at-half-maximum) of the lifetime distributions are shown in **(e)** and **(j)**, respectively. Setup parameters are listed in *Material S1*.
doi:10.1371/journal.pone.0060100.g001

2.43-fold (Fig. 1a, b). The FLIM depth at the same area amounted to 90 µm with the GOI setup as compared to 290 µm with the p-TCSPC setup (Fig. 1d, e). Interestingly, considerable deviation from the expected mean fluorescence lifetime of FITC occurs already at a ddSNR larger than 10 for the GOI setup as compared to a ddSNR value of 4 for the p-TCSPC setup (Fig. 1c). We explain this observation by the allocation of emitted photons in false pixels on the GOI due to scattering effects, which on its turn leads to an apparent time-spread of the photon arrival. In hippocampal slices of *Thy1 EGFP* mice the ddSNR imaging depth under similar excitation conditions (*Material S1*) and at the very same area amounted to 133 µm with the GOI setup and 258 µm with the p-TCSPC setup, an increase of 1.94-fold (Fig. 1e, f) whereas the FLIM depths were 115 µm and 240 µm (Fig. 1g, h),

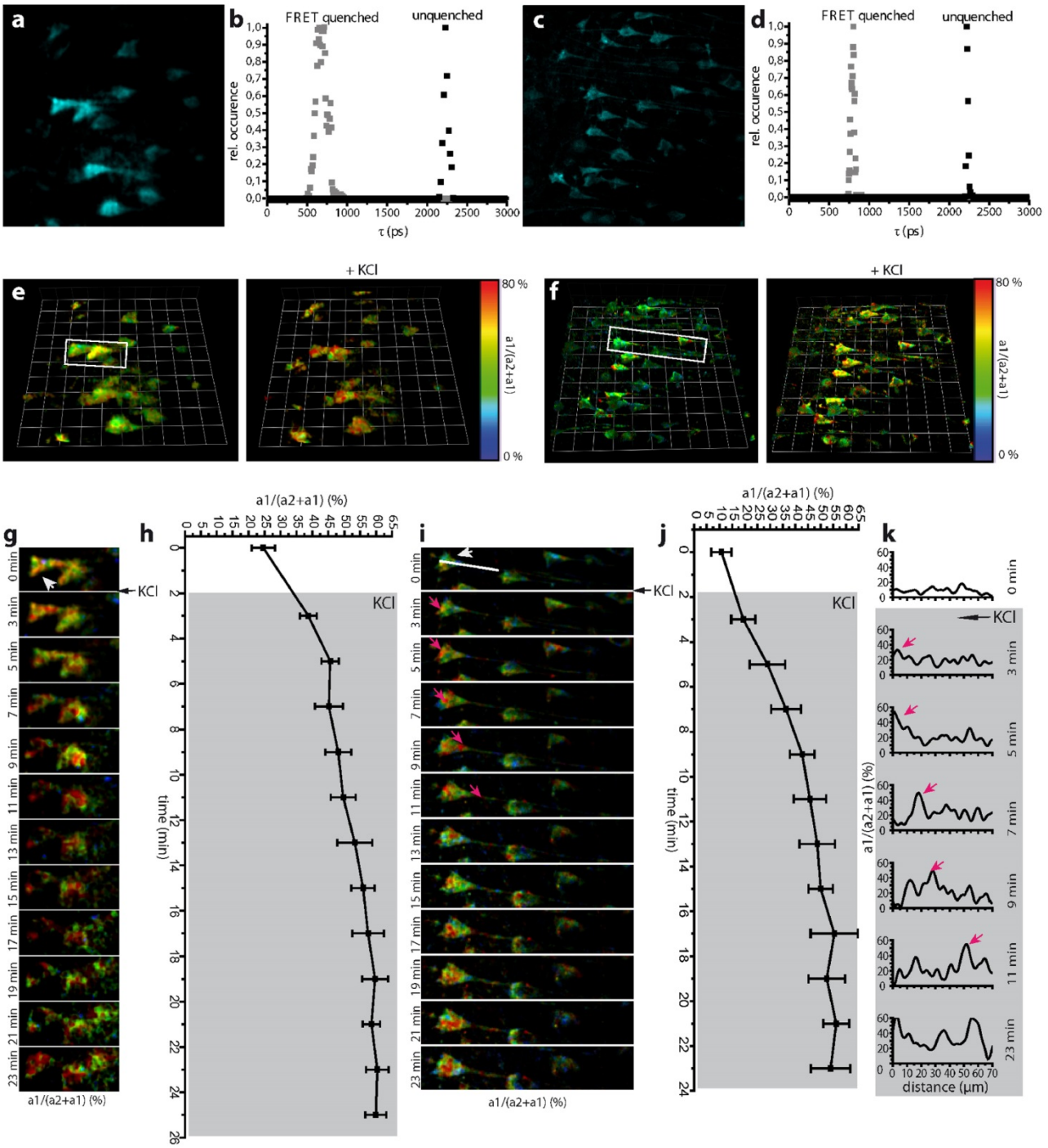

Figure 2. Dynamic FRET-FLIM in living hippocampal slices of *CerTN L15* mice. Projections of three dimensional (3D) fluorescence data sets **(a)** (221×221×12 µm^3, 492×492×5 voxel) acquired by the GOI setup and **(c)** (200×200×12 µm^3, 512×512×5 voxel) acquired by the p-TCSPC setup in a living hippocampal slice of a *CerTN L15* mouse. The fluorescence lifetime distributions of the FRET-quenched and unquenched Cerulean corresponding to **(a)** and **(c)** are depicted in the graphs **(d)** and **(b)**. **(e)** and **(f)** show corresponding 3D $a_1 \cdot 100/(a_2+a_1)$ images (FRET-ratio images) before and 7 minutes after perfusion with a 100 mM KCl solution as acquired with the GOI and p-TCSPC setup, respectively. The depolarization of the neurons in the presence of highly concentrated K^+ ions leads to an increase of neuronal calcium level, as shown by increased FRET signal. **(g)** Time-lapse images showing neurons in the demarcated area in **(e)** depicting the increase of calcium in neuronal somata. The graph **(h)** shows the increase of calcium level in the soma indicated in **(g)** by the arrowhead. 3D unit = 28 µm, scale bar = 20 µm. **(i)** Time-lapse showing neurons in the demarcated area in **(f)** depicting the increase of calcium in neuronal somata and processes. The magenta arrows in **(i)** indicate the incomplete depolarization immediately after application, i.e. high calcium levels are still led from the dendrites through the soma to the axon before the neuron is completely flooded by calcium. The graphs in **(k)** show the neuronal calcium level at the indicated time points along the white line in **(i),** reaching from the soma to the axon. The magenta arrows in (**k**) correspond to the Calcium increase also indicated by magenta arrows in the image series (**i**). The same process of neuronal depolarization as in **(h)** for the GOI setup can be observed in **(j)** for the p-TCSPC setup. 3D unit = 30 µm, scale bar = 20 µm. Imaging was performed starting from 15–30 µm depth in tissue, which is beyond the glial scar.
doi:10.1371/journal.pone.0060100.g002

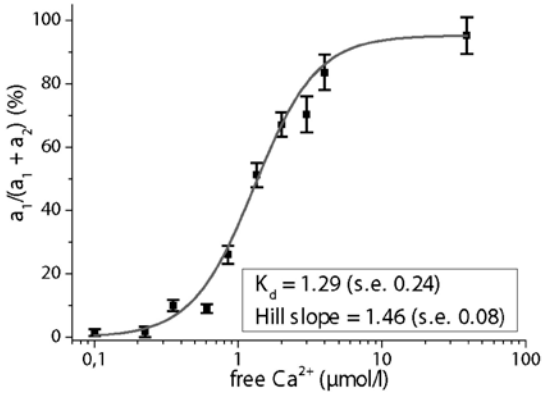

Figure 3. FLIM-based Calcium calibration of TN L15. The FRET signal of TN L15 (Troponin C bound to the FRET pair Cerulean and Citrine) was measured by FLIM in buffered solutions of different free Calcium concentrations in the range 0 µM to 39 µM (Ca Calibration Buffer Kit, Invitrogen, Germany). The fluorescence decays were biexponentially approximated. In all cases, the fluorescence lifetime of the FRET-quenched Cerulean amounts to 808 ps and that of the unquenched Cerulean to 2491 ps. These values well agree according to the Strickler-Berg dependence on refractive index to the values measured in brain slices and in the brain stem of live mice. The ratio a1/(a1+a2) of FRET-quenched to unquenched Cerulean represents the FRET signal and is depicted on the ordinate. The inset shows the values for K_d and the Hill slope.
doi:10.1371/journal.pone.0060100.g003

respectively. The dependence of the mean fluorescence lifetime on ddSNR depicted in Fig. 1 h emphasizes that also in brain slices strong deviations from the expected fluorescence lifetime occur for the GOI setup already at ddSNR of 17 whereas for the p-TCSPC setup the critical ddSNR is much lower (between 3 and 4).

The imaging depths, i.e. ddSNR depth and FLIM depth, attained by means of single-channel TCSPC were similar to those reached if using the p-TCSPC setup. Thereby, the excitation power/excitation photon flux was reduced up to 5 times in the single-channel TCSPC setup as compared to the p-TCSPC setup to avoid pile-up (max. 10^6 photons/s).

In favor of avoiding artifacts caused by a more complicated results interpretation we omitted the widely used exponential increase of mean excitation power to increase imaging depth in tissue [6].

Calcium imaging by 4D-FRET-FLIM in *CerTN L15* mice: performance of p-TCSPC vs. GOI in hippocampus slices

Quantitatively monitoring cellular function by FRET directly in living tissue is pivotal to fully understand basic physiologic and pathologic mechanisms. Therefore, time-lapse 2D and 3D FRET-FLIM, ensuring low photobleaching and photodamage, high acquisition speed and sub-cellular resolution deep within tissue, is required.

We compared the single-beam p-TCSCP to the multifocal GOI setups by probing neuronal function in acute hippocampal slices of adult *CerTN L15* mice during membrane depolarization induced by increased K^+ ion concentration (maximal FRET efficiency 65%). Brain slices prepared in this manner have been shown to retain a layer of living tissue in the middle of the slice, which is comparable to the native central nervous system (CNS) environment [44]. Imaging was performed in this living layer of acute slices, beyond the glial scar, starting at a depth of 30 µm.

The fluorescence lifetimes of unquenched and quenched Cerulean amount to 2225 ps (22 ps FWHM) and 693 ps (45 ps FWHM) with the p-TCSPC detector (Fig. 2b) and to 2234 ps (61 ps FWHM) and 677 ps (139 ps FWHM) with the GOI detector (Fig. 2d). This corresponds to previously determined values within the error margins [45]. The fluorescence lifetimes of both unquenched and FRET-quenched Cerulean in *TN L15* measured here in brain tissue are somewhat shorter than those measured under extracellular conditions by us ($\tau_{unquenched}$ = 2491 ps (158 ps FWHM), $\tau_{FRET\text{-}quenched}$ = 808 ps (49 ps FWHM)) and by others [46]. We attribute this to differences in refractive index *n*, i.e. the fluorescence lifetime τ scales with $1/n^2$ [47]. The lifetime values did not change over the whole acquisition period (40 time points), therefore excluding the possibility of eventual photo-isomerization of Cerulean, as has been reported for different conditions [48]. No significant change in mean fluorescence lifetime was observed down to 100 µm imaging depth in brain tissue.

A 3D image restoring the ratio $a_1 \cdot 100/(a_2 + a_1)$ gives the relative concentration of FRET quenched to total Cerulean concentration. The FRET signal shows a sigmoid dependence on calcium concentration (apparent K_d = 1.29±0.24 µM, Hill slope = 1.46±0.08, (Fig. 3) These values confirm previous calibration of the TN L15 construct (K_d = 1.2, Hill slope = 1.47) performed by ratiometric FRET [49].

The time-step for a similar time-resolved 3D data set of Cerulean, i.e. 492×492×5 voxel with the GOI setup (Fig. 2a) and 512×512×5 voxel with the p-TCSPC setup (Fig. 2c), respectively, was set to 120 s. The time-step does not correspond to the true acquisition time required to collect enough photons for the bilinear FRET-FLIM evaluation. We limited the acquisition rate to minimize photobleaching and photodamage if using the GOI setup and, thus, to enable time-lapse FLIM with the multifocal GOI setup. A reduction of the excitation power in the GOI setup led to fluorescence signals that are too low to be further evaluated. The peak photon flux was similar for both detectors (*Material S1*) and was adjusted in a way that at least 1000 photons/pixel are acquired. The true acquisition time for a 492×492×5 voxel image was 41.9 s with the GOI setup and for a 512×512×5 voxel image was 25 s with the p-TCSPC setup (19 µs/voxel)

The FRET signal in neurons within the middle layer typically amounts to 9±3% (N = 11 cells, s.d.), i.e. 240±27 nM calcium, with the p-TCSPC and to 17±6% (N = 7 cells, s.d.), i.e. 417±53 nM calcium, with the GOI. The damaged superficial neurons in the glial scar can locally reach values of up to 52%, i.e. 1.39 µM calcium, as depicted in measurements performed with the p-TCSPC (Fig. 2f).

We monitored the calcium distribution in neurons before and during perfusion with 100 mM KCl solution (Fig. 2e, f, *movies S1* and *S2*). Using both the GOI and the p-TCSPC setup, we observed an increase of mean calcium concentration in neurons due to membrane depolarization (Fig. 2g, i). However, the sub-cellular distribution of pathologically caused calcium waves over time could only be visualized using the p-TCSPC setup (Fig. 2i). Here it became evident that during membrane depolarization via increased K^+ a slow propagation of a high amplitude calcium wave (single peaks between 35% and 62% FRET ratio) from the dendrites through the soma to the axon, similar to the fast calcium oscillation under physiological conditions, overlapped a slight overall increase of the calcium level (9±3% before as compared to 18±4% immediately after KCl addition). After approx. 20 minutes the neurons were completely flooded by calcium (65% FRET-quenched Cerulean, i.e. 1.97 µM Ca^{2+}). This calcium level increase in neurons correlates with changes in neuron morphology: over time, both the somata and the cell nuclei showed signs of swelling before the cell membrane disintegrated.

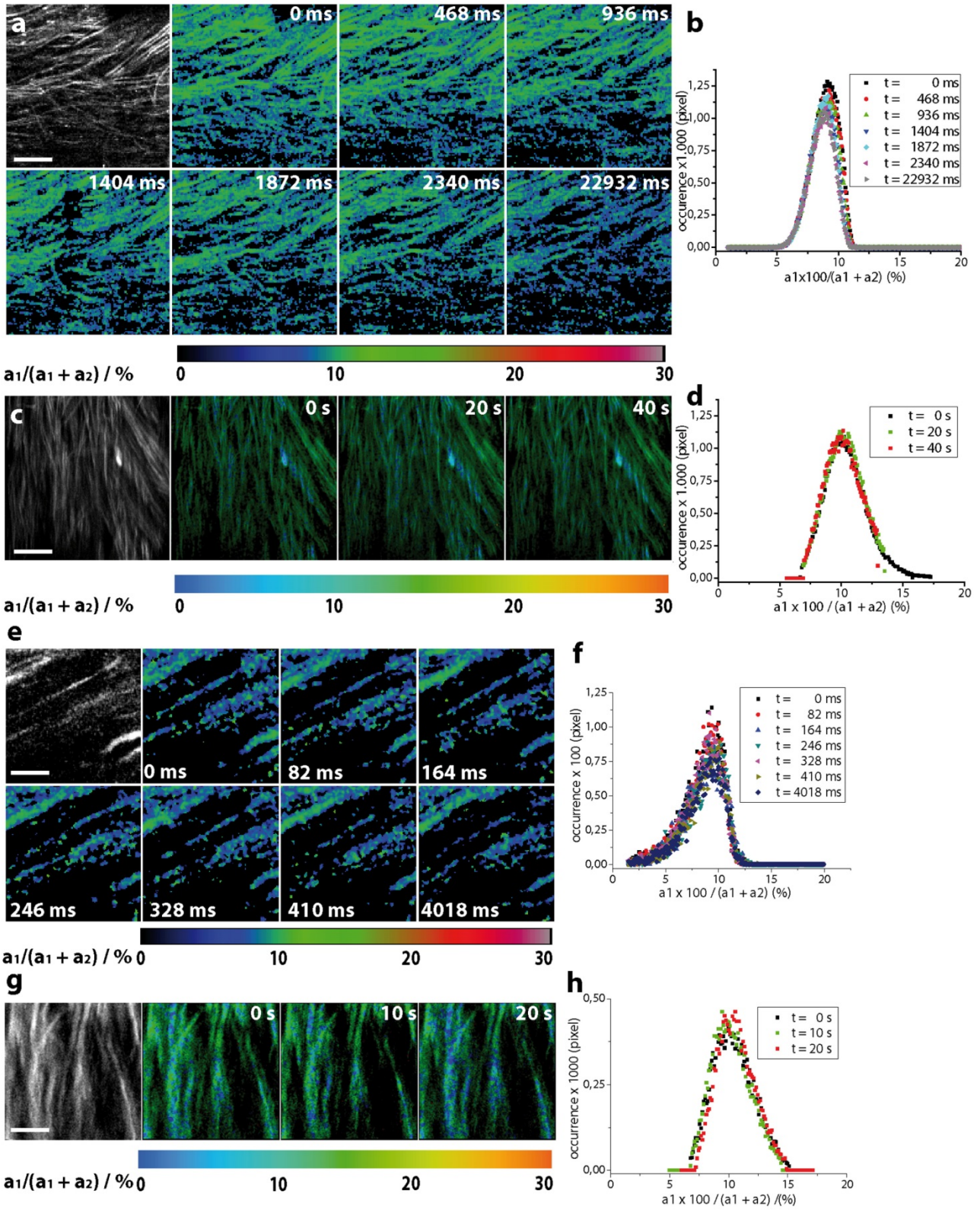

Figure 4. Dynamic intravital FRET-FLIM in the spinal cord of healthy *CerTN L15* mice. (a) Intensity of Cerulean and FRET-ratio ($a_1 \cdot 100/(a_1 + a_2)$ ratio) maps of axons in the spinal cord of a CerTN L15 mouse. 300×300 μm^2 (256×256 pixel) FRET-FLIM images are acquired every 468 ms using the p-TCSPC device. **(b)** The accuracy of the FRET-ratio in these data is quantified by the width of its distribution over an image (e.g. 9.04±1.11% corresponding to 242±76 nM calcium, t = 0 ms). This value corresponds to the expected calcium concentration in healthy neurons (44). The distributions of the FRET-ratio do not change over time (after 50 illumination steps). **(c)** Intensity of Cerulean and FRET-ratio maps (300×300 μm^2,

256×256 pixel) of axons in the spinal cord of a CerTN L15 mouse must be acquired every 20 s using the high-performance single-channel TCSPC to avoid pile up effects (maximally 10^6 photons/s) which artificially reduce the fluorescence lifetime of Cerulean and increase the FRET-ratio, i.e. the apparent calcium concentration. Thus, a much lower excitation power (1.8 mW instead of 18 mW as used in the p-TCSPC setup at 850 nm excitation wavelength) was applied. The full potential of the hybrid detector could not be exploited due to the limited average counting rate of the electronics. **(d)** The distributions of the FRET-ratio corresponding to the images in (c) are similar to the distributions measured using the p-TCSPC setup. Thus, the accuracy of the FRET-ratio measured by p-TCSPC (a) and single-channel TCSPC (c) is also similar. **(e)** 75×75 μm^2 (131×131 pixel) FRET-ratio maps in the spinal cord of the same mouse line could be acquired every 82 ms using the p-TCSPC device. **(f)** The accuracy of the images in (e) is restored by the distribution of the FRET-ratio (9.09±1.58% corresponding to 244±10.6 nM calcium, t = 0 ms), which remains stable over time (50 illumination steps). **(g)** FRET-ratio maps of the same dimensions (75×75 μm^2, 131×131 pixel) must be acquired every 10 s in order to simultaneously avoid pile-up effects and to achieve the same accuracy as by p-TCSPC-FLIM. **(h)** Distributions of FRET-ration in the images in (g).
doi:10.1371/journal.pone.0060100.g004

As far as intravital FLIM is concerned, the multifocal GOI setup was not able to repeatedly recover enough fluorescence signal due to the need for an extremely high excitation power, which led to photobleaching after very few illumination steps.

Fast and ultra-fast intravital calcium imaging by 3D-FRET-FLIM in *CerTN L15* mice: performance of p-TCSPC vs. single-channel TCSPC in the spinal cord

We compared the novel p-TCSCP (80 MHz average counting rate) with a hybrid-detector based single-channel TCSPC setup (10 MHz average counting rate) by probing neuronal function in the spinal cord of healthy *CerTN L15* mice. Imaging was performed in approx. 115–130 µm depth (Fig. 4).

We focused on (2D+time)-FRET-FLIM over large fields of view (300×300 μm^2, 256×256 pixel) with relevance in the investigation of pathologies. Using the p-TCSPC setup we could acquire a FRET-ratio image by FLIM every 468 ms (2000 photons/pixel, 18 mW (peak photon flux $\Phi = 4.36 \cdot 10^{30}$ photons/s·cm^2, $\lambda_{exc} = 850$ nm, count rate $6.38 \cdot 10^7$ photons/s). The accuracy of the images is restored by the parameters of the FRET-ratio distribution (t = 0 ms, 9.04±1.11% corresponding to 242±8.03 nM calcium). Even after 50 illumination steps the accuracy is retained (t = 22932 ms, 8.57±1.00% corresponding to 226±7.6 nM). In order to avoid pile-up effects, which induce an artificial shortening of the fluorescence lifetime and, thus, an increase of the FRET-ratio, i.e. of the apparent calcium concentration we limited the excitation power when using the single-channel TCSPC setup to 1.8 mW (peak photon flux $\Phi = 4.36 \cdot 10^{29}$ photons/s·cm^2, $\lambda_{exc} = 850$ nm, count rate $1.6 \cdot 10^6$ photons/s). Under these conditions, 20 s were necessary to acquire a 300×300 μm^2 (256×256 pixel) FRET-ratio map (2460 photons/pixel). The accuracy of the FRET-ratio is similar to that achieved by the p-TCSPC setup (t = 0 s, 10.04±1.58% corresponding to 271±10.6 nM calcium).

Ultra-fast (2D+time) FRET-FLIM on the time-scale of milliseconds (75×75 μm^2, 131×131 pixel) with relevance for cell physiology and cell biology emphasizes the superiority of electronics and detector parallelization (p-TCSPC) as compared to high-performance single-channel TCSPC (Fig. 4. e-h). Using the p-TCSPC setup we could acquire a FRET-ratio image by FLIM every 82 ms (1700 photons/pixel, 12 mW (peak photon flux $\Phi = 2.9 \cdot 10^{30}$ photons/s·cm^2, $\lambda_{exc} = 850$ nm, count rate $4.2 \cdot 10^7$ photons/s). The accuracy of the images is given at t = 0 ms by the FRET-ratio distribution 9.09±1.58% corresponding to 244±10.6 nM calcium. Even after 50 illumination steps the accuracy is retained (t = 4018 ms, 9.04±1.59% corresponding to 242±10.6 nM). Using the single-channel TCSPC at 0.9 mW excitation power and 850 nm excitation wavelength, 10 s were needed to acquire a FRET-ratio map of 75×75 μm^2 (131×131 pixel). The count rate amounted to $1.05 \cdot 10^6$ photons/s. The accuracy in this case was also similar to that of the p-TCSPC (2100 photons/pixel, t = 0 s, 10.25±1.81% corresponding to 276±11.7 nM calcium). In this context, it has to be mentioned that the use of the FRET-based constructs for such questions is rather inadequate, since the response time of the constructs to the stimulus, in this case calcium, is lower (520 ms) than the frame time of FLIM and the time resolution typically required by questions in cell biology [15,49]. Furthermore, the dynamic range (K_d and Hill slope) of the construct must be considered (Fig. 3) when choosing the genetically encoded calcium construct to answer a specific question.

The fluorescence lifetimes of unquenched and FRET-quenched Cerulean restored by biexponential approximation of the FLIM data acquired with single-channel TCSPC (*Fig. S4*) typically amounted to 2269 ps (FWHM 214 ps) and 754 ps (FWHM 158 ps), respectively ($\chi^2 = 1.00$). Using the p-TCSPC, the fluorescence lifetimes of unquenched and quenched Cerulean amounted to 2316 ps (223 ps FWHM) and 778 ps (115 ps FWHM), respectively ($\chi^2 = 1.09$).

Intravital quantification of neuronal calcium in CNS inflammation by p-TCSPC FLIM

Using the p-TCSPC setup we were able to perform time-lapse 3D FLIM in 30 to 150 µm depth in the brain stem of live anesthetized *CerTN L15* chimeric mice which were reconstituted with a tdRFP expressing immune system. These mice were affected by experimental autoimmune encephalomyelitis (EAE) (Fig. 5). We were therefore able to quantify the absolute sub-cellular calcium concentration in neurons during direct interaction with immune cells. The calcium levels in neurons not in contact with immune cells was low, i.e. $a_1 \cdot 100/(a_2+a_1)$ of 8±3% (227±27 nM calcium, n = 8, 5 mice, 2 different EAE cohorts), while in somata that were in contact with immune cells, the local calcium level increased up to 58% (1.66 µM calcium) (Fig. 5a, b). Our dynamic intravital FRET-FLIM experiments quantitatively validate for the first time our prior qualitative observation that sustained dynamic interaction between immune cells and neuronal structures in EAE (> 5 min) correlates with increased neuronal calcium levels at the contact site, which is followed by partially reversible neuronal dysfunction (> 1 µM calcium) as defined in [3].

Furthermore, the perfusion of the brain stem with 100 mM KCl solution lead to an increase of neuronal calcium in all neurons via membrane depolarization (Fig. 5d, e, f, *movie S3*). In low-calcium somata not in contact with immune cells, the calcium increase was more prominent than in high-calcium somata (Fig. 5e, f). Interestingly, the expected maximum calcium concentration (FRET signal 70%, 3.1 µM calcium) by depolarization is not reached. A possible explanation is the fact that in the living organism with intact blood flow, the locally applied KCl solution can be easily removed.

For these experiments, 3D time-resolved data sets of 150×150×30 μm^3 (256×256×16 voxel) or of 150×150×12 μm^3 (256×256×7 voxel) were acquired every 90 or 60 seconds (*Material S1*). The fluorescence lifetime of unquenched and FRET-quenched Cerulean, respectively, amounted to 2318 ps (217 ps

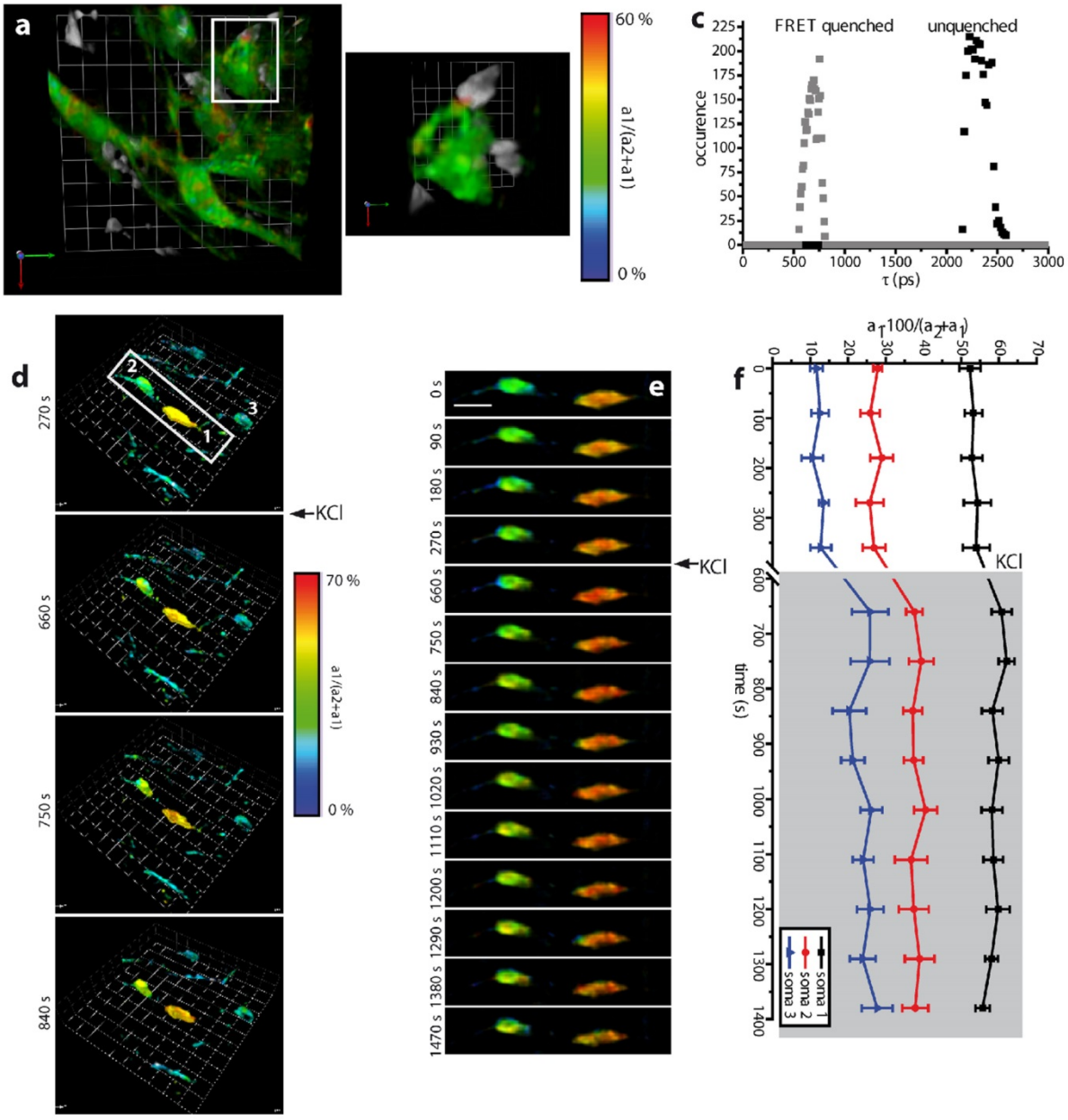

Figure 5. Dynamic intravital FRET-FLIM in the brain stem of *CerTN L15* mice. (a) Merged 3D $a_1 \cdot 100/(a_2+a_1)$ image (FRET signal image, 150×150×30 μm^3, 256×256×16 voxel in 90 μm depth) showing neuronal calcium and 3D data set of the tdRFP expressing immune cells recorded by the p-TCSPC setup. **(b)** As shown in the demarcated area in **(a)**, the calcium level in somata and processes interacting with immune cells, directly at the contact site, is significantly higher (FRET signal of up to 58%, 1.66 μM calcium, orange-red area in **(b)**) than in unaffected somata and processes (FRET signal of approximately 8%, 110 nM calcium). The corresponding fluorescence lifetime distributions of the FRET-quenched and unquenched Cerulean, as shown in the graph **(c)**, are similar to those determined in hippocampal slices. **(d)** The perfusion with a 100 mM KCl solution led to the depolarization of the neurons followed by a calcium concentration increase. The effect is more prominent in cells with low calcium than in the already affected neurons. **(e)** Time lapse of 3D $a_1 \cdot 100/(a_2+a_1)$ images of two neurons in contact with immune cells and then being subject to K^+ ion increase. The graph **(f)** shows the absolute values of the FRET signal in the somata numbered from 1 to 3 in **(d)**. 3D unit = 15 μm, scale bar = 12 μm. Imaging was performed between 80 μm to 100 μm depth in tissue, at a site with high immune cell infiltration grade (*Material S1*).
doi:10.1371/journal.pone.0060100.g005

FWHM) and to 686 ps (142 ps FWHM) (Fig. 5c) resulting from the non-linear bi-exponential evaluation (*Material S1*).

Photobleaching and photodamage

The fluorescence signal loss due to fluorophore photobleaching and the functionality and morphology loss due to tissue photodamage are limiting factors in time-lapse deep-tissue intravital microscopy in general, and in time-lapse deep-tissue intravital FLIM, in particular.

The photobleaching of Cerulean present in the neurons of *CerTN L15* mice during repeated p-TCSPC imaging (*Fig. S5*) over 30 minutes (60 scans and 20 3D FLIM-images) was similar to that

measured by standard TPLSM [35] under similar experimental conditions (*Material S1*).

Using the p-TCSPC setup we could perform FLIM over at least 2 hours in the brain stem of anesthetized healthy *CerTN L15* mice without observing any changes in the cellular calcium level (data not shown). Since the calcium level is a sensitive indicator of neuronal vital function [50], we conclude that p-TCSPC FLIM does not induce functionally discernible tissue photodamage.

Discussion

Although two-photon laser-scanning microscopy (TPLSM) is the most powerful tool for high-resolution intravital imaging available to date [2–5,51], it is limited in describing cellular function at the molecular level. Therefore, dynamic intravital fluorescence lifetime imaging (FLIM) is required [52–53]. Here we present a novel parallelized TCSPC (p-TCSPC) device featuring a 80 MHz average count rate, enabling us to demonstrate 4D-FLIM *in vivo*. Hence, p-TCSPC retains the optical performance and the accuracy of standard TCSPC techniques simultaneously allowing for dynamic FLIM over large regions (3D-stacks). As compared to video-rate FLIM based on gated optical intensifiers (GOI) [23] in the context of deep-tissue imaging, p-TCSPC shows, as expected, better optical and FLIM performance at a similar acquisition speed.

Our benchmarking experiments show that at high signals, exceeding single photon counting, multifocal GOI-FLIM is considerably faster than p-TCSPC-FLIM. Yet, at the low fluorescence signal intensity which is typical for deep-tissue imaging, this advantage vanishes. Decreasing the signal-to-noise ratio (SNR) leads to faster acquisition with both detectors, but also to lower FLIM accuracy. the advantage of p-TCSPC in acquisition speed over standard single-channel TCSPC devices is preserved as long as more than one photon every 8th laser pulse impinges on the photocathode, i.e. more 10^6 photons are emitted per second. As demonstrated by us, this is the case even in dynamic intravital FLIM in more than 100 µm depth withinthe spinal cord of *CerTN L15* mice. The use of hybrid point-detectors (PMT-APD) with shorter transit times and improved detection efficiency (70% at 550 nm) in combination with single-channel electronics (10 MHz), is not sufficient to perform ultrafast FLIM. The use of hybrid detectors together with parallelized electronics will solve the mentioned limitations and will constitute a breakthrough in fast and ultra-fast deep-tissue FLIM.

As expected, both single-beam scanning TCSPC setups perform better than the multifocal GOI setup as far as depth-dependent spatial resolution and signal-to-noise ratio are concerned. Interestingly, we showed that the maximum imaging depth in brain and skin tissue determined by the depth-dependent SNR is larger than that of reasonable FLIM accuracy (FWHM = 1000 ps). However, both values are up to three times larger for the TCSPC setups than for the GOI setup. Moreover, since the FLIM accuracy of the TCSPC devices, as PMT-based point-detectors, is limited only by the loss of excitation photons due to scattering, an exponential increase of the excitation power leads to increased FLIM depth in tissue. In contrast, the maximum FLIM depth of the GOI as a field-detector is mainly limited by the scattering of emitted photons. Thus, an excitation power increase would lead to larger ddSNR imaging depths, but would not allow for improvements of FLIM accuracy at deeper tissue layers.

Using the novel p-TCSPC device, we were for the first time able to precisely quantify neuronal calcium fluctuations as a read-out of neuronal dysfunction over time in response to chronic inflammation in the CNS of living *CerTN L15* mice affected by EAE.

In the context of rapid developments in transgenic mouse technology which aim to probe cellular, tissue and organ function at the molecular level *in vivo*, the development of fast, non-invasive and highly spatially and time-resolved FLIM represents a critical step. The parallelized TCSPC technique presented here allows for dynamic intravital FLIM in whole organs, and thus opens new perspectives in the investigation of cellular fate in genuine tissue environment.

Supporting Information

Figure S1 Experimental multi-photon setup for live tissue fluorescence lifetime imaging. (**a**) Set up of the multi-photon microscope used in FLIM experiments. A Ti:Sa laser and an optical parametric oscillator (OPO) are used as excitation sources for multi-photon microscopy. Their beams are separately shaped. The Ti:Sa beam is either first split by the beam multiplexer in up to 64 beamlets (multifocal scanning mode) or simply directed to the galvanometric scanner. The spatial overlap of the Ti:Sa and OPO beams is achieved by a customized dichroic mirror (DM1) before the galvanometric scanner. The beams are then directed through a system of scan (SL) and tubus lenses (TL), through a dichroic mirror (DM2), finally to the objective lens. The objective lens focuses the excitation beams into the sample and collects the fluorescence. The fluorescence light is reflected by the dichroic mirror DM3 to the parallelized TCSPC detector or transmitted through DM2 and a near-infrared (NIR) blocking filter either to the gated optical intensifier (FLIM field-detector) or to standard photomultiplier tubes (PMT). (**b**) Working principle of the parallelized TCSPC. The fluorescence photons are led by a liquid light guide to the detector, a 16-anode PMT. The signal is homogenized prior to detection. The electronic signal of the PMTs is shaped by analog electronics. The events are counted by two groups of 8 time-to-digital converters (TDC). The photon counting information from the TDCs is converted to the final histogram by a FPGA module. (**c**) Typical fluorescence decays measured with the GOI setup at an arbitrary pixel of a 100×100 pixel image within a 4:1 mixture of Rhodamine B and Rhodamine 6G (10 µM, aqueous solution) and fitted with a biexponential function (Levenberg-Marquadt algorithm). (**d**) Typical fluorescence decays measured with the p-TCSPC setup at an arbitrary pixel of a 100×100 pixel image within the same solution and fitted with the same algorithm. For both (c) and (d) the fitted parameters and the quality of the fit (χ^2_R) are given in the inset. (**e**) Fluorescence lifetime distributions of RhB and Rh6G corresponding to (c) over the 100×100 pixel image. (**f**) Fluorescence lifetime distributions of RhB and Rh6G corresponding to (d) over the 100×100 pixel image. The insets in the graphs (e) and (f) are intensity images of similar signal-to-noise ratio immediately after excitation, at the onset of fluorescence.
(PDF)

Figure S2 Benchmarking accuracy and acquisition speed in FLIM. (**a**) and (**b**): Examples of typical monoexponential fluorescence decays and fitting curves of a pixel in 10 µM Rhodamin 6G aqueous solution acquired by the GOI setup and by the p-TCSPC setup, respectively. The insets depict the fitted parameters and the quality of the fit (χ^2_R). The graphs (**c**) and (**e**) show the 400 ps time-gate of the GOI detector and the instrument response function of the p-TCSPC detector, respectively. Fluorescence lifetime distributions of 100×100 pixel images of similar SNR corresponding to the decays depicted in (a) and (b) are shown in (**d**) and (**f**). The graphs (**g**) and (**h**) depict typical monoexponential decays (100×100 pixel images of similar SNR) measured by the GOI and p-TCSPC setup, respectively, in a 10 µM solution of Rhodamin B. The fitted parameters and χ^2_R are

shown in the insets. (**i**) and (**j**): Typical biexponential fluorescence decays and fitting curves of one pixel in a 1:1 mixture of 10 µM Rhodamin B and 10 µM Rhodamin 6G aqueous solutions acquired by the GOI setup and by the p-TCSPC setup, respectively. All setup parameters are listed in *Material S1*.
(PDF)

Figure S3 Spatial resolution in FLIM. Lateral and axial profiles (**a**) and xz cross-section (**b**) of ePSF of fluorescing 200 nm beads embedded in agarose measured by the GOI and p-TCSPC detector, respectively. λ_{exc} = 800 nm, z step-size = 200 nm, $\lambda_{detection}$ = 525±25 nm. (**c**) Fluorescence images of the same region of a skin biopsy stained with FITC acquired in 20 and in 60 µm depth with the GOI and p-TCSPC detector, respectively. In 60 µm depth in skin tissue the p-TCSPC setup still depicts subcellular details, while the GOI setup sparsely restores the morphology. The FLIM image acquisition time and excitation power was similar for both setups at λ_{exc} = 770 nm and $\lambda_{detection}$ = 525±25 nm (*Material S1*, *Supplemental Setup Parameters*).
(PDF)

Figure S4 Typical evaluation algorithms using the Becker&Hickl FLIM-software for the FRET-FLIM data measured with the single-channel TCSPC based on a hybrid detector (Becker&Hickl). The time-resolved fluorescence of Cerulean in the spinal cord of healthy CerTN L15 mice is acquired at 850 nm so that no more than 10^6 photons/s are evaluated. This is required to avoid pile-up effects. Both iterative biexponential approximations by means of Levenberg-Marquardt algorithms and bilinear regressions with fixed fluorescence lifetimes of unquenched and FRET-quenched Cerulean are applied.
(PDF)

Figure S5 Photobleaching in dynamic intravital p-TCSPC FLIM. (a) Time-lapse of 3D Cerulean fluorescence images of neuronal processes in the brain stem of a *CerTN L15* mouse as acquired by p-TCSPC FLIM. λ_{exc} = 850 nm, z step-size = 2 µm, $\lambda_{detection}$ = 475±20 nm, peak laser power $3.13 \cdot 10^{5}$ mW. **(b)** Corresponding loss of the normalized Cerulean fluorescence over time, i.e. number of scans, due to photobleaching.
(PDF)

Movie S1 Neuronal response to KCl in hippocampus slices of *CerTN L15* mice measured by GOI-based FLIM. 3D movie of $a_1 \cdot 100/(a_2+a_1)$ images (FRET signal, Calcium level) in hippocampal slices of a *CerTN L15* mouse before (first image) and during perfusion with 100 mM KCl. The acquisition was performed with the GOI-based FLIM setup in the 16 beam scanning mode (*Material S1*, *Supplemental Setup Parameters*). Scale bar = 20 µm.
(ZIP)

Movie S2 Neuronal response to KCl in hippocampus slices of *CerTN L15* mice measured by p-TCSPC FLIM. 3D movie of $a_1 \cdot 100/(a_2+a_1)$ images (FRET signal, Calcium level) in hippocampal slices of a *CerTN L15* mouse before (first image) and during perfusion with 100 mM KCl. The acquisition was performed with the p-TCSPC FLIM setup in the single beam scanning mode (see *Material S1*). Scale bar = 20 µm.
(ZIP)

Movie S3 Neuronal response to direct interaction with immune cells in the brain stem of *CerTN L15* mice affected by EAE, measured by p-TCSPC FLIM. 3D movie of $a_1 \cdot 100/(a_2+a_1)$ images (FRET signal, Calcium level) in the brain stem of a *CerTN L15* mouse affected by experimental autoimmune encephalomyelitis before (first five images) and during local perfusion with 100 mM KCl. The acquisition was performed with the p-TCSPC FLIM setup in the single beam scanning mode (see *Material S1*). Scale bar = 20 µm.
(ZIP)

Material S1 In the additional Supplemental Material and Methods we describe in more detail the technical setup of the microscope, working principles of compared detectors used in experiments and sample preparation. Detailed **Supplemental Setup Parameters** regarding the FLIM benchmarking experiments, PSF, ddSNR and dynamic intravital imaging experiments are included. **Supplemental data analysis** describes the algorithms and software used for data analysis. Further relevant literature is included in Supplemental References**.**
(DOCX)

Acknowledgments

We thank O. Griesbeck for providing the *CerTN L15* transgenic mice and H.J. Fehling for the *Rosa26.tdRFP* transgenic mice. We thank R. Gühnter and N. Asselborn for excellent technical assistance. We thank Dr. Jason Millward for fruitful discussions and for critical reading of the manuscript.

Author Contributions

Conceived and designed the experiments: J-LR CB RN. Performed the experiments: J-LR CB RN. Analyzed the data: J-LR CB RN. Contributed reagents/materials/analysis tools: J-LR RN TS. Wrote the paper: J-LR VA MB RN. Edited the manuscript: HR VS FZ. Initiated and supervised the project: RN VA MB. Provided expertise in mouse handling and brain slice preperation: HR AEH. Performed experiments and provided expertise in EAE: HR AM JH VS FZ. Gave technical expertise for FLIM by time-gated field detection and parallelized TCSPC point detection: VA TS HS. Developed evaluation software RINIFLIM: J-LR.

References

1. Denk W, Strickler JH, Webb WW (1990) Two-photon laser scanning fluorescence microscopy. Science. 248: 73–6.
2. Hauser AE, Junt T, Mempel TR, Sneddon MW, Kleinstein SH, et al. (2007) Definition of germinal-center B cell migration in vivo reveals predominant intrazonal circulation patterns. Immunity. 26: 655–67.
3. Siffrin V, Radbruch H, Glumm R, Niesner R, Paterka M, et al. (2010) In vivo imaging of partially reversible th17 cell-induced neuronal dysfunction in the course of encephalomyelitis. Immunity. 33: 424–36.
4. Cahalan MD, Parker I. (2008) Choreography of cell motility and interaction dynamics imaged by two-photon microscopy in lymphoid organs. Annu Rev Immunol. 26 : 585–626.
5. Nimmerjahn A, Kirchhoff F, Helmchen F (2005) Resting microglial cells are highly dynamic surveillants of brain parenchyma in vivo. Science. 308: 1314–18.
6. Helmchen F, Denk W. (2005) Deep tissue two-photon microscopy. Nat Methods. 2: 932–40.
7. Zipfel WR, Williams RM, Webb WW (2003) Nonlinear magic: multiphoton microscopy in the biosciences. Nat Biotechnol. 21: 1369–77.
8. Elangovan M, Wallrabe H, Chen Y, Day RN, Barroso M, et al. (2003) Characterization of one- and two-photon excitation fluorescence resonance energy transfer microscopy. Methods. 29: 58–73.
9. Jares-Erijman EA, Jovin TM (2003) FRET imaging. Nat Biotechnol. 21: 1387–95.
10. Periasamy A. (2001) Fluorescence resonance energy transfer microscopy: a mini review. J Biomed Opt. 6: 287–91.
11. Levitt JA, Matthews DR, Ameer-Beg SM, Suhling K (2009) Fluorescence lifetime and polarization-resolved imaging in cell biology. Curr Opin Biotechnol. 20: 28–36.
12. Fruhwirth GO, Fernandes LP, Weitsman G, Patel G, Kelleher M, et al. (2011) How forster resonance energy transfer imaging improves the understanding of protein interaction networks in cancer biology. Chemphyschem. 12: 442–61.
13. Tsien RY (2009) Indicators based on fluorescence resonance energy transfer (FRET). Cold Spring Harb Protoc. pdb top57.

14. Heim N, Garaschuk O, Friedrich MW, Mank M, Milos R, et al. (2007) Improved calcium imaging in transgenic mice expressing a troponin C-based biosensor. Nat Methods. 4: 127–9.
15. Geiger A, Russo L, Gensch T, Thestrup T, Becker S, et al. (2012) Correlating calcium binding, Förster resonance energy transfer, and conformational change in the biosensor TN-XXL. Biophys J. 102(10): 2401–10.
16. Breart B, Lemaitre F, Celli S, Bousso P (2008) Two-photon imaging of intratumoral CD8+ T cell cytotoxic activity during adoptive T cell therapy in mice. J Clin Invest. 118: 1390–7.
17. Timpson P, McGhee EJ, Morton JP, von Kriegsheim A, Schwarz JP, et al. (2011) Spatial regulation of RhoA activity during pancreatic cancer cell invasion driven by mutant p53. Cancer Res. 71: 747–57.
18. Ducros M, Moreaux L, Bradley J, Tiret P, Griesbeck O, et al. (2009) Spectral unmixing: analysis of performance in the olfactory bulb in vivo. PLoS One. 4: e4418.
19. Roszik J, Lisboa D, Szollosi J, Vereb G (2009) Evaluation of intensity-based ratiometric FRET in image cytometry – approaches and a software solution. Cytometry A. 75: 761–7.
20. Chen Y, Mills JD, Periasamy A (2003) Protein localization in living cells and tissues using FRET and FLIM. Differentiation. 71: 528–41.
21. Peter M, Ameer-Beg SM, Hughes MK, Keppler MD, Prag S, et al. (2005) Multiphoton-FLIM quantification of the EGFP-mRFP1 FRET pair for localization of membrane receptor-kinase interactions. Biophys J. 88: 1224–37.
22. Caccia M, Sironi L, Collini M, Chirico G, Zanoni I, et al. (2008) Image filtering for two-photon deep imaging of lymph nodes. Eur. Biophys. J. 37(6): 979–87.
23. Gratton E, Breusegem S, Sutin J, Ruan Q, Barry N (2003) Fluorescence lifetime imaging for the two-photon microscope: time-domain and frequency-domain methods. J Biomed Opt. 8: 381–90.
24. Elson D, Requejo-Isidro J, Munro I, Reavell F, Siegel J, et al. (2004) Time-domain fluorescence lifetime imaging applied to biological tissue. Photochem Photobiol Sci. 3: 795–801.
25. Krishnan RV, Masuda A, Centonze VE, Herman B (2003) Quantitative imaging of protein-protein interactions by multiphoton fluorescence lifetime imaging microscopy using a streak camera. J Biomed Opt. 8: 362–7.
26. Soloviev VY, Tahir KB, McGinty J, Elson DS, Neil MAA, et al. (2007) Fluorescence lifetime imaging by using time-gated data acquisition. Appl Opt. 46: 7384–91.
27. Kumar S, Dunsby C, De Beule PA, Owen DM, Anand U, et al. (2007) Multifocal multiphoton excitation and time correlated single photon counting detection for 3-D fluorescence lifetime imaging. Opt Express. 15: 12548–61.
28. Becker W, Bergmann A, Haustein E, Petrasek Z, Schwille P, et al. (2006) Fluorescence lifetime images and correlation spectra obtained by multidimensional time-correlated single photon counting. Microsc Res Tech. 69: 186–95.
29. Wahl M, Rahn HJ, Rohlicke T, Kell G, Nettels D, et al. (2008) Scalable time-correlated photon counting system with multiple independent input channels. Rev Sci Instrum. 79: 123113.
30. Lee SJ, Escobedo-Lozoya Y, Szatmari EM, Yasuda R (2009) Activation of CaMKII in single dendritic spines during long-term potentiation. Nature. 458: 299–304.
31. Vitali M, Picazo F, Prokazov Y, Duci A, Turbin E, et al. (2011) Wide-Field Multi-Parameter FLIM: long-term minimal invasive observation of proteins in living cells. PloS One. 6(2): e15820.
32. Digman MA, Caiolfa VR, Zamai M, Gratton E (2008) The phasor approach to fluorescence lifetime imaging analysis. Biophys J. 94: L14–16.
33. Lee KC, Siegel J, Webb SE, Leveque-Fort S, Cole MJ, et al. (2001) Application of the streched exponential function to fluorescence lifetime imaging. Biophys J. 81(3): 1265–74.
34. Jo JA, Fang Q, Papaioannou T, Marcu L (2004) Novel ultra-fast deconvolution method for fluorescence lifetime imaging microscopy based on the Laguerre expansion technique. Conf. Proc. IEEE Eng. Med. Biol. Soc. 1271–4.
35. Herz J, Siffrin V, Hauser AE, Brandt AU, Leuenberger T, et al. (2010) Expanding two-photon intravital microscopy to the infrared by means of optical parametric oscillator. Biophys J. 98: 715–23.
36. Niesner R, Andresen V, Neumann J, Spiecker H, Gunzer M (2007) The power of single and multibeam two-photon microscopy for high-resolution and high-speed deep tissue and intravital imaging. Biophys J. 93: 2519–29.
37. Bakker GJ, Andresen V, Hoffman RM, Friedl P (2012) Fluorescence lifetime microscopy of tumor cell invasion, drug delivery, and cytotoxcity. Meth. Enzymol. 504: 109–25.
38. Magde D, Wong R, Seybold PG (2002) Fluorescence quantum yields and their relation to lifetimes of rhodamine 6G and fluorescein in nine solvents: improved absolute standards for quantum yields. Photochem Photobiol. 75: 327–34.
39. Magde D, Rojas GE, Seybold PG (1999) Solvent dependence of the fluorescence lifetimes of xanthene dyes. Photochem Photobiol. 70: 737–44.
40. Gu M. Advanced optical imaging theory. Springer-Verlag, Berlin, 2000.
41. Andresen V, Pollok K, Rinnenthal J-L, Oehme L, Guenther R, et al. (2012) High-resolution intravital imaging. PLOS One. 7(12): e50915.
42. Hanson KM, Behne MJ, Barry NP, Mauro TM, Gratton E, et al. (2002) Two-photon fluorescence lifetime imaging of the skin stratum corneum pH gradient. Biophys J. 83: 1682–90.
43. Murakoshi H, Lee SJ, Yasuda R (2008) Highly sensitive and quantitative FRET-FLIM imaging in single dendritic spines using improved non-radiative YFP. Brain Cell Biol. 36: 31–42.
44. Nitsch R, Bechmann I, Deisz RA, Haas D, Lehmann TN, et al. (2000) Human brain-cell death induced by tumour-necrosis-factor-related apoptosis-inducing ligand (TRAIL). Lancet. 356: 827–8.
45. Becker W, Bergmann A, Hink MA, Konig K, Benndorf K, et al. (2004) Fluorescence lifetime imaging by time-correlated single-photon counting. Microsc Res Tech. 63: 58–66.
46. McGinty J, Soloviev VY, Tahir KB, Laine R, Stuckey DW, et al. (2009) Three-dimensional imaging of Förster resonance energy transfer in heterogeneous turbid media by tomographic fluorescent lifetime imaging. Opt Lett. 34: 2772–4.
47. Strickler SJB, Berg RA (1962) Relationship between absorption intensity and fluorescence lifetime of molecules. J. Chem. Phys. 37: 814–22.
48. Hoffmann B, Zimmer T, Klocker N, Kelbauskas L, Konig K, et al. (2008) Prolonged irradiation of enhanced cyan fluorescent protein or Cerulean can invalidate Forster resonance energy transfer measurements. J Biomed Opt. 13: 031205.
49. Heim N, Griesbeck O (2004) Genetically encoded indicators of cellular calcium dynamics based on troponin C and green fluorescent protein. J Biol Chem. 279: 14280–6.
50. Hopt A, Neher E (2001) Highly nonlinear photodamage in two-photon fluorescence microscopy. Biophys J. 80: 2029–36.
51. Bajenoff M, Egen JG, Qi H, Huang AY, Castellino F, et al. (2007) Highways, byways and breadcrumbs: directing lymphocyte traffic in the lymph node. Trends Immunol. 28: 346–52.
52. Celli A, Sanchez S, Behne M, Hazlett T, Gratton E, et al. (2010) The epidermal Ca(2+) gradient: Measurement using the phasor representation of fluorescent lifetime imaging. Biophys J. 98: 911–21.
53. Behne MJ, Sanchez S, Barry NP, Kirschner N, Meyer W, et al. (2011) Major translocation of calcium upon epidermal barrier insult: imaging and quantification via FLIM/Fourier vector analysis. Arch. Dermatol. Res. 303: 103–15.

Acta Neuropathol
DOI 10.1007/s00401-015-1497-x

ORIGINAL PAPER

Tracking CNS and systemic sources of oxidative stress during the course of chronic neuroinflammation

Agata A. Mossakowski[1,2,3] · Julian Pohlan[1,3,9] · Daniel Bremer[1] · Randall Lindquist[1] · Jason M. Millward[4] · Markus Bock[7] · Karolin Pollok[3,9] · Ronja Mothes[3,9] · Leonard Viohl[3,9] · Moritz Radbruch[1,3] · Jenny Gerhard[1] · Judith Bellmann-Strobl[2,7] · Janina Behrens[2] · Carmen Infante-Duarte[4] · Anja Mähler[7] · Michael Boschmann[7] · Jan Leo Rinnenthal[3] · Martina Füchtemeier[5] · Josephine Herz[6] · Florence C. Pache[1,2,9] · Markus Bardua[1] · Josef Priller[8] · Anja E. Hauser[1,9] · Friedemann Paul[2,7] · Raluca Niesner[1] · Helena Radbruch[3]

Received: 18 August 2015 / Revised: 15 October 2015 / Accepted: 15 October 2015
© The Author(s) 2015. This article is published with open access at Springerlink.com

Abstract The functional dynamics and cellular sources of oxidative stress are central to understanding MS pathogenesis but remain elusive, due to the lack of appropriate detection methods. Here we employ NAD(P)H fluorescence lifetime imaging to detect functional NADPH oxidases (NOX enzymes) in vivo to identify inflammatory monocytes, activated microglia, and astrocytes expressing NOX1 as major cellular sources of oxidative stress in the central nervous system of mice affected by experimental autoimmune encephalomyelitis (EAE). This directly affects neuronal function in vivo, indicated by sustained elevated neuronal calcium. The systemic involvement of oxidative stress is mirrored by overactivation of NOX enzymes in peripheral $CD11b^+$ cells in later phases of both MS and EAE. This effect is antagonized by systemic intake of the NOX inhibitor and anti-oxidant epigallocatechin-3-gallate. Together, this persistent hyper-activation of oxidative enzymes suggests an "oxidative stress memory" both in the periphery and CNS compartments, in chronic neuroinflammation.

Keywords Multiple sclerosis · Oxidative stress · Neuronal dysfunction · Fluorescence lifetime microscopy · Intravital imaging · Oxidative stress memory

Introduction

Multiple sclerosis (MS) is a chronic inflammatory neurodegenerative disease characterized by multifocal infiltration of immune cells in the central nervous system (CNS). The first onset of inflammatory symptoms is called clinically isolated syndrome (CIS), and 30–70 % of CIS patients develop definitive MS [34]. In most patients MS has a

R. Niesner and H. Radbruch are equally contributing senior authors.

Electronic supplementary material The online version of this article (doi:10.1007/s00401-015-1497-x) contains supplementary material, which is available to authorized users.

✉ Raluca Niesner
niesner@drfz.de

✉ Helena Radbruch
helena.radbruch@charite.de

1 German Rheumatism Research Center, Berlin, Germany

2 Department of Neurology, NeuroCure Clinical Research Center, Clinical and Experimental Multiple Sclerosis Research Center, Charité-Universitätsmedizin Berlin, Berlin, Germany

3 Institut für Neuropathologie, Charité-Universitätsmedizin Berlin, Berlin, Germany

4 Institute for Medical Immunology, Charité-Universitätsmedizin Berlin, Berlin, Germany

5 DZNE-German Center for Neurodegenerative Diseases, Berlin, Germany

6 Department of Paediatrics I, Neonatology, University Hospital Essen, Essen 45122, Germany

7 Experimental and Clinical Research Center, Max Delbrueck Center for Molecular Medicine and Charité–Universitätsmedizin Berlin, Berlin, Germany

8 Department of Neuropsychiatry and Laboratory of Molecular Psychiatry, Charité-Universitätsmedizin Berlin, Cluster of Excellence NeuroCure and BIH, Berlin, Germany

9 Intravital Imaging and Immune Dynamics, Charité-Universitätsmedizin Berlin, Berlin, Germany

Published online: 31 October 2015

relapsing–remitting course (RRMS), which is conventionally considered to reflect mainly inflammatory processes. It can, however, subsequently evolve into a secondary progressive disease (SPMS), thought to reflect more of a degenerative process [27, 41], leading to lasting and irreversible neurological disability.

Reactive oxygen species (ROS) generated by invading and resident CNS macrophages have been implicated in mediating demyelination and axonal damage [13, 38, 55, 58, 60]. The term reactive oxygen species (ROS) refers to both free radicals and related molecules. There is evidence pointing to excessive ROS production as a major mechanism causing damage in MS, as oxidized DNA, lipids and proteins were reported in CNS lesions, cerebrospinal fluid and plasma of MS patients [17, 21, 31]. To prevent ROS-caused damage, cells have potent anti-oxidative mechanisms. However, defects in anti-oxidant mechanisms and excessive ROS production that overwhelms the endogenous anti-oxidant capacity lead to oxidative stress. The most abundant source of ROS leading to oxidative stress is the respiratory burst, which is mediated by the nicotinamide adenine dinucleotide phosphate (NADPH) oxidases [NOX1, NOX2 (phox), NOX3, NOX4, DUOX1, DUOX2] [5]. The NOX enzymes catalyze the oxidation of molecular oxygen to its highly reactive anion O_2^-. Recently, significant up-regulation of NOX2 as well as histological co-localization of cytosolic and membrane-bound NOX2 subunits have been described in MS, at lesion sites [13, 59]. Additionally, subunits of NOX2 are up-regulated in active lesions in experimental autoimmune encephalomyelitis (EAE), an animal model of MS [45]. Furthermore, other members of the NADPH oxidase family, including NOX1 and NOX4 have the capacity to cause oxidative stress in the CNS [11, 30, 36, 43, 49]. NOX1 subunits have been described in active lesions in MS tissue in microglia/macrophages as well as in astrocytes [13], and inhibition of NOX enzymes [9] and knockout of isotype-specific as well as isotype-common NOX subunits (gp91 [29], p47 [57]) decreased EAE severity and incidence. This suggests that NOX enzymes in general are major contributors to oxidative stress by catalyzing the production of ROS, thus leading to CNS tissue damage. However, up to now, neither the catalytic activity of NOX enzymes leading to oxidative stress nor their cellular sources could be tracked, in vivo in the CNS and in the periphery.

Given the increasingly recognized importance of oxidative stress in MS pathogenesis, anti-oxidant drugs are emerging as new therapeutic approaches [15]. One potential candidate is epigallocatechin-3-gallate (EGCG), a polyphenol present in green tea. We and others have shown that EGCG ameliorates EAE [2, 19, 22, 33, 61], and clinical trials testing the benefits of EGCG in MS patients are ongoing (NCT00525668, NCT00799890 and NCT01417312). There is in vitro data pointing to the inhibition of ROS production through EGCG [63]. It is known that EGCG competes with NADPH but not with NADH in binding to NADH-/NADPH-dependent enzymes [46]. However, the therapeutic effects of EGCG in vivo have not yet been analyzed on a cellular level.

Developed two decades ago, fluorescence lifetime imaging (FLIM) has proven to be a reliable, quantitative tool to probe cellular parameters [1, 12, 24, 25, 35, 53]. In particular, the possibility to quantify the endogenous fluorescence of NAD(P)H or of flavoproteins has made FLIM an especially versatile probe of metabolic function [26, 51, 52], as this marker-free approach allows for the acquisition of unaltered, real-time data. Despite its power as a quantitative technique, FLIM requires a high fluorescence signal and thus could not be applied to deep-tissue imaging until recently [4]—a limitation which is particularly relevant to intravital imaging of protected, hardly accessible organs like the CNS [44]. In our previous work, we demonstrated that, in the context of oxidative stress, the increase of fluorescence lifetime of NAD(P)H is specific for NADPH (and not NADH) binding to members of the NOX family, both in murine polymorphonuclear cells [37] and in plant cells (*Nicotiana tabacum*) (unpublished data). These results are supported by recent studies showing the same increase in NAD(P)H fluorescence lifetime, in a more general context [6]. When using NAD(P)H-FLIM, all NADH- and NADPH-dependent enzymes which participate in biochemical reactions within the cell are simultaneously detected (up to several hundred enzymes). Thus, the activation of NOX enzymes can be unequivocally detected only at sites where these enzymes preferentially bind the present coenzymes. The catalytic activity corresponding to such a situation implies an excessive ROS production, and thus oxidative stress, rather than a low, e.g., immunomodulatory, ROS production.

In the present study, we observe a spatio-temporal correlation between the catalysts of oxidative stress (activated NOX enzymes) and neuronal damage in the CNS of mice affected by EAE. Furthermore, we validate this technique in the CNS by identifying macrophages and activated microglia as major cellular sources of activated NOX enzymes, and thus of oxidative stress, in the brain stem of mice with EAE. Using this novel technique, we show for the first time that astrocytes are also major contributors in generating oxidative stress in the CNS during chronic EAE. Additionally, we offer insight into the systemic dimensions of both EAE and MS by quantifying the activity of NADPH oxidases in peripheral monocytes, from the first presentation of symptoms to the chronic phase of the disease. This marker-free approach allows the direct monitoring of the therapeutic mechanism of the anti-oxidative drug EGCG in humans at a cellular and even sub-cellular level.

Methods and materials

Two-photon laser-scanning microscopy (TPLSM)

FLIM experiments were performed using a specialized two-photon laser-scanning microscope based on a commercial scan head (TriMScope, LaVision BioTec, Bielefeld, Germany) [20, 44]. The detection of the fluorescence signals was accomplished either with photomultiplier tubes in the ranges 460 ± 30, 525 ± 25, 593 ± 20 nm or with a 16-channel parallelized TCSPC detector (FLIM-X_{16}, LaVision BioTec, Bielefeld, Germany) in the range 460 ± 30 nm. The excitation of NADH and NADPH was performed at 760 nm (detection at 460 ± 30 nm), of Cerulean (detection at 460 ± 30 nm), sulforhodamine 101 (detection at 593 ± 20 nm) and EGFP (detection at 525 ± 25 nm) at 850 nm and of tdRFP either at 930 nm or at 1110 nm (detection at 593 ± 20 nm). Citrine was detected at 525 ± 25 and 593 ± 20 nm.

For both intensity and fluorescence lifetime imaging we used an average maximum laser power of 8 mW to avoid photodamage. The experimental parameters for FLIM were 160 ps histogram bin (for NAD(P)H-FLIM) and 80 ps histogram bin (for FRET-FLIM) and maximum acquisition time for a 512 × 512 image was 5 s to record a fluorescence decay stack (Suppl. Fig. 3). The time window in which the fluorescence decays were acquired was set to 9 ns.

Data analysis

FLIM data analysis was performed using self-written software based on Levenberg–Marquardt algorithms for non-linear fitting as well as the phasor approach (Suppl. Fig. 6).

Statistical analysis and graphical presentation was carried out with GraphPad Prism 4 (Graphpad Software, USA) and OriginPro (OriginLab, USA). Results are shown as mean values from analyzed data in one mouse/human, in addition the mean ± SD summarize collective data from performed experiments.

Mice

All mice used were on a C57/Bl6 background. The *CerTN L15 x LysM tdRFP* mouse expresses a FRET-based calcium biosensor consisting of Cerulean (donor) and Citrine (acceptor) bound to troponin C, a calcium-sensitive protein present in certain subsets of neurons [18]. Mice carrying the CerTN L15 reporter were crossed to the LysM tdRFP mice, in which tdRFP [32] is expressed in $LysM^+$ cells [10], yielding progeny with both reporters. The $CX_3CR1^{+/-}$ *EGFP* mouse [23] was used to detect microglia, whereas the $CD4^+$ *YFP* mouse strain was used to detect $CD4^+$ T cells [28, 50]. EAE induction protocol and EAE course of these mice can be found in Table 2, Supplemental Material.

Preparation of the brain stem window for intravital imaging

The preparation of the imaging field was similar to our previous description [47, 48]. For a detailed description, see Supplemental Material. In each imaged animal the whole area that was accessible by intravital imaging was scanned and all visible lesions of each animal were analyzed as well as at least one "normal appearing" imaging field. Animal experiments were approved by the appropriate state committees for animal welfare (G0198/11 and G0181/10, LAGeSo—Landesamt für Gesundheit und Soziales Berlin) and were performed in accordance with current guidelines and regulations.

Human samples

Venous blood samples were obtained with informed consent after the nature and possible consequences of the studies were explained. We included healthy controls, patients with untreated clinically isolated syndrome (CIS), patients with relapsing remitting MS (RRMS-GA) in a randomized double-blind clinical trial medicated with glatiramer acetate receiving additional 600 mg of EGCG or placebo, patients with relapse and remitting MS not treated with any immunomodulatory drugs (RRMS), and patients with a secondary progressive disease course (SPMS); further detailed information can be found in Table I, Supplemental Material. Peripheral blood mononuclear cells (PBMCs) were isolated using standard protocols and $CD11b^+$-enriched by MACS selection (Miltenyi Biotec, Bergisch Gladbach, Germany) according to the manufacturer's protocol. The purity was assessed by flow cytometry. The MACS-enriched $CD11b^+$ monocytes were injected into specifically fabricated chambers and incubated in phenol-free RPMI at 37° C for one hour prior to imaging.

Further experimental details are available in Supplemental Methods.

Results

Activation of NOX enzymes measured by intravital NAD(P)H fluorescence lifetime imaging pinpoints the origin of oxidative stress and correlates with immune infiltration and neuronal dysfunction in EAE

To detect and quantify NOX enzymes activation in vivo, we induced EAE in mice and imaged their brainstem

intravitally. Consistent with previous reports [38], we detected elevated ROS concentrations (~200 µM) in the brain stem of mice affected by EAE at the peak of disease, compared to disease-free control animals (Fig. 1a). ROS were detected by intravital imaging of murine brainstems which had been previously superfused with a 100 µM solution of Amplex Red®. The Amplex Red® calibration was performed using a H_2O_2 concentration series (Suppl. Fig. 2).

As the main catalysts of O_2^- production (precursor of ROS) the membrane-bound NOX enzymes (NOX1,2,3,4 and DUOX1,2) directly contribute to oxidative stress. By employing intravital NAD(P)H fluorescence lifetime imaging (FLIM) we detected the activation of NOX enzymes in the brainstem of EAE mice (Table 2). From the fluorescence intensity decay of NAD(P)H, we evaluated the fluorescence lifetime of enzyme-bound NAD(P)H at each pixel of the image in different layers of the brainstem between 30 and 150 µm depth, as described in Supplemental Material. We expected a mean fluorescence lifetime between 1.1 and 2.7 ns for NAD(P)H bound to metabolic enzymes responsible for basic cellular functions (Suppl. Fig. 4) and a fluorescence lifetime of approximately 3.65 ns for NADPH bound to NOX enzymes as calculated with two independent evaluation methods [37] (Supplemental Material, Suppl. Figs. 4 and 6). Free NAD(P)H has a fluorescence lifetime of approx. 400 ps and is easily distinguished from enzyme-bound NAD(P)H.

The specific NAD(P)H fluorescence lifetime ("NOX only" gate set at 3.3–3.9 ns) corresponding to activated NOX enzymes was detectable in EAE mice mainly within those brainstem regions that included immune cell infiltrations ($LysM^+$tdRFP or $CD4^+$YFP cells, Movie 1); that is, NOX enzymes overactivation was detected in acute lesions, but could not be detected in "normal appearing" areas in the same animal (peak disease, score 2.5, Fig. 1b, c).

The area of NOX-specific activation in acute lesions in the brainstem was significantly enlarged, both at the onset of clinical signs, with a mean of 5 ± 1.5 % in the field of view (300 × 300 µm^2), and at the peak of disease, with a mean area of 14.9 ± 5.8 %, as compared to healthy animals, with a mean area of 2.2 ± 0.9 % (Fig. 1e).

By performing intravital FRET-FLIM in the brain stem of *CerTNL15xLysMtdRFP* mice with EAE, we were able to confirm and extend our previous results indicating neuronal dysfunction during the disease (Fig. 1d, f). We showed previously that elevated Ca^{2+} concentrations over 1 µM in these mice over a period of 1 h reliably indicate neuronal dysfunction [48]. Here, we confirm this finding by showing that neuronal and axonal calcium is increased in areas adjacent to immune infiltrates. Additionally, after 2 h of intravital monitoring, the sites of increased axonal calcium showed axonal disintegration (Fig. 1h). Both the TN L15 construct decay time and the acquisition time of the FRET-FLIM technique are in the range of several 100 ms, allowing for recording time-averaged calcium concentrations relevant for the pathologic dysfunction of neurons. They are, however, both too slow to monitor neuronal calcium transients.

By simultaneously performing NAD(P)H-FLIM and FRET-FLIM in the brainstems of mice with EAE,

Fig. 1 Activation of NADPH oxidases in the CNS pinpoints oxidative stress. Oxidative stress is dependent on disease severity and correlates with cellular inflammation and neuronal dysfunction. ROS concentration in the brain stem of a healthy mouse compared to a mouse affected by EAE at peak of disease (score 2.0) (**a**). Amplex Red® was used as ROS indicator. $\lambda_{exc} = 910$ nm, $\lambda_{em} = 525 \pm 25$ nm (Thy1-Citrine in neurons depicted in *green*), $\lambda_{em} = 593 \pm 20$ nm (Amplex Red®), *scale bar* 50 µm. **b** Correlated 300 × 300 µm^2 (517 × 517 pixel) fluorescence intensity images [Thy1 = *green* (neurons), LysM = *red* (macrophages)], **c** enzyme-bound NAD(P)H-FLIM maps (τ_2-maps) and **d** neuronal Ca^{2+} maps as recorded by FRET-FLIM in three different regions of the brain stem of a *CerTN L15 x LysM tdRFP* mouse with EAE, at the peak of the disease, score = 2.5. *First row* normal appearing white matter; *second row* margin of lesion; *third row* lesion center. The activation of the NADPH oxidases (NOX) assessed by NAD(P)H-FLIM (**c**) correlates with $LysM^+$ tdRFP cell infiltrate in the CNS (**b**) and with elevated neuronal calcium (**d**), indicating neuronal dysfunction. *Scale bars* in **b**, **c** and **d** = 30 µm. The τ_2-maps show the false color-encoded fluorescence lifetime τ of enzyme-bound NAD(P)H at each recorded pixel of the image. NAD(P)H bound to metabolic enzymes are depicted in blue and green (τ between 1 and 3 ns) whereas, under oxidative stress, NADPH bound to activated NOX appears in red (τ between 3.3 and 3.9 ns, "NOX only" gate). **e** Quantification of the NOX activation area within lesions defined by $LysM^+$ cell infiltration, i.e., ratio of the area of NOX only gate to the total tissue area, 4.98 ± 1.53 % at the onset of clinical signs (day 1–2 after appearance of first clinical signs, EAE scores 0.5–1.0) and 14.88 ± 5.81 % of the tissue area at peak of disease (day 3–5 after onset of clinical symptoms, EAE scores 1.5–2.5) as compared to 2.19 ± 0.94 % in healthy controls. Six independent EAE experiments (EAE onset $n = 6$, EAE peak $n = 12$ healthy controls $n = 3$), see Table 2. **f** Quantification of elevated neuronal calcium area is assessed by FRET-FLIM relative to the total neuronal area. Data display means of imaging fields of individual animals from two independent EAE experiments (healthy controls $n = 3$, EAE onset $n = 3$, EAE peak $n = 4$). The increased NOX activity correlates with an increased area of elevated neuronal calcium ("$Ca^{2+} > 1$ µM" gate) at the time of EAE onset (1.32 ± 0.78 %) and at peak disease (12.80 ± 2.41 %), as compared to healthy controls (0 %, $n = 3$, mean calcium concentration 170 nM, maximum calcium concentration 450 nM). **g** Correlation between NOX enzymes activation area and increased neuronal calcium area at lesion sites and non-infiltrated sites in the brain stem of *CerTN L15 x LysM tdRFP* mice affected by EAE. **h** Pathologically increased neuronal calcium level (>1 µM calcium) correlates with immune cell infiltrate and, after 2 h, with axonal break-down as shown by intravital images in the brain stem of a *CerTN L15* mouse affected by EAE (peak)—*scale bar* 10 µm. All images are acquired in the region 30–150 µm depth within the brain stem (300 × 300 × 50 µm^3, z-step = 2 µm). For the statistic evaluation in **e** and **f** we applied ANOVA tests (*$p < 0.05$, **$p < 0.01$, ***$p < 0.001$)

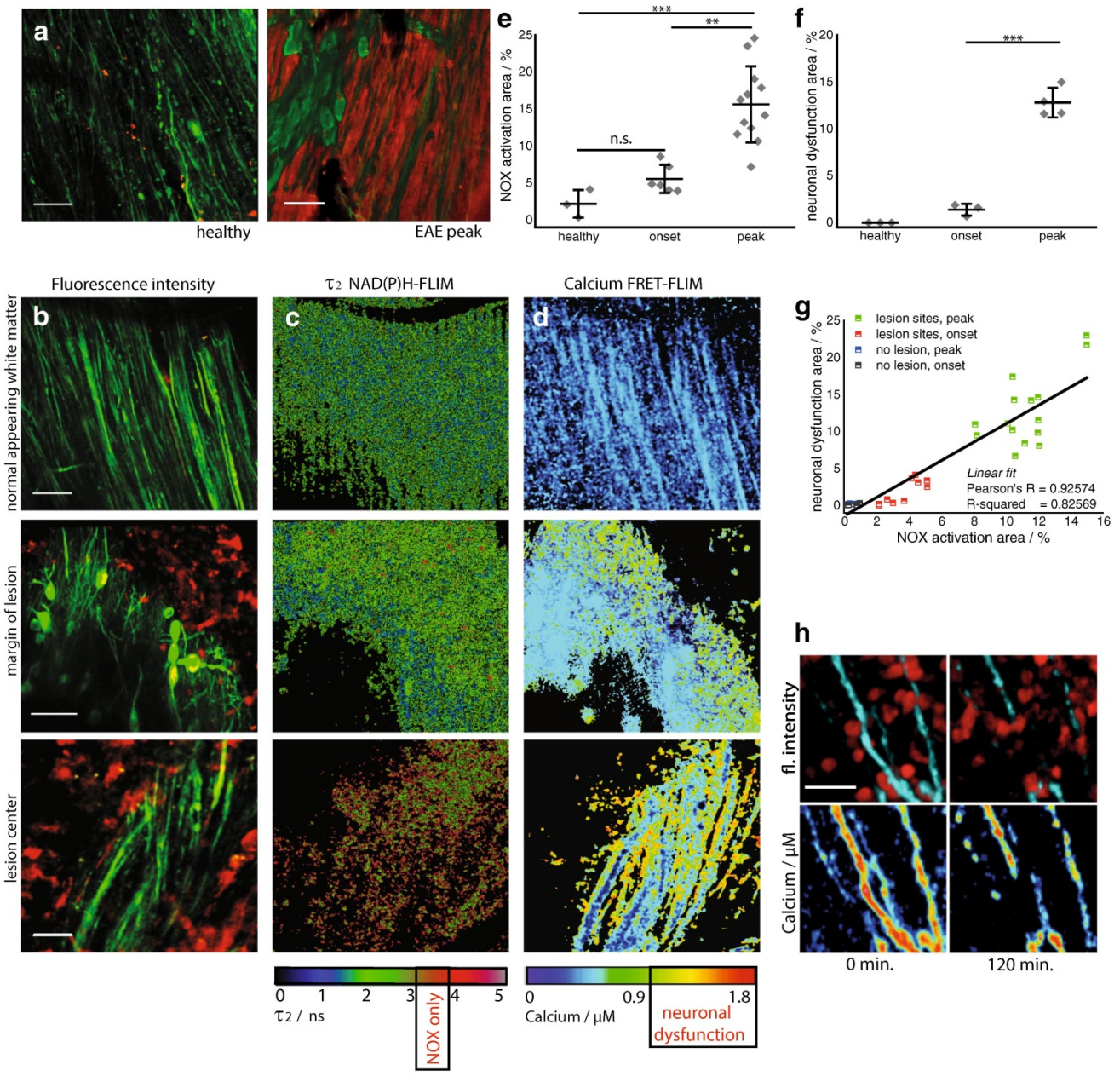

we found that the increased NOX activation correlated with an extended area of elevated neuronal calcium ("Ca^{2+} >1 µM" gate) at EAE onset (1.3 ± 0.8 %) and at peak disease (12.8 ± 2.4 %), as compared to control mice (0 %) (Fig. 1g). The high spatial correlation between areas of NOX enzymes activation and increased neuronal calcium indicating early neuronal dysfunction (Pearson's *R* coefficient over 0.9) in EAE is depicted in Fig. 1g. Interestingly, at lesion sites, both the overactivation of NOX enzymes and the neuronal dysfunction were generally lower at onset than at disease peak. The areas of NOX enzymes activation and increased calcium values were determined as mean values of 3–12 acute lesions per mouse. Each data point in Fig. 1e, f represents the average value for each individual mouse.

Cellular origins of oxidative stress in EAE

We verified the capacity of intravital NAD(P)H-FLIM to identify the cellular origins of oxidative stress directly in the CNS by confirming the contributions of macrophages and activated microglia, which are well-known contributors to the activation of NOX enzymes during EAE. Subsequently, we used the unique versatility of this technique to identify novel cellular sources of oxidative stress by performing endogenous NAD(P)H-FLIM in the CNS

of EAE mice with a variety of fluorescently labeled cell subsets. Here, we evaluated the relative contributions of each cell type ($LysM^+$tdRFP, CerTNL15, $CD4^+$YFP, $CX_3CR_1^{+/-}$EGFP or sulforhodamine101 labeled cells) to the total area of NOX enzymes activity.

Characterization of cellular markers

The reliability of the chosen cellular markers used in the intravital experiments was verified by flow cytometry or histology in mice affected by EAE. While in healthy $LysM^+$tdRFP animals only rare $tdRFP^+$ cells can be found in the CNS, during EAE ($n = 4$) the $tdRFP^+$ compartment increased markedly at lesion sites. Of the $tdRFP^+$ cells, 65 % were $CD45^{high}CD11b^+Ly6G^-$ (macrophages), 25 % $CD45^{low}$-$CD11b^+$ (microglia) and 7 % $CD45^{high}CD11b^+Ly6G^+$ (neutrophil granulocytes) (Fig. 2a). The overlap of $LysM^+$tdRFP cells with $CX_3CR_1^+$ cells was quantified by flow cytometry using an anti-CX_3CR_1 antibody. 17.8 ± 8.9 % of all $LysMtdRFP^+$ cells were $CX_3CR_1^+CD45^{low}$ (microglia) and 27.6 ± 10.1 % were $CX_3CR_1^+CD45^{high}$ (macrophages). This represented only a minority of the total $CX_3CR_1^+$ cells as displayed in the 2.8 ± 1.4 % of cells that co-expressed LysM-tdRFP ($n = 3$) (Fig. 2b).

In disease-free control animals, sulforhodamine 101 (sulforh101) specifically labels astrocytes in the cortex [39, 40]. To characterize the cells labeled with sulforh101 during EAE in the brainstem we analyzed by immunofluorescence intracellular sulforh101 (following i.v. injection) as well as GFAP and CD11b expression. Minimal co-localization (6.1 ± 1.4 %) of sulforh101 labeling with CD11b staining could be observed at EAE lesion sites in the brainstem (Fig. 2c). We detected sulforh101 co-localization mainly with $GFAP^{low}$ cells [16] but not with $GFAP^{high}$ cells (Fig. 2d). 80 ± 6 % of sulforh101-labeled cells were $GFAP^+$, whereas this cell population represents only half of all GFAP-expressing cells (Fig. 2d). Intravital imaging data recorded in the brainstem of $CX_3CR_1^{+/-}$EGFP mice additionally labeled with sulforh101 showed negligible overlap between the EGFP and sulforh101 labeling, typically 2 ± 1.5 %, both in healthy controls and in mice affected by EAE (Fig. 3a). The lesions investigated by intravital imaging in the brainstem showed typical EAE characteristics, which we confirmed by histology (Suppl. Fig. 1).

Phagocytic capacity of astrocytes and their potential role in EAE

We focused on astrocytes as potential contributors to oxidative stress during neuroinflammation as they are known to have phagocytic capacity. Morphological analysis of our intravital experiments revealed a disruption of the fine process-rich astrocytic network typically found in healthy control animals (Fig. 3a), similar to that which could be seen on histological staining (Fig. 2). The disruption of the astrocytic network was associated with changes towards a reactive phenotype and glial scar formation at lesion sites, with dense accumulations of astrocytic end feet and processes lining up along the vessels and around inflammatory cells ($CX_3CR_1^+$) in EAE (Figs. 2d, 3a).

Furthermore, NAD(P)H-FLIM analysis in astrocytes using beads for phagocytosis coated with *Staphylococcus aureus* fragments (pHrodo) in mixed cell cultures with microglia showed increased NAD(P)H fluorescence lifetime typical of NOX enzymes activity. We could correlate increased NOX enzymes activation with the localization of phagocytosed pHrodo beads (red) (Fig. 3b).

As the expression of p22 NOX subunit in astrocytes during EAE is only sparse [45], we investigated Noxo1 expression by immunofluorescence to address the question which NOX enzyme could be responsible for the observed NAD(P)H lifetime prolongation. NOX1 function is less dependent on p22 coexpression compared to other isoforms [54]. We could detect in $GFAP^{high}$ cells and $GFAP^{low}$ cells Noxo1 expression (Fig. 3c, d) including $GFAP^{low}$ and sulforh101-co-labeled cells (Fig. 3g) in EAE lesions. Furthermore, Noxo1 was also found in $CD11b^+$ cells (with both phagocytic and microglial morphology) (Fig. 3e).

Altogether, these data suggest that astrocytes generate oxidative stress within the CNS during the course of chronic neuroinflammation.

Astrocytes are major cellular contributors to oxidative stress in EAE

We quantified the contribution of specific cell types to the total area of NOX enzymes activity in the CNS using the cellular markers described above. In line with previous studies, we found that the mean contribution of $LysM^+$ cells amounted to 22.7 ± 6.4 % at onset, and 28.2 ± 4.7 % at the peak of EAE. Additionally, the mean contribution of $CX_3CR_1^+$cells amounted to 13.1 ± 2.3 % at onset, and 17.4 ± 2.4 % at the peak of EAE. Macrophages and microglia (either $LysM^+$ and/or $CX_3CR_1^+$) together constitute the main source of oxidative stress at onset and peak of the disease (Fig. 4d). This finding confirms the reliability of our method to evaluate oxidative stress by detecting the activation of NOX enzymes.

Using this novel approach, we found that although microglia and macrophages are the main sources of NOX enzymes activity, a significant fraction could not be attributed to those cell types. Surprisingly, we found that astrocytes (sulforhodamine 101-labeled cells [3]) accounted for 26.4 ± 4.4 and 34.2 ± 5.6 % of total area of NOX enzymes overactivation at onset and peak of EAE, respectively (Fig. 4d). In this model, the contribution of astrocytes to

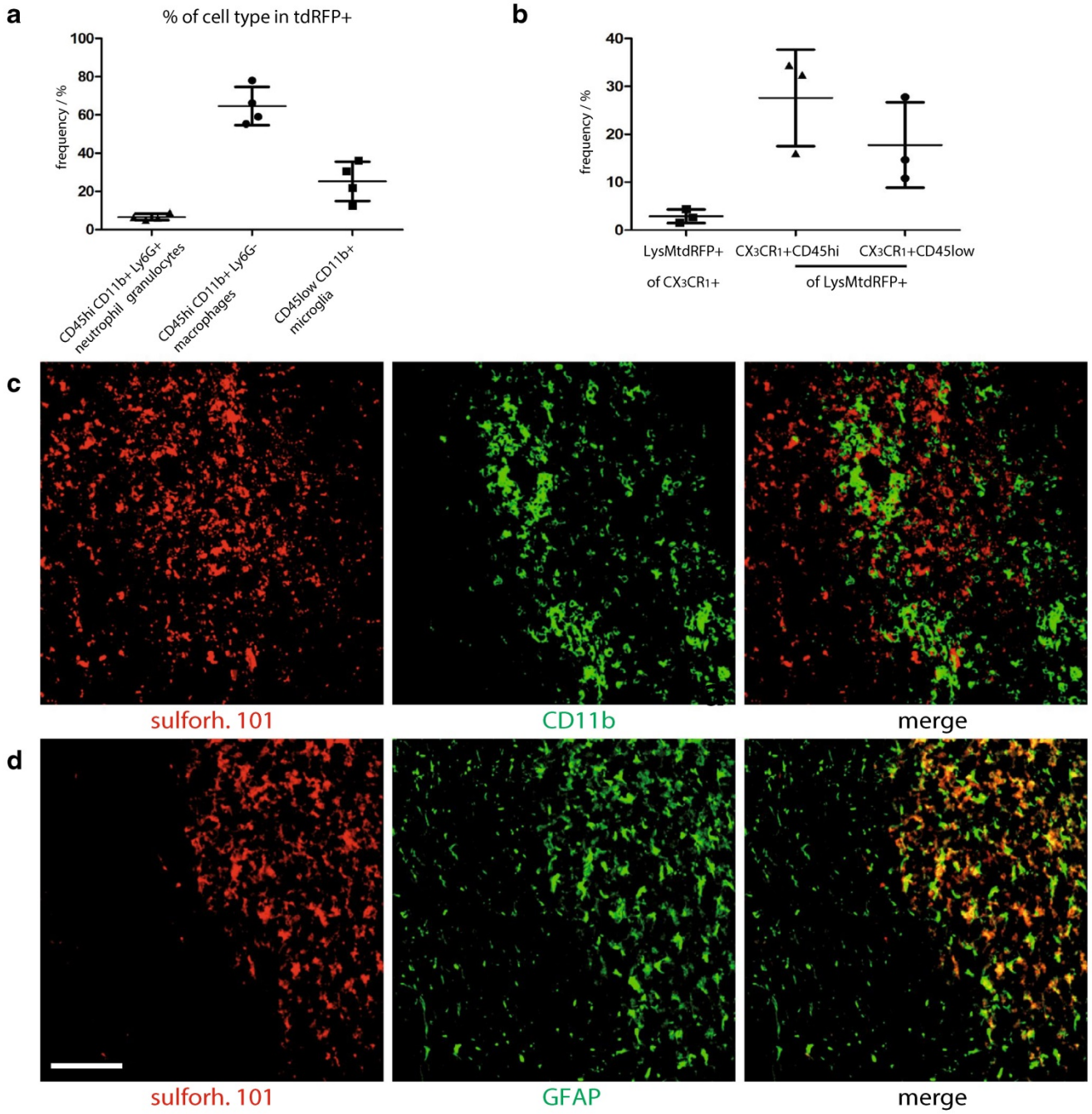

Fig. 2 Characterization of active lesions as well as of LysMtdRFP$^+$ and sulforhodamine 101 labeled cells during EAE. **a** FACS analysis data in the CNS of LysM$^+$tdRFP mice at peak EAE, characterizing the tdRFP$^+$ cell population ($n = 4$). **b** FACS analysis data in the CNS of LysM$^+$tdRFP mice ($n = 3$) at peak EAE showing the overlap of LysMtdRFP and CX_3CR_1-antibody labeled cells. **c** Immunofluorescence images within the brain stem of a C57Bl6 mouse affected by EAE, at peak of the disease, showing no co-localisation between sulforhodamine 101 (*red*) and CD11b$^+$ cells (*green*) at infiltration sites. **d** Immunofluorescence images within the brain stem of the same mouse, showing colocalization between sulforhodamine 101 (*red*) and GFAP$^+$ cells (*green*) at reactive gliosis sites. *Scale bar* 200 µm

oxidative stress within the CNS is comparable to that of the labeled macrophages and microglia together, thus identifying astrocytes also as central contributors to oxidative stress in the acute phases of EAE.

The mean contribution of CD4$^+$cells to NOX enzymes activity was negligible, amounting to 3.6 % at peak disease, comparable to the mean contribution of neurons with 2.3 % at onset and 3.8 % at peak of EAE (Fig. 4d).

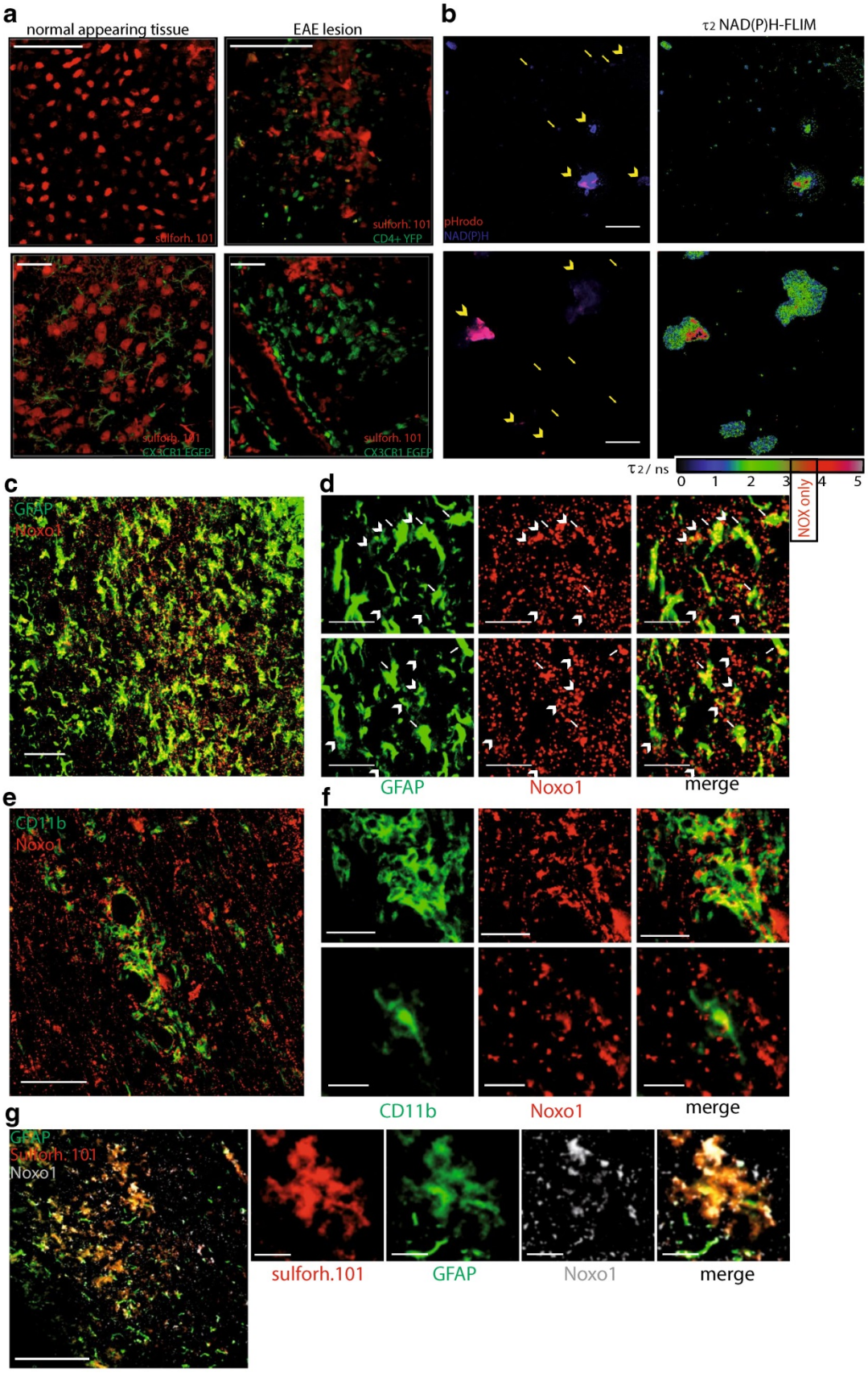
a
normal appearing tissue
EAE lesion
sulforh. 101
sulforh. 101
CD4+ YFP
sulforh. 101
CX3CR1 EGFP
sulforh. 101
CX3CR1 EGFP
b
τ2 NAD(P)H-FLIM
pHrodo
NAD(P)H
τ2 / ns
0 1 2 3 4 5
NOX only
c
GFAP
Noxo1
d
GFAP
Noxo1
merge
e
CD11b
Noxo1
f
CD11b
Noxo1
merge
g
GFAP
Sulforh. 101
Noxo1
sulforh.101
GFAP
Noxo1
merge

◀**Fig. 3** Astrocytes as phagocytes and their potential role in EAE. **a** 3D fluorescence intensity images were acquired in the brain stem of $CD4^+$ YFP mice: healthy controls (*upper*, *left panel*) and at a lesion site, in EAE (*upper*, *right panel*) [$CD4^+$ cells (YFP) = *green*, astrocytes (sulforhodamine 101) = *red*]. *Scale bar* 100 µm. Similarly, 3D fluorescence intensity images were acquired in the brain stem of $CX_3CR_1^{+/-}$ EGFP mice: healthy controls (*lower*, *left panel*) and at the lesion site in EAE (*lower*, *right panel*) [microglia/macrophages (EGFP) = *green*, astrocytes (sulforhodamine 101) = *red*]. *Scale bar* 30 µm. **b** NAD(P)H fluorescence images (*blue*) of mixed astrocytes (*arrow head*) and microglia (*arrows*) cell cultures phagocytosing *Staphylococcus aureus* beads (pHrodo, *red* after uptake) are shown on the *right side*. Corresponding NAD(P)H-FLIM maps (τ_2-maps) shown on the *left side* reveal the correlation between phagocytosis of pHrodo beads and the typical increase of fluorescence lifetime in astrocytes indicating the activation of NOX enzymes. **c** Immunofluorescence overview image within the brain stem of a mouse affected by EAE indicating the distribution of Noxo1 (subunit of NOX1, *red*) and GFAP signal (*green*). *Scale bar* 100 µm. **d** Zoom ins of **c** demonstrating that Noxo1 is found both in $GFAP^{high}$ cells (indicated by *white arrows*) and $GFAP^{low}$ cells (indicated by *white arrow heads*) in the CNS of mice affected by EAE. *Scale bar* 30 µm. **e** Immunofluorescence overview image within the brain stem of a mouse affected by EAE indicating the distribution of Noxo1 (subunit of NOX1, *red*) and CD11b signal (*green*). *Scale bar* 150 µm. **f** Zoom ins of **e** demonstrating that Noxo1 is found in $CD11b^+$ cells (with both phagocytic and microglial morphology). *Scale bar* 40 µm (*upper panels*), *scale bar* 20 µm (*lower panels*). **g** Immunofluorescence overview image within the brain stem of a mouse affected by EAE indicating the distribution of Noxo1 (subunit of NOX1, *gray*), GFAP signal (*green*) and sulforh101 signal (*red*). *Scale bar* 200 µm. **h** Zoom in of **g** demonstrating that Noxo1 is found in $GFAP^{low}$, sulforh101-labeled cells. *Scale bar* 30 µm

We further analyzed the fraction of activation within each cell subset by calculating the percentage of the specific cell area that shows NOX enzymes activation, as well as averaged values per mouse displayed in Fig. 4e. The area of NOX enzymes activation within neurons ($Thy1^+$ cells in *LysM*$^+$*tdRFPxCerTNL15* mice) was very small, both at clinical onset and at peak of disease with less than 2 %. Conversely, in $LysM^+$tdRFP cells the area of NOX enzymes activation was generally higher with 8 % at clinical onset and rising significantly to 27 % at peak disease (Fig. 4e). The area of NOX enzymes activation in $CX_3CR_1^{+/-}$EGFP cells was 11 and 14 %, respectively. We obtained similar data in astrocytes with 12 % at onset and 10 % in peak. In $CD4^+$YFP cells, the area of NOX enzymes activation was low at peak of disease, amounting to only 3 %.

In our experimental setup, not all cells of the specific cell subtype are fluorescently labeled also due to the use of heterozygous fluorescent mouse strains, but we could address the majority of cells with our labeling strategy. The remaining percentage of NOX enzyme activation area that was not associated with labeled cells in this model (12.85 % at peak, 35.46 % in onset of EAE) is probably due to unlabeled macrophages, microglia and/or astrocytes. The contribution of other immune or CNS-specific cell types, such as oligodendrocytes or immune cells with phagocytic capacity, to the generation of oxidative stress cannot be completely excluded but is expected to be low.

Soluble factors drive activation of NADPH oxidases in EAE

Regarding the co-localization of neuronal structures ($Thy1^+$ cells) and $LysM^+$ cells in *CerTNL15xLysMtdRFP* mice, we found that only a 28 to 30 % of the co-localized area was associated with increased NOX enzymes activation in EAE (Fig. 4f, h). The normalized co-localization index, calculated as we previously described [48] indicated significantly more extensive interaction between neurons and macrophages at peak disease than at the time of onset (Fig. 4g), independently of the number of neurons or macrophages at the imaged site. Thus, while the interactions between neurons and $LysM^+$ cells were more extensive with the progression of the disease, NOX enzymes activation was not specifically induced by neurons or by their direct interaction with $LysM^+$ cells. On the other hand, we showed that upon applying glutamate (300 µM) locally to the brainstem of healthy mice, the NOX enzymes activation area increased from values typical for control animals (0.7 ± 0.2 %) to values similar as those reached in peak of EAE (11.9 ± 3.1 %) (Suppl. Fig. 5), indicating that glutamate-induced excitotoxicity can lead to similar levels of NOX enzymes activation as are present in acute EAE lesions. These data support the interpretation that the cause of NOX enzymes activity in macrophages, activated microglia and astrocytes within the CNS in EAE is not necessarily triggered by direct contact to CNS components like axons, but is rather associated with soluble factors, such as glutamate or inflammatory mediators.

NOX is overactivated in peripheral $CD11b^+$ monocytes in both MS and EAE and can be ameliorated by systemic administration of EGCG

To translate our findings to MS, we isolated $CD11b^+$ monocytes from peripheral blood mononuclear cells (PBMC) taken from MS patients, at different stages of the disease, including CIS, RRMS and SPMS. In healthy humans and healthy mice, $CD11b^+$ monocytes were not activated after isolation, i.e., the area of NOX activation amounted to 3.4 ± 0.6 and 3.4 ± 1.9 %, respectively. In untreated RRMS patients, the area of NOX activation was 18.3 ± 2.5 %, in mice at peak of EAE, the NOX activation area was 18.5 ± 3.5 %. The high levels of NOX activation in peripheral $CD11b^+$ cells of mice with EAE and of untreated RRMS patients could be ameliorated by treatment with glatiramer acetate (GA) alone, to only 10.8 ± 2.8 % (in RRMS patients). Upon combination treatment with both GA and additional systemic administration

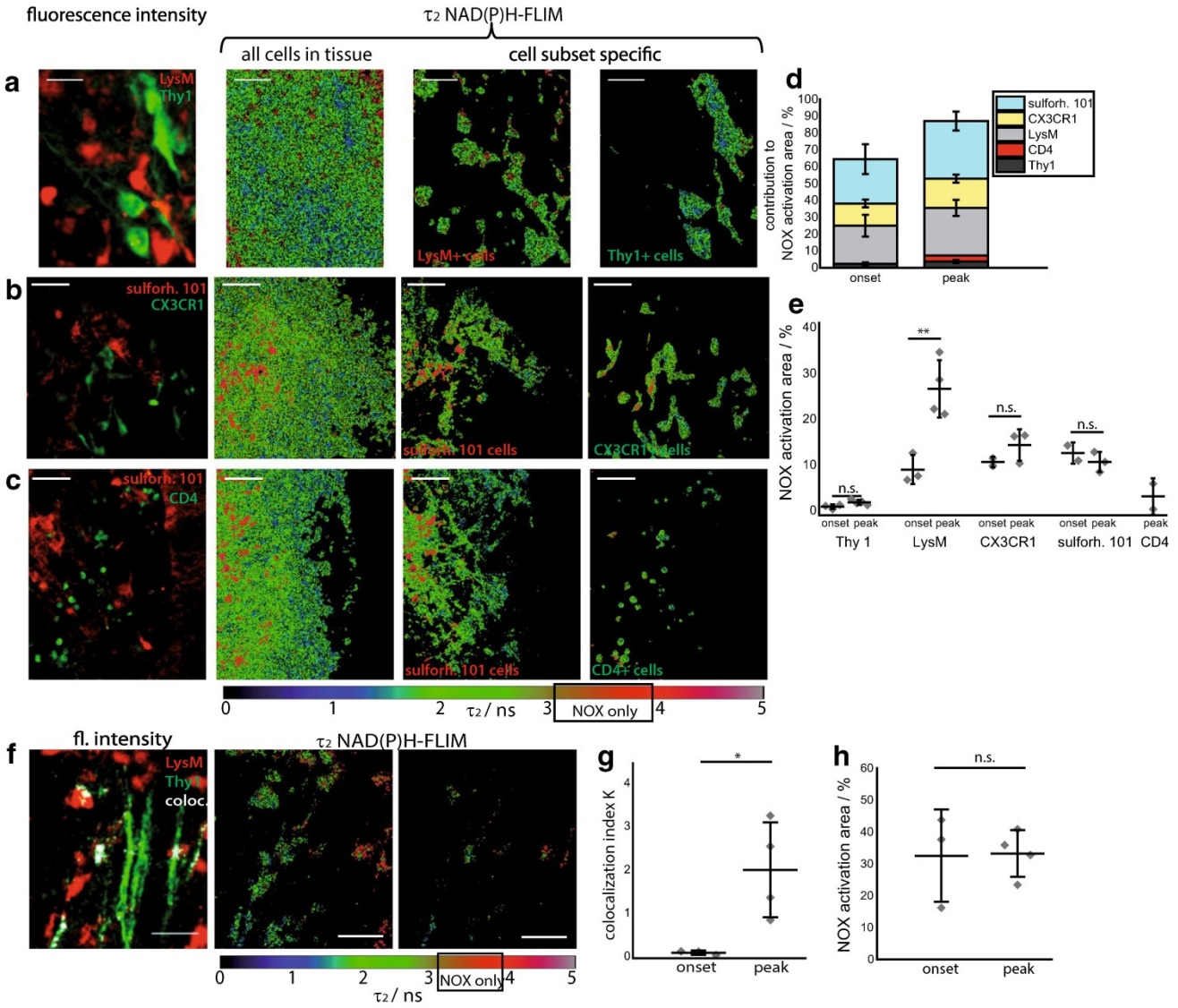

of EGCG, levels were even further reduced, almost to the levels of healthy controls: 5.8 ± 3.4 % in mice and 6.4 ± 1.2 % in RRMS patients (Fig. 5).

To understand the kinetics of NOX activation leading to oxidative stress during the course of the disease, we analyzed PBMCs of newly diagnosed (untreated) patients with CIS, untreated RRMS patients and differently treated SPMS patients. We observed little NOX activation in CIS patients (3.6 ± 1.2 %), and markedly elevated NOX activation in untreated RRMS patients (18.3 ± 2.5 %) and in treated SPMS patients (15.1 ± 3.2 %) (Fig. 5b). These data could be reproduced in mice, since at onset of disease $CD11b^+$ splenocytes showed almost normal NOX activation (5.0 ± 1.1 % %), while at peak of disease the values were similar to those measured in untreated RRMS patients (18.5 ± 3.5 %). Immunization with adjuvant only (CFA without MOG) did not increase NOX activation (3.0 ± 0.9 %) in $CD11b^+$ splenocytes. All values of NOX activation area represent mean values acquired over 30–120 cells per individual.

To address if EGCG counteracts a possible overexpression of NOX2 subunits in MS, rather than direct NOX2 overactivation, we performed qRT-PCR analysis of PBMCs from ECGC-treated and untreated patients. We did not detect any differences in the expression level of the gp91 (NOX2 subunit) in patients treated with GA and placebo as compared to treatment with GA and EGCG (Fig. 6e), indicating that the reduced activation of NOX2 in EGCG-treated patients was not caused by reduced gp91 gene expression. Rather, this observation could be explained by direct inhibition of NOX2 activation by EGCG, which is in accordance with the fact that EGCG competes with NADPH in binding to the NADPH-binding site of enzymes [6] including the NADPH oxidases (NOX enzymes). In

◀**Fig. 4** Cellular origin of NADPH oxidases activity in the CNS of EAE mice. **a** The fluorescence intensity image and the τ_2 NAD(P)H-FLIM map of whole tissue area was used to analyze the cellular origin of NOX activation signal in the CNS. Therefore, we performed an overlay of both images and analyzed the NAD(P)H-FLIM signal at the areas of the respective cell types. Exemplarily $LysM^+$ cells as well as $Thy1^+$ cells (neurons) in **(a)**, $CX_3CR_1^{+/-}$ EGFP—*green* or sulforhodamine 101—*red* (astrocytes) in **b** and $CD4^+$ YFP—*green* (T cells) or sulforhodamine 101—*red* (astrocytes) in **c** are shown in the brain stem of mice affected by EAE. All τ_2 NAD(P)H-FLIM images depict the normalized area of NOX activation in relation to the total cellular area in the respective cell subsets. *Scale bar* 30 µm (**a**) and 50 µm (**b**, **c**). Quantification of the contribution of LysM, Thy1, CX_3XR_1, $CD4^+$ and sulforhodamine 101-labeled cell subsets, respectively, to the total area of NOX enzymes activation within a lesion. $LysM^+$ phagocytes: 22.7 % at onset and 28.2 % at the peak of EAE, $CX_3CR_1^+$ cells: 13.1 % at onset and 17.4 % at the peak of EAE, astrocytes (sulforhodamine 101): is 26.2 and 37.0 %, $CD4^+$ cells: 3.6 % at peak disease, neurons ($Thy1^+$): 2.3 % at onset and 3.8 % at peak (**d**). To analyze the proportion of activated cells in one specific cell subset, we quantified the NOX enzymes activation area relative to the total area of the respective cell type at onset and peak of disease (**e**). The area of NOX activation within neurons ($Thy1^+$ cells in the *$LysM^+$tdRFP x CerTN L15* mice): onset 0.8 ± 0.5 % and peak 1.8 ± 0.4 %, $LysM^+$ cells onset 7.9 ± 2.3 %, and peak 26.4 ± 6.6 %, $CX_3CR_1^+$ cells: onset 10.6 ± 0.6 % and peak 14.4 ± 1.7 %, astrocytes (sulforhodamine 101): onset 11.7 ± 0.6 % and peak 9.8 ± 1.6 %, $CD4^+$ cells: peak 3.1 ± 2.0 %. Data from 2 EAE experiments in *$LysM^+$tdRFP x CerTN L15* mice, $n = 3$ onset, peak $n = 4$; 2 EAE experiments in *$CX_3XR_1^{+/-}$ EGFP* mice labeled with sulforhodamine 101, $n = 2$ onset and $n = 3$ peak; 1 EAE experiment in *$CD4^+$ YFP* mice labeled with sulforhodamine 101, peak $n = 2$ (**e**). *Left* fluorescence intensity image of brain stem lesion in EAE (Thy1 = *green*, LysM = *red*, colocalisation = *white*). τ_2 (enzyme-bound) NAD(P)H-FLIM image of $LysM^+$tdRFP cells in tissue (*middle*) and at the Thy1/LysM colocalisation area (*right*) depicts the normalized area of NOX enzymes activation in relation to total $LysM^+$ cellular area as well as the activation within the colocalisation area. *Scale bar* 30 µm (**f**). The normalized colocalisation index indicates the interaction level between $LysM^+$ and Thy1 cells, respectively, in onset and in peak of the disease, in the same experiments (**g**). Quantification of the mean NOX activation area of individual mice relative to the total area of LysM/Thy1 colocalisation at the onset ($n = 3$) and peak ($n = 4$) of disease, two independent EAE experiments (**h**). All images are acquired in 30–150 µm depth within the brain stem (z-step = 2 µm). For statistic evaluation in **d** we applied the ANOVA test, in **g** and **h** Mann–Whitney *U* tests (*$p < 0.05$, **$p < 0.01$, ***$p < 0.001$)

vitro data from our group using 100 µM EGCG yielded similar results, as they lead to an immediate shift with more free NAD(P)H with a shorter fluorescence lifetime (data not shown).

As NOX2 activity requires the fusion of the membrane-bound p22 and cytosolic p47 components, we examined the co-localization of p22 and p47 in human $CD11b^+$ PBMCs by imaging cytometry to confirm our FLIM data with an independent approach. The co-localization was quantified as the Bright Detail Similarity (BDS), which measures the correlation coefficient between the intensities in localized bright spots of radius 1 µm or less. In healthy donors, less than 0.1 % of $CD11b^+$ cells demonstrated co-localization of the p22 and p47 subunits, as indicated by a BDS >2, while RRMS patients had a markedly increased proportion of cells in which the two subunits co-localized, with 3.6 % of $CD11b^+$ cells having a BDS >2 (Fig. 6a–c). Using a DCF (Di-Chloridium Fluorescein) fluorescence-based ROS/RNS detection assay in serum, we measured a general trend towards lower ROS/RNS concentrations in GA-treated RRMS patients with EGCG co-therapy as compared to placebo (Fig. 6d). Consistent with MS pathology (with the brain as the target of inflammation) and the frequencies of overactivated cells in the blood as detected with imaging cytometry, the ROS/RNS are highly diluted in serum, and were not significantly different between the groups under investigation.

Discussion

To elucidate how oxidative stress causes neuronal degeneration and to clarify the mechanisms of anti-oxidant therapy, it is necessary to have a tool which allows real-time monitoring of functional changes at cellular and sub-cellular level. Applying this tool both within the central nervous system—where the damage takes place—and in the peripheral immune system demonstrates novel links between human disease and animal models, and offers unique functional insights into the systemic impact of MS.

In the present study, we monitored for the first time the functionality of NADPH oxidases catalyzing the production of ROS, which leads to oxidative stress in vivo. The fact that NOX enzymes are membrane-bound enzymes facilitates the identification of their cellular origins. Our intravital imaging and marker-free NAD(P)H-FLIM data demonstrate that NADPH oxidases are overactivated in astrocytes (sulforh101 labeled) during neuroinflammation, in addition to the known contributors, $LysM^+$ and $CX_3CR_1^+$ phagocytes, previously reported and recently corroborated in bone marrow chimeric mice deficient for NRROS, a negative regulator of ROS [38, 42]. Our intravital data regarding the role of astrocytes in chronic neuroinflammation are supported by histological studies showing that Noxo1 is expressed in $GFAP^+$ cells, and that negative p22 immunostaining [45] in astrocytes does not exclude a NOX2-independent functional NADPH oxidases activation in vivo [54]. Additionally, we showed that NOX enzymes activation was spatially associated with lesion sites in EAE, and correlated with locations of neuronal dysfunction. This finding is consistent with the report that mice with knockout of the common subunit of NOX enzymes ($p47^{-/-}$ mice) are more resistant to EAE [57] supporting the idea that NOX2, the phagocytic isotype, is not the only member of the NOX family that may contribute to excessive ROS production in chronic neuroinflammation. In line with this, mice lacking only NOX2 ($gp91^{-/-}$) develop only a slightly milder form of EAE [29] and expression levels of NOX enzyme subunits other than NOX2

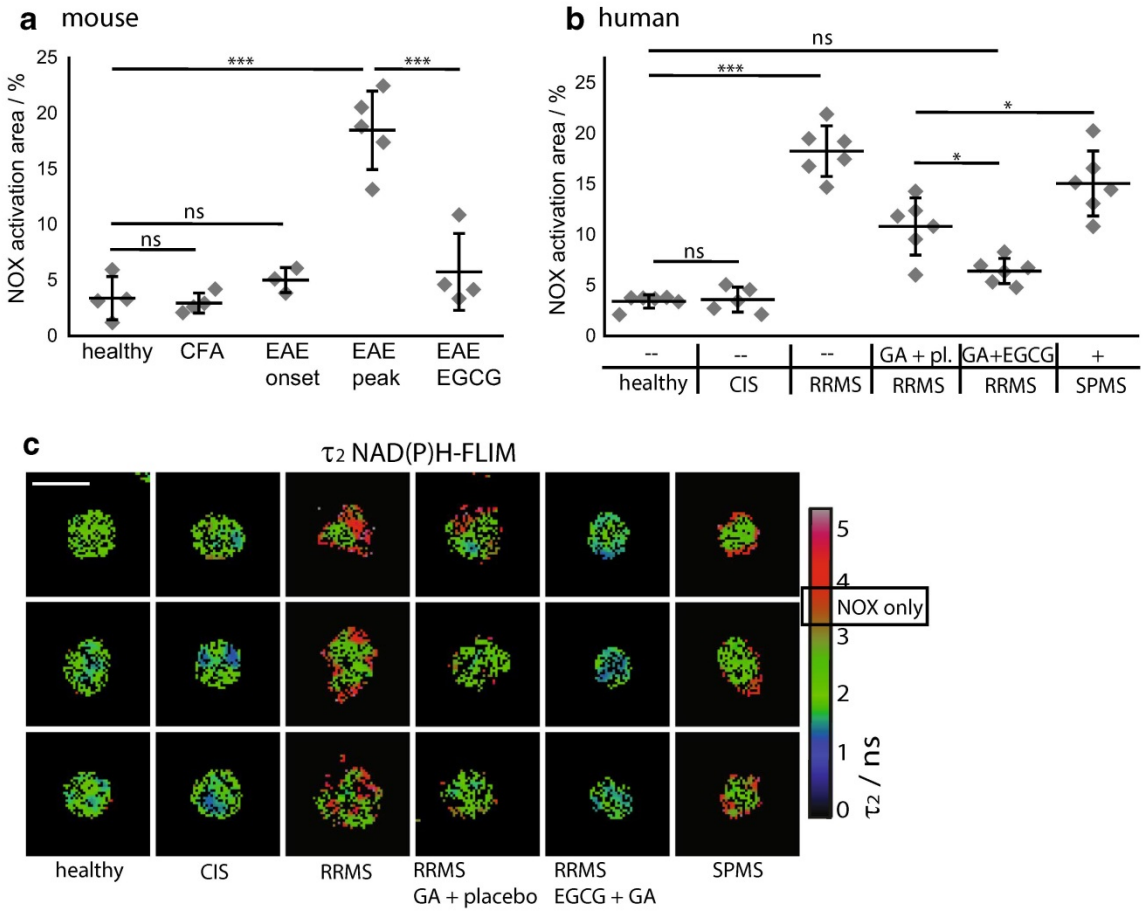

Fig. 5 NOX activation in murine and human peripheral CD11b$^+$ cells during chronic neuroinflammation as compared to treatment with EGCG. **a** Quantification of mean normalized area of NOX activation as measured from τ_2 (enzyme-bound) NAD(P)H fluorescence lifetime images of MACS-purified splenic CD11b$^+$ monocytes from healthy controls ($n = 4$), from mice immunized only with Freund's Complete Adjuvant (CFA, $n = 4$) and from mice with EAE—at onset of disease ($n = 3$), at peak of disease ($n = 5$) or treated with EGCG ($n = 4$) encompassing two to four independent EAE experiments. **b** Quantification of mean normalized area of NOX activation of MACS-enriched blood CD11b$^+$ human monocytes from age- and gender-matched healthy controls ($n = 6$), patients with clinically isolated syndrome (CIS, $n = 5$), untreated RRMS patients ($n = 6$), RRMS patients treated either with glatiramer acetate (GA) and placebo ($n = 6$) or with glatiramer acetate and EGCG ($n = 6$) as well as SPMS patients with their regular MS-related therapy ($n = 6$). **a**, **b** Data points are mean values of at least 50 cells from one individual, for the statistic evaluation we applied ANOVA tests (*$p < 0.05$, **$p < 0.01$, ***$p < 0.001$). **c** Representative color-encoded τ_2 NAD(P)H fluorescence lifetime images of MACS-enriched blood CD11b$^+$ human monocytes

were elevated within active MS lesions [13]. One additional candidate is NOX1, which was reported to be neurotoxic in microglia [8]. Importantly, our NAD(P)H-FLIM technique to detect the catalysis of oxidative stress does not discriminate between NOX isotypes. Rather, it detects their increased activation as compared to other NAD(P)H-dependent enzymes responsible for basic cellular processes that are present in the same observation volume ($0.4 \times 0.4 \times 1.5\ \mu m^3$). Therefore, the hallmark of our technique is its capacity to monitor excessive NOX enzyme function as a reliable indicator of oxidative stress, rather than dissecting the activation of specific NOX isotypes.

NADPH oxidases activation was not restricted to a specific cell type, and was not preferentially found co-localized with the major compartments of the immune system (macrophages/activated microglia) and of the CNS (neurons), suggesting a predominant contribution of locally acting soluble factors like TNF-α or glutamate [15, 62]. Glutamate is not only an excitotoxic factor but was also shown to induce NOX activation. Supporting this interpretation, we found that local treatment with glutamate caused a significant increase of the NOX enzymes activation area as revealed by intravital NAD(P)H-FLIM in the brain stem of healthy mice (Suppl. Fig. 5).

As macrophages/microglia are two of the main producers of ROS in EAE, it was unexpected that only up to 50 % of the area of macrophages/microglia (LysM$^+$tdRFP cells and $CX_3CR_1^{+/-}$EGFP cells) showed activation of NOX

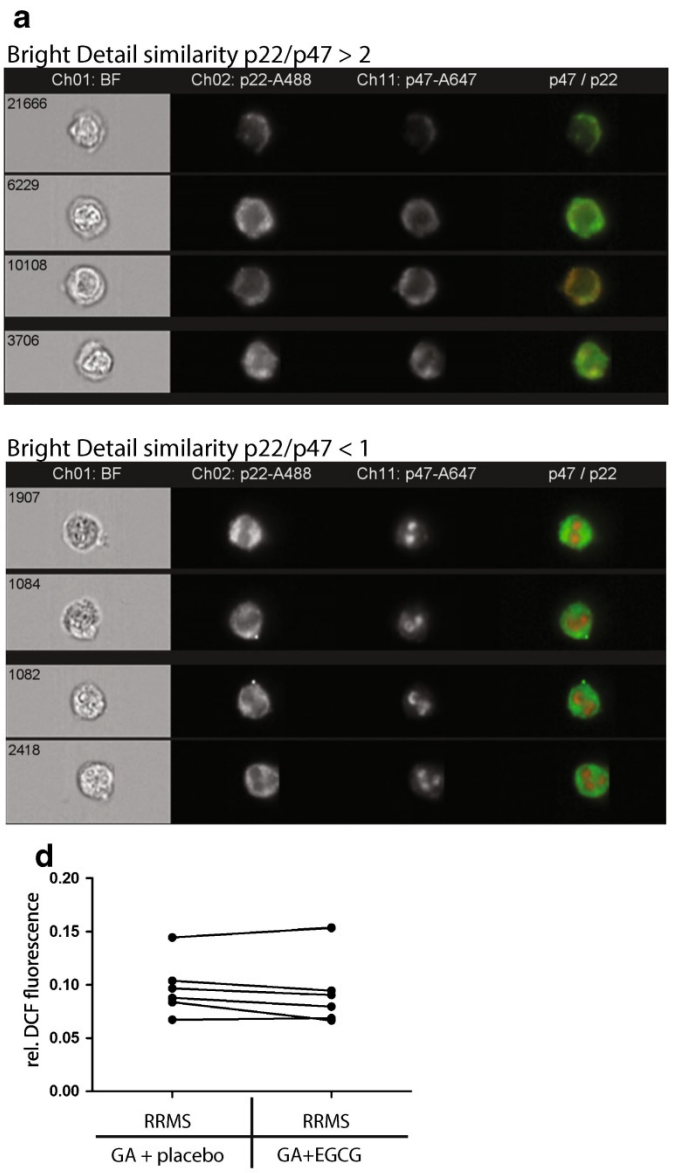

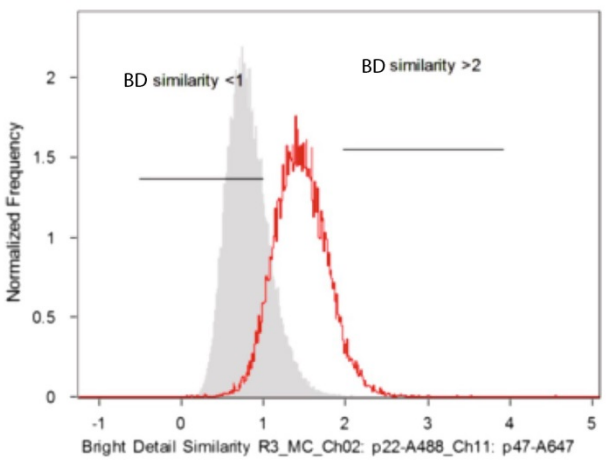

c

	healthy controls (n = 2)		untreated RRMS (n = 2)	
	cell count	percentage of CD11b+	cell count	percentage of CD11b+
CD11b+	64915	100%	50278	100%
BD similarity p22/p47 > 2	56	0.09%	1810	3.6%

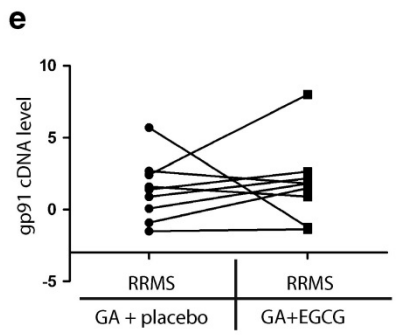

Fig. 6 NOX subunits expression levels and co-localization in human peripheral CD11b$^+$ cells as well as ROS detection in serum during chronic neuroinflammation. **a** Representative images of cells, generated by imaging flow cytometry immunostained for CD11b, p22 (membrane-bound NOX subunit) and p47 (cytosolic NOX subunit). Cells shown are gated on CD11b (not shown). The upper panel depicts cells with high bright detail similarity (>2) between p22 and p47 patterns (activated NOX), whereas the lower panel shows cells with low bright detail similarity (<1). **b** Less CD11b$^+$ cells of a healthy control show high similarity (>2) between p22 and p47 as compared to an untreated RRMS patient. **c** The table depicts corresponding cell numbers and percentages from two healthy controls and two untreated RRMS patients showing that CD11b$^+$ cells with high similarity between p22 and p47, indicating activated NOX, are at least 20× more frequent in untreated RRMS patients than in healthy controls. **d** Results of DCF fluorescence-based ROS/RNS detection assay in serum of patients show a general trend of lower ROS/RNS production in glatiramer acetate (GA) treated RRMS patients after EGCG complementary therapy as compared to placebo. **e** Analyzed gp91 cDNA levels of PBMCs with qRT-PCR showed no difference in expression levels in patients pre- or post-treatment with EGCG

enzymes in vivo (Fig. 4e). This is consistent with the findings that the reactive oxidative burst is counter-regulated in MS by myelin-loaded macrophages up-regulating antioxidant enzymes [14, 17, 58]. The toxic role of excessive ROS production in MS pathogenesis has been proposed to be related to multiple mechanisms, including enhanced blood–brain barrier transmigration [56], oligodendrocyte damage, and mitochondrial damage leading to further ROS production. Here, we provide evidence for an additional mechanism of NOX enzymes-mediated pathogenesis in MS: direct induction of neuronal dysfunction. We demonstrated in vivo that NOX enzymes activity leading

to excessive ROS production was spatially correlated with pathologically increased neuronal calcium—a reliable indicator of neuronal dysfunction at lesion sites [7, 48].

The activation of astrocytes towards oxidative stress generation in chronic neuroinflammation supports the hypothesis that these cells are partially responsible for the accumulated neuronal dysfunction and damage over the course of the disease. In the later phases of the disease, activated astrocytes and microglia may continue to enhance neuronal loss even in the absence of overt immune infiltration of the CNS. Thus, these cells may become a major target of therapy, especially in the progressive phase of the disease. We also employed our NAD(P)H-FLIM technique, under in vitro conditions, to monitor NOX enzymes activation in peripheral cells. The elevated NOX activation in monocytes from the periphery of EAE mice and of MS patients at various stages of the disease strengthens the view that both MS and EAE have a complex systemic dimension. Increased NOX activation in peripheral monocytes is not specific for MS, as we could also see moderately elevated NOX activation in individuals with common cold (data not shown). However, we saw a significant increase of NOX activation with disease progression, similar to our observation in the target organ, the CNS. The time-dependent increase in MS patients from no overactivation at the beginning of the disease (CIS patients and EAE onset) to elevated NOX activity in RRMS and SPMS patients' PBMCs we observed, in conjunction with data from other groups showing overexpression of NOX subunits in the CNS tissue of progressive MS patients at lesion sites [13] supports the hypothesis that during the course of the disease the immune system (and possibly also CNS components like astrocytes and microglia) develops an "oxidative stress memory". Our findings are furthermore in accordance with data showing that in the chronic phase of the disease oxidized DNA, damaged lipids, and proteins are present in PBMCs of MS patients [21], supporting the proposition that excessive ROS plays a major role in the progressive phase of the disease.

Collectively, these results point to new treatment strategies aiming to reduce oxidative stress in MS. EGCG, the major polyphenolic compound of the green tea plant has been investigated under numerous conditions. Although the molecular mechanisms of its actions are not fully understood [33], there is experimental data pointing to the inhibition of ROS production through EGCG in vitro [63]. Empirically, we showed that EGCG is neuroprotective in EAE, it is known to influence T cell and neuronal function [2, 19, 61] and clinical trials investigating the effects of EGCG (NCT00525668, NCT00799890 and NCT01417312) are ongoing.

In the current study, we demonstrated a direct anti-oxidative mechanism of EGCG on PBMCs of MS patients. Oral treatment with EGCG completely counteracted the chronic NOX overactivation in MS patients, consistent with a higher enzymatic activity, as we could not detect overexpression of NOX2 subunit gp91 by qRT-PCR. Since it is known that EGCG inhibits the binding of NADPH to enzymes within the cell, we observed the mechanism of blocking NADPH binding to NADPH oxidases.

Beside insights into the cellular sources of oxidative stress in EAE and MS, in the CNS and in the periphery, this work demonstrates the unique versatility of intravital NAD(P)H-FLIM as a marker-free method to investigate mechanisms of oxidative stress in inflammatory pathologies, underscoring its intriguing potential for biomedicine as well as clinical research, in a more general context.

Acknowledgments We thank O. Griesbeck for providing the *CerTN L15* transgenic mice, H.J. Fehling for the *Rosa26.tdRFP* transgenic mice and K. Westendorf for providing the *CD4*$^{+}$*.YFP* mouse. We would like to thank E. Gratton and M. Digman for kindly receiving J.P. in the frame of a lab exchange at the University Irvine, CA and for fruitful discussions concerning the detection of oxidative stress by FLIM. We kindly thank R. Günther, N. Asselborn and P. Mex for excellent technical assistance. We are highly grateful to Frank Heppner who provided insight and expertise that greatly assisted the research. Funding: We acknowledge the Deutsche Forschungsgemeinschaft under grant NI 1167/2-1, NI 1167/3-1, NI 1167/4-1 as well as the TRR130 to R.N., H.R. and A.E.H. and the Berlin-Brandenburg School for Regenerative Therapies GSC 203 for H.R. for financial support. This work was partially funded through DFG Exc 257 to F.P. and A.E.H. and TPC4 in FOR 1336 to Jo. P. We declare no competing financial interests.

Open Access This article is distributed under the terms of the Creative Commons Attribution 4.0 International License (http://creativecommons.org/licenses/by/4.0/), which permits unrestricted use, distribution, and reproduction in any medium, provided you give appropriate credit to the original author(s) and the source, provide a link to the Creative Commons license, and indicate if changes were made.

References

1. Agronskaia AV, Tertoolen L, Gerritsen HC (2004) Fast fluorescence lifetime imaging of calcium in living cells. J Biomed Optics 9:1230–1237. doi:10.1117/1.1806472
2. Aktas O, Prozorovski T, Smorodchenko A, Savaskan NE, Lauster R, Kloetzel PM, Infante-Duarte C, Brocke S, Zipp F (2004) Green tea epigallocatechin-3-gallate mediates T cellular NF-kappa B inhibition and exerts neuroprotection in autoimmune encephalomyelitis. J Immunol 173:5794–5800
3. Appaix F, Girod S, Boisseau S, Romer J, Vial JC, Albrieux M, Maurin M, Depaulis A, Guillemain I, van der Sanden B (2012) Specific in vivo staining of astrocytes in the whole brain after intravenous injection of sulforhodamine dyes. PLoS One 7:e35169. doi:10.1371/journal.pone.0035169
4. Balu M, Mazhar A, Hayakawa CK, Mittal R, Krasieva TB, Konig K, Venugopalan V, Tromberg BJ (2013) In vivo multiphoton NADH fluorescence reveals depth-dependent keratinocyte metabolism in human skin. Biophys J 104:258–267. doi:10.1016/j.bpj.2012.11.3809

5. Bedard K, Krause K-H (2007) The NOX Family of ROS-generating NADPH oxidases: physiology and pathophysiology. Physiol Rev 87:245–313. doi:10.1152/physrev.00044.2005
6. Blacker TS, Mann ZF, Gale JE, Ziegler M, Bain AJ, Szabadkai G, Duchen MR (2014) Separating NADH and NADPH fluorescence in live cells and tissues using FLIM. Nat Commun 5:3936. doi:10.1038/ncomms4936
7. Breckwoldt MO, Pfister FM, Bradley PM, Marinkovic P, Williams PR, Brill MS, Plomer B, Schmalz A, St Clair DK, Naumann R et al (2014) Multiparametric optical analysis of mitochondrial redox signals during neuronal physiology and pathology in vivo. Nat Med 20:555–560. doi:10.1038/nm.3520
8. Cheret C, Gervais A, Lelli A, Colin C, Amar L, Ravassard P, Mallet J, Cumano A, Krause KH, Mallat M (2008) Neurotoxic activation of microglia is promoted by a nox1-dependent NADPH oxidase. J Neurosci 28:12039–12051. doi:10.1523/JNEUROSCI.3568-08.2008
9. Choi BY, Kim JH, Kho AR, Kim IY, Lee SH, Lee BE, Choi E, Sohn M, Stevenson M, Chung TN et al (2015) Inhibition of NADPH oxidase activation reduces EAE-induced white matter damage in mice. J Neuroinflamm 12:104. doi:10.1186/s12974-015-0325-5
10. Clausen BE, Burkhardt C, Reith W, Renkawitz R, Forster I (1999) Conditional gene targeting in macrophages and granulocytes using LysMcre mice. Transgenic Res 8:265–277
11. Cooney SJ, Bermudez-Sabogal SL, Byrnes KR (2013) Cellular and temporal expression of NADPH oxidase (NOX) isotypes after brain injury. J Neuroinflamm 10:155. doi:10.1186/1742-2094-10-155
12. Elson D, Requejo-Isidro J, Munro I, Reavell F, Siegel J, Suhling K, Tadrous P, Benninger R, Lanigan P, McGinty J et al (2004) Time-domain fluorescence lifetime imaging applied to biological tissue. Photochem Photobiol Sci 3:795–801. doi:10.1039/b316456j
13. Fischer MT, Sharma R, Lim JL, Haider L, Frischer JM, Drexhage J, Mahad D, Bradl M, van Horssen J, Lassmann H (2012) NADPH oxidase expression in active multiple sclerosis lesions in relation to oxidative tissue damage and mitochondrial injury. Brain 135:886–899. doi:10.1093/brain/aws012
14. Frischer JM, Bramow S, Dal Bianco A, Lucchinetti CF, Rauschka H, Schmidbauer M, Laursen H, Sorensen PS, Lassmann H (2009) The relation between inflammation and neurodegeneration in multiple sclerosis brains. Brain 132:1175–1189
15. Gilgun-Sherki Y, Melamed E, Offen D (2004) The role of oxidative stress in the pathogenesis of multiple sclerosis: the need for effective antioxidant therapy. J Neurol 251:261–268. doi:10.1007/s00415-004-0348-9
16. Grass D, Pawlowski PG, Hirrlinger J, Papadopoulos N, Richter DW, Kirchhoff F, Hulsmann S (2004) Diversity of functional astroglial properties in the respiratory network. J Neurosci 24:1358–1365. doi:10.1523/JNEUROSCI.4022-03.2004
17. Haider L, Fischer MT, Frischer JM, Bauer J, Höftberger R, Botond G, Esterbauer H, Binder CJ, Witztum JL, Lassmann H (2011) Oxidative damage in multiple sclerosis lesions. Brain 134:1914–1924. doi:10.1093/brain/awr128
18. Heim N, Garaschuk O, Friedrich MW, Mank M, Milos RI, Kovalchuk Y, Konnerth A, Griesbeck O (2007) Improved calcium imaging in transgenic mice expressing a troponin C-based biosensor. Nat Methods 4:127–129
19. Herges K, Millward JM, Hentschel N, Infante-Duarte C, Aktas O, Zipp F (2011) Neuroprotective effect of combination therapy of glatiramer acetate and epigallocatechin-3-gallate in neuroinflammation. PLoS One 6:e25456. doi:10.1371/journal.pone.0025456
20. Herz J, Siffrin V, Hauser AE, Brandt AU, Leuenberger T, Radbruch H, Zipp F, Niesner RA (2010) Expanding two-photon intravital microscopy to the infrared by means of optical parametric oscillator. Biophys J 98:715–723
21. Hunter MI, Nlemadim BC, Davidson DL (1985) Lipid peroxidation products and antioxidant proteins in plasma and cerebrospinal fluid from multiple sclerosis patients. Neurochem Res 10:1645–1652
22. Janssen A, Fiebiger S, Bros H, Hertwig L, Romero-Suarez S, Hamann I, Chanvillard C, Bellmann-Strobl J, Paul F, Millward JM et al (2015) Treatment of chronic experimental autoimmune encephalomyelitis with epigallocatechin-3-gallate and glatiramer acetate alters expression of heme-oxygenase-1. PLoS One 10:e0130251. doi:10.1371/journal.pone.0130251
23. Jung S, Aliberti J, Graemmel P, Sunshine MJ, Kreutzberg GW, Sher A, Littman DR (2000) Analysis of fractalkine receptor CX(3)CR1 function by targeted deletion and green fluorescent protein reporter gene insertion. Mol Cell Biol 20:4106–4114
24. Konig K (2000) Multiphoton microscopy in life sciences. J Microsc 200:83–104
25. Kumar S, Alibhai D, Margineanu A, Laine R, Kennedy G, McGinty J, Warren S, Kelly D, Alexandrov Y, Munro I et al (2011) FLIM FRET technology for drug discovery: automated multiwell-plate high-content analysis, multiplexed readouts and application in situ. Chem Phys Chem 12:609–626. doi:10.1002/cphc.201000874
26. Lakowicz JR, Szmacinski H, Nowaczyk K, Johnson ML (1992) Fluorescence lifetime imaging of free and protein-bound NADH. Proc Natl Acad Sci USA 89:1271–1275
27. Lassmann H, Bruck W, Lucchinetti C (2001) Heterogeneity of multiple sclerosis pathogenesis: implications for diagnosis and therapy. Trends Mol Med 7:115–121
28. Lee PP, Fitzpatrick DR, Beard C, Jessup HK, Lehar S, Makar KW, Perez-Melgosa M, Sweetser MT, Schlissel MS, Nguyen S et al (2001) A critical role for Dnmt1 and DNA methylation in T cell development, function, and survival. Immunity 15:763–774
29. Li S, Vana AC, Ribeiro R, Zhang Y (2011) Distinct role of nitric oxide and peroxynitrite in mediating oligodendrocyte toxicity in culture and in experimental autoimmune encephalomyelitis. Neuroscience 184:107–119. doi:10.1016/j.neuroscience.2011.04.007
30. Li Z, Tian F, Shao Z, Shen X, Qi X, Li H, Wang Z, Chen G (2015) Expression and clinical significance of non-phagocytic cell oxidase 2 and 4 after human traumatic brain injury. Neurol Sci Off J Ital Neurol Soc Ital Soc Clin Neurophysiol 36:61–71. doi:10.1007/s10072-014-1909-z
31. Lu F, Selak M, O'Connor J, Croul S, Lorenzana C, Butunoi C, Kalman B (2000) Oxidative damage to mitochondrial DNA and activity of mitochondrial enzymes in chronic active lesions of multiple sclerosis. J Neurol Sci 177:95–103
32. Luche H, Weber O, Nageswara Rao T, Blum C, Fehling H (2007) Faithful activation of an extra-bright red fluorescent protein in "knock-in" Cre-reporter mice ideally suited for lineage tracing studies. Eur J Immunol 37:43–53
33. Mahler A, Mandel S, Lorenz M, Ruegg U, Wanker EE, Boschmann M, Paul F (2013) Epigallocatechin-3-gallate: a useful, effective and safe clinical approach for targeted prevention and individualised treatment of neurological diseases? EPMA J 4:5. doi:10.1186/1878-5085-4-5
34. Miller D, Barkhof F, Montalban X, Thompson A, Filippi M (2005) Clinically isolated syndromes suggestive of multiple sclerosis, part I: natural history, pathogenesis, diagnosis, and prognosis. Lancet Neurol 4:281–288. doi:10.1016/S1474-4422(05)70071-5

35. Murata S, Herman P, Lakowicz JR (2001) Texture analysis of fluorescence lifetime images of nuclear DNA with effect of fluorescence resonance energy transfer. Cytometry 43:94–100
36. Nayernia Z, Jaquet V, Krause KH (2014) New insights on NOX enzymes in the central nervous system. Antioxid Redox Signal 20:2815–2837. doi:10.1089/ars.2013.5703
37. Niesner R, Narang P, Spiecker H, Andresen V, Gericke KH, Gunzer M (2008) Selective detection of NADPH oxidase in polymorphonuclear cells by means of NAD(P)H-based fluorescence lifetime imaging. J Biophys 2008:602639. doi:10.1155/2008/602639
38. Nikic I, Merkler D, Sorbara C, Brinkoetter M, Kreutzfeldt M, Bareyre FM, Bruck W, Bishop D, Misgeld T, Kerschensteiner M (2011) A reversible form of axon damage in experimental autoimmune encephalomyelitis and multiple sclerosis. Nat Med. 17:495–499. http://www.nature.com/nm/journal/v17/n4/abs/nm.2324.html#supplementary-information
39. Nimmerjahn A, Helmchen F (2012) In vivo labeling of cortical astrocytes with sulforhodamine 101 (SR101). Cold Spring Harbor Protoc 2012:326–334. doi:10.1101/pdb.prot068155
40. Nimmerjahn A, Kirchhoff F, Kerr JN, Helmchen F (2004) Sulforhodamine 101 as a specific marker of astroglia in the neocortex in vivo. Nat Methods 1:31–37. doi:10.1038/nmeth706
41. Noseworthy JH, Lucchinetti C, Rodriguez M, Weinshenker BG (2000) Multiple sclerosis. N Engl J Med 343:938–952. doi:10.1056/NEJM200009283431307
42. Noubade R, Wong K, Ota N, Rutz S, Eidenschenk C, Valdez PA, Ding J, Peng I, Sebrell A, Caplazi P et al (2014) NRROS negatively regulates reactive oxygen species during host defence and autoimmunity. Nature 509:235–239. doi:10.1038/nature13152
43. Reinehr R, Gorg B, Becker S, Qvartskhava N, Bidmon HJ, Selbach O, Haas HL, Schliess F, Haussinger D (2007) Hypoosmotic swelling and ammonia increase oxidative stress by NADPH oxidase in cultured astrocytes and vital brain slices. Glia 55:758–771. doi:10.1002/glia.20504
44. Rinnenthal JL, Bornchen C, Radbruch H, Andresen V, Mossakowski A, Siffrin V, Seelemann T, Spiecker H, Moll I, Herz J et al (2013) Parallelized TCSPC for dynamic intravital fluorescence lifetime imaging: quantifying neuronal dysfunction in neuroinflammation. PLoS One 8:e60100. doi:10.1371/journal.pone.0060100
45. Schuh C, Wimmer I, Hametner S, Haider L, Van Dam AM, Liblau RS, Smith KJ, Probert L, Binder CJ, Bauer J et al (2014) Oxidative tissue injury in multiple sclerosis is only partly reflected in experimental disease models. Acta Neuropathol 128:247–266. doi:10.1007/s00401-014-1263-5
46. Shin ES, Park J, Shin JM, Cho D, Cho SY, Shin DW, Ham M, Kim JB, Lee TR (2008) Catechin gallates are NADP+-competitive inhibitors of glucose-6-phosphate dehydrogenase and other enzymes that employ NADP+ as a coenzyme. Bioorg Med Chem 16:3580–3586. doi:10.1016/j.bmc.2008.02.030
47. Siffrin V, Brandt AU, Radbruch H, Herz J, Boldakowa N, Leuenberger T, Werr J, Hahner A, Schulze-Topphoff U, Nitsch R et al (2009) Differential immune cell dynamics in the CNS cause CD4 + T cell compartmentalization. Brain 132:1247–1258 **(pii: awn354)**
48. Siffrin V, Radbruch H, Glumm R, Niesner R, Paterka M, Herz J, Leuenberger T, Lehmann SM, Luenstedt S, Rinnenthal JL et al (2010) In vivo imaging of partially reversible th17 cell-induced neuronal dysfunction in the course of encephalomyelitis. Immunity 33:424–436
49. Sorce S, Krause KH (2009) NOX enzymes in the central nervous system: from signaling to disease. Antioxid Redox Signal 11:2481–2504. doi:10.1089/ARS.2009.2578
50. Srinivas S, Watanabe T, Lin CS, William CM, Tanabe Y, Jessell TM, Costantini F (2001) Cre reporter strains produced by targeted insertion of EYFP and ECFP into the ROSA26 locus. BMC Dev Biol 1:4
51. Stringari C, Edwards RA, Pate KT, Waterman ML, Donovan PJ, Gratton E (2012) Metabolic trajectory of cellular differentiation in small intestine by Phasor Fluorescence Lifetime Microscopy of NADH. Sci Rep 2:568. doi:10.1038/srep00568
52. Stringari C, Nourse JL, Flanagan LA, Gratton E (2012) Phasor fluorescence lifetime microscopy of free and protein-bound NADH reveals neural stem cell differentiation potential. PLoS One 7:e48014. doi:10.1371/journal.pone.0048014
53. Suhling K, Levitt JA, Chung PH, Kuimova MK, Yahioglu G (2012) Fluorescence lifetime imaging of molecular rotors in living cells. J Vis Exp JoVE. doi:10.3791/2925
54. Sumimoto H, Miyano K, Takeya R (2005) Molecular composition and regulation of the Nox family NAD(P)H oxidases. Biochem Biophys Res Commun 338:677–686. doi:10.1016/j.bbrc.2005.08.210
55. van der Goes A, Brouwer J, Hoekstra K, Roos D, van den Berg TK, Dijkstra CD (1998) Reactive oxygen species are required for the phagocytosis of myelin by macrophages. J Neuroimmunol 92:67–75
56. Van der Goes A, Wouters D, Van Der Pol SM, Huizinga R, Ronken E, Adamson P, Greenwood J, Dijkstra CD, De Vries HE (2001) Reactive oxygen species enhance the migration of monocytes across the blood-brain barrier in vitro. FASEB J Off Publ Fed Am Soc Exp Biol 15:1852–1854
57. van der Veen RC, Dietlin TA, Hofman FM, Pen L, Segal BH, Holland SM (2000) Superoxide prevents nitric oxide-mediated suppression of helper T lymphocytes: decreased autoimmune encephalomyelitis in nicotinamide adenine dinucleotide phosphate oxidase knockout mice. J Immunol 164:5177–5183
58. van Horssen J, Schreibelt G, Drexhage J, Hazes T, Dijkstra CD, van der Valk P, de Vries HE (2008) Severe oxidative damage in multiple sclerosis lesions coincides with enhanced antioxidant enzyme expression. Free Radic Biol Med 45:1729–1737. doi:10.1016/j.freeradbiomed.2008.09.023
59. van Horssen J, Singh S, van der Pol S, Kipp M, Lim JL, Peferoen L, Gerritsen W, Kooi EJ, Witte ME, Geurts JJ et al (2012) Clusters of activated microglia in normal-appearing white matter show signs of innate immune activation. J Neuroinflamm 9:156. doi:10.1186/1742-2094-9-156
60. Vladimirova O, Lu FM, Shawver L, Kalman B (1999) The activation of protein kinase C induces higher production of reactive oxygen species by mononuclear cells in patients with multiple sclerosis than in controls. Inflamm Res Off J Eur Histamine Res Soc [et al] 48:412–416
61. Wang J, Ren Z, Xu Y, Xiao S, Meydani SN, Wu D (2012) Epigallocatechin-3-gallate ameliorates experimental autoimmune encephalomyelitis by altering balance among CD4+ T-cell subsets. Am J Pathol 180:221–234. doi:10.1016/j.ajpath.2011.09.007
62. Werner P, Pitt D, Raine CS (2001) Multiple sclerosis: altered glutamate homeostasis in lesions correlates with oligodendrocyte and axonal damage. Ann Neurol 50:169–180
63. Yin S-T, Tang M-L, Su L, Chen L, Hu P, Wang H-L, Wang M, Ruan D-Y (2008) Effects of epigallocatechin-3-gallate on lead-induced oxidative damage. Toxicology 249:45–54. doi:10.1016/j.tox.2008.04.006

LEBENSLAUF

Mein Lebenslauf wird aus datenschutzrechtlichen Gründen in der elektronischen Version meiner Arbeit nicht veröffentlicht.

KOMPLETTE PUBLIKATIONSLISTE

„*In vivo* imaging of lymphocytes in the CNS reveals different behaviour of naïve T cells in health and autoimmunity“

Josephine Herz, Magdalena Paterka, Raluca A Niesner, Alexander U Brandt, Volker Siffrin, Tina Leuenberger, Jerome Birkenstock, **Agata Mossakowski**, Robert Glumm, Frauke Zipp und Helena Radbruch. Journal of Neuroinflammation, 2011. Impact Factor 5.41

“Parallelized TCSPC for Dynamic Intravital Fluorescence Lifetime Imaging: Quantifying Neuronal Dysfunction in Neuroinflammation”

Jan Leo Rinnenthal, Christian Börnchen, Helena Radbruch, Volker Andresen, **Agata Mossakowski,** Volker Siffrin, Thomas Seelemann, Heinrich Spiecker, Ingrid Moll, Josephine Herz, Anja E. Hauser, Frauke Zipp, Martin J. Behne und Raluca Niesner. PLOS one, 2013.
Impact Factor 3.23

„Tracking CNS and systemic sources of oxidative stress during the course of chronic neuroinflammation“

Agata A. Mossakowski, Julian Pohlan, Daniel Bremer, Randall Lindquist, Jason M. Millward, Markus Bock, Karolin Pollok, Ronja Mothes, Leonard Viohl, Moritz Radbruch, Jenny Gerhard, Judith Bellmann-Strobl, Janina Behrens, Carmen Infante-Duarte, Anja Mähler, Michael Boschmann, Jan Leo Rinnenthal, Martina Füchtemeier, Josephine Herz, Florence C. Pache, Markus Bardua, Josef Priller, Anja E. Hauser, Friedemann Paul, Raluca Niesner, Helena Radbruch. Acta Neuropathologica, 2015. Impact Factor 10.76

DANKSAGUNG

An allererster Stelle danke ich meiner wundervollen Betreuerin, Frau Dr. Helena Radbruch. Liebe Helena, seit unserer ersten Begegnung, in der Du alle meine bisherigen Pläne mit Deiner Begeisterung und Deinem wissenschaftlichen Enthusiasmus über den Haufen geworfen hast, bist Du mein größtes Vorbild. Ich bin so dankbar, damals meinem Bauchgefühl und dieser vor Ideen sprudelnden Frau gefolgt zu sein, obwohl ich mir noch überhaupt nichts unter Zweiphotonenmikroskopie vorstellen konnte. Ich danke Dir für Deine leidenschaftliche Unterstützung in allen Lebenslagen, Deine klugen Ratschläge und Deinen unerschütterlichen, heiteren Drang nach vorn. Du lebst gute und faire Wissenschaft vor, und ich bin unendlich froh, von Dir in diese Welt eingeführt worden zu sein. Genauso danken möchte ich Frau Dr. Raluca Niesner, die mich und diese Arbeit in den letzten Jahren eng und liebevoll begleitet hat. Liebe Raluca, für Deine Integrität, Deine Genialität und Deine Offenheit bewundere ich Dich über alle Maßen. Es macht unheimlich viel Spaß, mit Dir zusammen zu arbeiten und ich hoffe, dass ich diesen Spaß noch lange genießen kann! (Außerdem kenne ich sonst niemanden, der durch das bloße Betreten eines Raumes das darin stehende Mikroskop zum Laufen bringen kann. Den Trick musst Du mir mal verraten.) Auch Frau Prof. Dr. Anja Hauser hat mich über die letzten Jahre gestützt und vorwärts gebracht. Liebe Anja, danke für Deine stets offene Tür und Deinen Blick fürs Wesentliche. Du hast immer die richtigen Fragen gestellt und die entscheidenden Hinweise gegeben. Ich danke von Herzen den AGs Niesner und Hauser - Julian, David, Asylkhan, Laura, Sandra, Jannike, Caro, Karo, Randy, Leo, Zoltan, Florence, Peggy und Robert, für Eure Freundschaft, Eure Ideen, Eure helfenden Hände und Köpfe im Labor und für die Abende auf dem Dach. Herrn Prof. Dr. Friedemann Paul danke ich aufrichtig für den Rückhalt von der ersten Minute an. Lieber Friedemann, dass Du sofort eine Eingebung hattest und mich Helena vorgestellt hast, ist einer der größten Glücksgriffe meines Lebens. Meinem Doktorvater Herrn Prof. Dr. Josef Priller und seiner AG danke ich für ihre Unterstützung und das auf den Weg bringen dieses Projektes. Ich erinnere mich wärmstens an die Zeiten an der Bench zurück und bin dankbar, so gute und herzliche Lehrer im Labor gehabt zu haben.

Meinen großartigen Eltern, Zofia und Jacek Mossakowski, danke ich für ihre Liebe, Selbstlosigkeit und ihren Beistand immer und überall. Ich habe Euch schon unzählige

Male gesagt, dass Ihr die besten Eltern der Welt seid, aber jetzt steht es in einem Buch und Ihr könnt aufhören, daran zu zweifeln. Kocham was na świecie!

Oliver, mein Fels in der Brandung, danke, dass Du immer für mich da bist. Du hast Dir nun bestimmt hundertmal im Präsentationstestlauf erklären lassen, wie FLIM funktioniert und wie es die Welt verändern wird, hast sicher tausend Powerpointfolien gegenlesen müssen und unendlich viele Abende stundenlang auf mich gewartet. Danke für Deine Geduld und Deine Käsebrote. Und für alles andere auch.

Diese Arbeit wäre nur halb so gut und ich nur halb so glücklich, wenn es Euch nicht gäbe, liebe Anne, liebe Jana und liebe Dorothee. Ihr habt mich angekurbelt, Ihr habt mir zugehört, Ihr habt mit mir nachgedacht, gebangt und gefeiert. Danke für Eure sorgfältigen Korrekturen, herausfordernden Kommentare und Eure stetige Ermunterung. Genau das habe ich gebraucht!

Ein solches Projekt ruht natürlich auf noch sehr vielen weiteren Schultern, denen wiederum sehr kluge und freundliche Köpfe aufsitzen. Ich danke allen, die mich in den letzten Jahren gefördert und bestärkt haben und im Kleinen wie im Großen an der Fertigstellung dieser Arbeit beteiligt waren. Ich hatte eine außergewöhnliche Zeit und mit Euch gemeinsam einen tollen Start in das wissenschaftliche Leben!